Electro-Catalytic Reforming of Ethylene Glycol

Kurt Augustus Spies

A dissertation
submitted in partial fulfillment of the
requirements for the degree of

Doctor of Philosophy

University of Washington

2012

Reading Committee:
Dan Schwartz
Rick Gustafson
Eric M. Stuve, Chair

Program Authorized to Offer Degree:
Chemical Engineering

University of Washington

Abstract

Electro-Catalytic Reforming of Ethylene Glycol

Kurt Augustus Spies

Chair of the Supervisory Committee:
Professor Eric M. Stuve
Chemical Engineering

Biofuels continue to receive national attention motivated by concerns about finite energy supplies, geopolitical issues surrounding petroleum imports, and the environmental impact of fossil fuels. Biomass is an abundant resource, but is not easily converted to a usable transportation fuel. The aqueous phase reforming (APR) process [1] shows promise for converting compounds derived from biomass into hydrogen and alkanes at moderate temperatures (≈200 °C) in the aqueous phase. However, hydrogen selectivity in APR is a major hurdle, especially as carbon chain length of the feed molecules increase [2].

An alternative and complementary process for reforming carbohydrates is electro-catalytic reforming (ECR) which involves electrooxidation of carbohydrates and reduction of generated protons to produce hydrogen at the cathode. In this work we use ethylene glycol as a prototypical carbohydrate, as it is the simplest sugar-like molecule. The primary reactions in this system are equations 1 and 2 for the anode and cathode respectively.

$$C_2H_6O_2 + 2H_2O \longleftrightarrow 2CO_2 + 10H^+ + 10e^- \quad (1)$$

$$2H^+ + 2e^- \longleftrightarrow H_2 \quad (2)$$

Protons formed at the anode reduce and form gaseous hydrogen at the cathode. The formation of hydrogen in a separate compartment from the reactants, simplifies hydrogen removal and purification, and improves overall hydrogen efficiency by preventing

deleterious homogeneous reactions. Successful electro-catalytic reforming rests largely on effective electrooxidation, which typically is hampered by formation of poisons at the anode [3].

We developed a reactor that utilized a proton exchange membrane fuel cell architecture and operated up to 140 °C and 3.04 MPa with a liquid phase reactant. The reaction was studied by cyclic voltammetry and step potential measurements. We measured reaction products by gas chromatography (GC) and high pressure liquid chromatography (HPLC). We corroborated findings that saw a decease in electrooxdation potential of ethylene glycol with increasing temperature [4].

We focused on increasing the operating temperature of the ECR reactor to improve its catalyst poison tolerance and to approach operating conditions of APR. However, to increase temperature a high temperature electrolyte needed to be developed. We studied cross-linked sulfonated poly ether ether ketone membranes to test their viability to increase the temperature range of ECR. Unfortunately, we found that these materials undergo dissolution in high temperature aqueous phase environments and are not suitable to improve the range of ECR.

Using a Nafion electrolyte, and GC and HPLC data, we were able to close the mass balance on the ECR reaction. We measured five major products of the reforming reaction: carbon dioxide, hydrogen, glycolic acid, glycolaldehyde, and oxalic acid. For operating conditions of 137 °C and 0.7 V we calculated that ECR uses 36% less platinum than APR at 265 °C, to reform an equivalent amount of ethylene glycol.

TABLE OF CONTENTS

LIST OF FIGURES

Figure Number Page

LIST OF TABLES

ACRONYM LIST

APR: Aqueous Phase Reforming

BDM: 1,4-Benzenedimethanol

DMAC: Dimethylacetamide

DMF: Dimethylformamide

ECR: Electro-Catalytic Reforming

GC: Gas Chromatography

HPLC: High Pressure Liquid Chromatography

IGERT: Integrative Graduate Education and Research Traineeship

MSA: Methanesulfonic Acid

PEEK: Poly Ether Ether Ketone

NMP: N-Methylpyrrolidone

SPEEK: Sulfonated Poly Ether Ether Ketone

ACKNOWLEDGMENTS

I am very grateful to all the people who have contributed to my success in this research project, dissertation, and graduate school experience. I would like to thank my advisor, Eric Stuve, for his guidance, patience, and willingness to send me on travel to present my work. I would also like to thank Dan Schwartz for the amazing opportunity to take part in IGERT and for challenging me. I would like to acknowledge Angelina Snodgrass for my Guatemala experience, expanding my understanding about energy policy, and broadening my experience with energy policy impacts. I am indebted to Ken Faires, Arne Biermans, and Dave Gery for their assistance in building the ECR reactor, and being a sounding block for design ideas. I would like to thank Laurie Stephan for being a go-to person for IGERT and related activities and always being extremely helpful.

I am thankful to have had the opportunity to work with a range of talented colleagues and friends who have enhanced my graduate school experience including: Cortney Kreller, Liney Arnadottir, Ken Faires, James Matthaei, Hai Nguyen, Tim Geary, TJ McDonald, Shannon Ewanick, Dinesh Baskar, Jeff Richardson, and Sara York. I am extremely beholden to my family, Tom, Amy, Jack, and Paul Spies for their encouragement, understanding, and belief in me, through good days and bad. I also want to thanks Sarah Widder for her support throughout my studies and pushing me to always improve.

Finally I would like to acknowledge the National Science Foundation through IGERT and CBET-EAGER for proving funding for my research and The Electrochemical Society PAED Division, UW GPSS, and the UW Chemical Engineering department for conference travel grants.

DEDICATION

To Sarah and my family, for their constant encouragement and support.

Chapter 1

INTRODUCTION AND MOTIVATION OF RESEARCH

The world is addicted to fossil fuels. Representing more than 85% of our primary energy consumption [5], this dependence has many negative impacts. Concerns about finite energy supply, geopolitical issues surrounding petroleum imports, and the environmental impacts of fossil fuel combustion question whether this level of consumption is sustainable, environmentally, economically, and physically. To help mitigate some of these issues and develop secure energy supplies for future generations, our nation requires a change in energy portfolios to include more renewable and environmental sources such as bioenergy [6].

Bioenergy, defined as energy generated from biologically derived material, has many benefits over fossil fuels. The most widely publicized advantage is the significant reduction in life-cycle greenhouse gas emissions as compared to fossil fuels [6, 7]. The creation of a bioenergy market will stimulate rural economies, increase domestic energy investment, and offer a secondary market for waste products [6]. The use of waste products for energy can offer the additional benefits of saved landfill space and improved local air quality [7]. However, while the use of bioenergy has significant non-market benefits over fossil fuels, it is currently more expensive and its higher cost impedes widespread use [8].

The variety of feedstocks in bioenergy makes a single efficient conversion technology difficult. Direct combustion, liquid transportation fuel, and hydrogen for fuel cells each have a different economic model and price. A study, by the author and his colleagues, analyzed biomass price and availability to supply a wood fired boiler for a combined heat and power application on behalf of the Confederated Tribes and Bands of the Yakama Nation, Appendix A. An expert local forester, interviewed for the study, estimated the market for woody biomass at around 40-50 dollars per bone dry metric ton (BDMT) delivered. This was about 20% of all the available biomass in the study area, which included Yakima, Kittitas, Klickitat, Benton, and Grant counties in the state of Washington. For comparison, an equivalent amount of coal by energy content sells for an average of 39 dollars in the United States [5]

Much of the cost of biomass is because it is a disperse low density resource, which increases transportation and collection costs [8]. A study by MacLean et al. estimated that the United States has about 568 million metric tons of biomass available for energy if the market could pay $100 per BDMT [9]. In order to access an increased volume of available biomass, the market prices for biomass must have a higher value. One way to do this is to convert biomass into a more valuable form, like transportation fuels or hydrogen.

If an economical conversion technology for converting biomass to hydrogen or a transportation fuel can be found, a larger supply of woody biomass would be available. Increased availability of bioenergy can replace more fossil fuel, increasing the environmental, economic, and physical sustainability of the U.S. fuel mix. This study will focus on hydrogen because it is a product of reformation and has a variety of energy applications.

Today, hydrogen is generated primarily through stream reforming of natural gas or by catalytic reforming of petroleum [10, 11]. Hydrogen is a commodity in an oil refinery because of its use in hydrotreating and hydrocracking of petroleum products [11]. Large quantities of hydrogen are also used to hydrogenate cooking oils to make margarine. In the future, hydrogen demand is expected to increase because of the move to further reduce the sulfur content of fossil fuels through hydrotreating [11], the development of the hydrogen economy and fuel cells [10], and for use in upgrading biomass-derived fuels into higher quality energy fuels [12]. Biofuel upgrading is a large potential growth area for hydrogen consumption because of energy policy interest in second generation biofuels [13]. The hydrogen demand of upgrading is higher for biomass derived molecules because of the lower H/C ratio than for petroleum feedstocks [14]. In this way, the environmental footprint of biofuels is inextricably linked to the availability of economic hydrogen production.

Aqueous phase reforming (APR), discovered by the Dumesic group at the University of Wisconsin, converts biomass-derived compounds to hydrogen and alkanes [2, 15–18]. It works by a combination of dehydration, dehydrogenation, water-gas-shift, and carbon-carbon cleavage pathways [2]. Equation 1.1 shows reforming of ethylene glycol. APR is promising because of tolerance of wet and non-volatile fuels and potential for incorporating biomass sugars into a refinery [1]. Unlike gas phase processes, processing in the aqueous phase prevents large non-volatile sugars like glucose from decomposing [2]. If these sugars were allowed to decompose, they would form solid carbon, olefins, and aromatics that can coat catalysts and reduce the reactant yield [19]. The Dumesic group was able to achieve high hydrogen selectivities especially for smaller chain molecules, Figure 1.1. This low flowrate and high catalyst loading requirement makes its commercial viability limited.

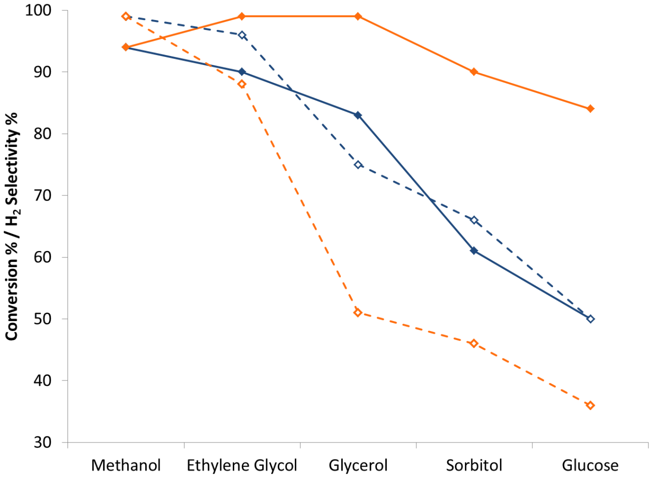

Figure 1.1: A figure of data from Cortright et al [2]. showing reactant conversion (solid line) and hydrogen selectivity (dashed line) for temperatures of 498 K (blue) and 538 K (orange) of different oxygenated hydrocarbons. The reaction system was 1 wt% reactant, a flowrate of 3.6 mL per hour through a 5mm inner diameter steel reactor 45 cm long with 4.5 g of 3 wt% Pt/Al_2O_3 catalyst.

$$C_2H_4(OH)_2 + 2H_2O \longrightarrow 2CO_2 + 5H_2 \tag{1.1}$$

There is a need for a more efficient conversion pathway for biomass to hydrogen and the development of aqueous phase reforming suggests there may be an equivalent electrochemical pathway that could have a higher selectivity and faster kinetics. This research explores the feasibility of electro-catalytic reforming (ECR) of biomass derived compounds and its potential benefits compared to APR. An electro-catalytic reforming reactor will operate by oxidizing a carbohydrate at the anode of an electrolyte membrane and a hydrogen recombination reaction at the cathode, Figure 1.2. The overall reforming reaction follows the same stoichiometry as APR , Equation 1.1. By separating the product hydrogen from the other reactant species through the electrolyte membrane, the hydrogen selectivity for the reaction is expected to be improved.

To reach conditions of APR the reactor must be heated to temperatures of about 200 °C and pressures sufficient to maintain an aqueous phase. This is outside the range of typical fuel cell operation parameters that the ECR reactor is designed from. A high temperature electrolyte and high pressure seals are necessary to test the feasibility of ECR. In addition, energy is required to drive the reaction because reforming is endothermic. In APR the energy was completely supplied from thermal energy, for ECR it will be a combination of thermal energy and electrical energy. For large scale application of an ECR system a fraction of the biomass that is not suitable for reforming, such as lignin, could be used to offset the energy requirements of the system.

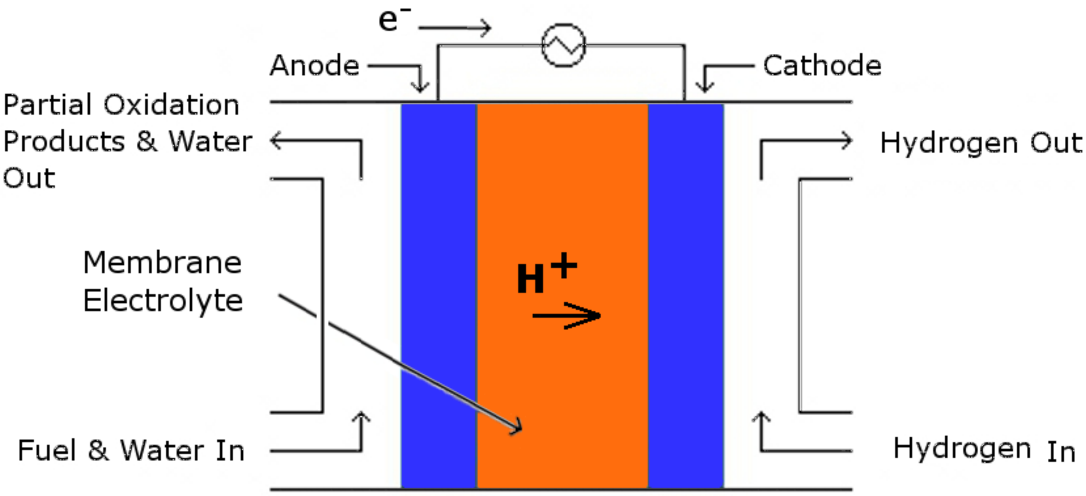

Figure 1.2: An illustration of the electro-catalytic reforming reactor. Fuel comes in as an aqueous stream at where oxidizes into protons, electrons, and oxidation products. The protons recombine with the electrons on the cathode to make hydrogen gas.

Chapter 2

SURVEY OF LITERATURE

Electro-catalytic reforming is a series of aqueous phase electrochemical partial oxidation reactions that form hydrogen from wet biomass based compounds. Generating hydrogen from these oxygenated hydrocarbons without drying, would allow a more efficient route for this underutilized resource [9]. Aqueous phase reforming, developed at the University of Wisconsin, pursues this objective by thermo-catalytic reforming [15–17, 20–22]. ECR offers an additional degree of freedom to influence the reforming reaction over APR, by controlling the reaction potential. This potential control changes the stability of adsorbed surface species on the catalyst and could be used to optimize the reaction conditions. The other major difference between ECR and APR is the inclusion of an electrolyte membrane to separate the product hydrogen from the reactants. However, to simulate APR conditions of 200 °C and 3.0 MPa a high temperature electrolyte is needed. This chapter will review the literature in two main sections: electro-catalytic reforming and high temperature electrolytes. Within each section a series of sub topics relevant to the overall objective will be discussed.

Related work on electrochemical oxidation of small chain oxygenated hydrocarbons has been extensive motivated by interest in direct alcohol and polyol fuel cells [23–30]. This work, coupled with APR observations, recognizes C-C bond scission as a rate limiting step in the full utilization of multi-carbon fuels to hydrogen [2, 31, 32]. For this reason we will be investigating ethylene glycol, the simplest two carbon polyol with stoichiometry close to a carbohydrate.

2.1 Electro-Catalytic Reforming

While there is no known research explicitly of ECR of ethylene glcyol, there is sufficient information to define the experimental design. Relevant topics include: biomass derived feedstocks, aqueous phase reforming, carbon monoxide poisoning of platinum catalysts, and electrochemical oxidation of ethylene glycol.

Biomass derived feedstocks are important for ECR because they allow hydrogen product to be made from renewable resources instead of fossil fuels. The use of biomass derived feedstocks produces its own challenges, however. Reaction conditions that lead to carbon-carbon bond breakage and complete oxidation of the reactants are necessary for economically utilizing the available chemical potential energy in the feed molecule.

Aqueous phase reforming is important for comparison because work there has looked at the thermochemical breakdown of ethylene glycol and its process parallels electro-catalytic reforming in areas of: back pressure necessary to maintain the high temperature aqueous phase, high surface area catalyst to generate measurable amounts of reaction products, and separate phase analytics to measure gas phase and liquid phase products. Electrochemical oxidation of ethylene glycol in a fuel cell is the same anode reaction as reforming. In a fuel cell, oxidation of a fuel on the anode is coupled with the oxygen reduction reaction on the cathode to drive the reaction. In reforming, the cathode reaction is driven by applied voltage to generate hydrogen.

From an efficiency standpoint, the energy supplied to drive the ECR reaction above the ideal heat of formation is wasted. However, the overpotential can heat the system and reduce the thermal load as long as the overpotential is less than or equal to the heating load. Increasing the temperature is beneficial because of reaction kinetics and CO surface poisoning. At low temperatures and low potentials the ECR reaction has a low rate due partly to irreversible surface coverage of carbon monoxide on the platinum catalyst [33–35]. A temperature that facilitates driving the reaction and using overpotential for thermal heating will be the most efficient.

2.1.1 Biomass Derived Feedstocks

Biomass derived feedstocks typically are highly oxygenated, which reduces their energy content and their ability to be used directly as a fuel for combustion. The location of the oxygen in the polyol influences products possible by functional group oxidation, without

C-C bond cleavage. The feasible oxidation products for primary, secondary, and tertiary alcohols is shown in Figure 2.1. Two polyols with equivalent stoichiometry may have very different possible partial oxidation products. From a fuel utilization standpoint, oxidation of polyols to carboxylic acid is preferable when C-C bond cleavage is not achievable, because more of the chemical potential energy of the reactant is harnessed. Fortunately, oxygenated hydrocarbons from biomass are primary or secondary alcohols [36]. The most common oxygenated hydrocarbons from biomass are primarily 5 or 6 carbon sugars: glucose, galactose, mannose, xylose, and arabinose [36]. The relatively long carbon chain length of these molecules leads to a significant number of potential partial oxidation products, which complicates analytical measurement.

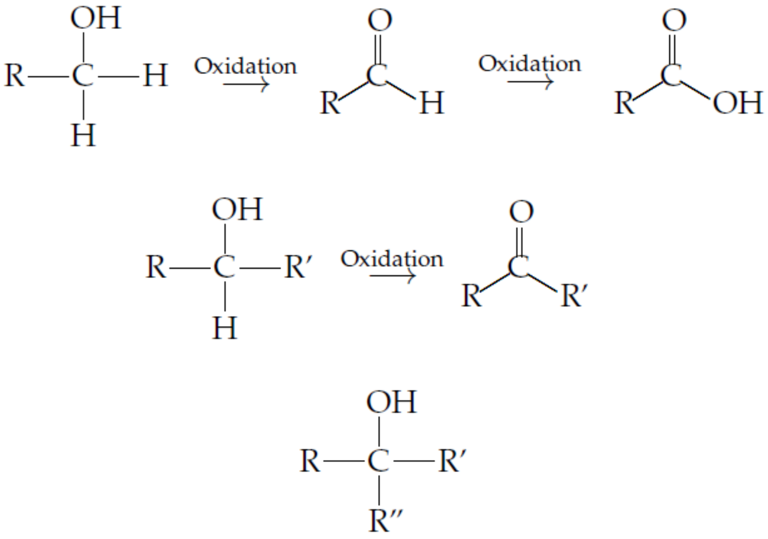

Figure 2.1: The possible oxidation reactions for alcohols without C-C bond cleavage. The top series starting with a primary alcohol can proceed to an aldehyde and end with a carboxylic acid. The secondary alcohol in the second row can only proceed to a ketone and no further. A tertiary alcohol, the bottom row, cannot be oxidized due to an absence of a proton on the carbinol carbon [37]. The oxidation cannot proceed further for any of the alcohols unless a carbon-carbon is broken.

Our choice to study ethylene glycol as a model biomass molecule minimize any analytic complexity due to its smaller size, Fig. 2.2. Ethylene glycol has the same general functionalities of the larger polyols including: C-C, C-O, C-H bonds [15], hydroxyl groups adjacent to carbon atoms [38], a primary alcohol moiety, and a carbon-to-oxygen (C/O) ratio of 1. The presence of the C-C bond is the most important characteristic of ethylene glycol for comparison to larger polyols due to its resistance to bond cleavage in catalytic oxidation.

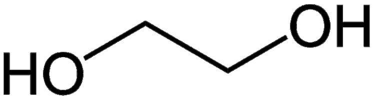

Figure 2.2: Ethylene glycol chemical structure

2.1.2 *Aqueous Phase Reforming*

Aqueous phase reforming is a catalytic process initially developed by the Dumesic group at University of Wisconsin for the reforming of oxygenated hydrocarbons [39]. The reaction is a "low temperature" heterogeneous catalysis reaction, ≈ 225 °C. An aqueous solution of an oxygenated hydrocarbon is pressurized and flowed past a catalyst [40]; such as Pd, Pt, or Rh. The reaction for complete reforming of ethylene glycol can be seen in Eqn. 2.1.

$$C_2H_6O_2 + 2H_2O \longleftrightarrow 2CO_2 + 5H_2 \tag{2.1}$$

Aqueous phase reforming has several advantages over traditional fuel conversion processes. Since the fuel stream is liquid, water in the fuel does not need to be volatilized, thus saving energy compared to vapor-phase processes like steam reforming [41]. The lower temperature of the reaction helps to minimize undesirable decomposition reactions typically encountered when heating carbohydrates [41].

A significant number of papers have looked at the best catalysts for APR [42–45]. The consensus for a 'good' APR catalyst are: a high selectivity for C-C bond cleavage, low selectivity for C-O bond cleavage, low hydrogenation activity, and a high overall reforming activity [40]. The C-C bond cleavage is important for breaking down the reactants into more reactive species [40]. Cleavage of the C-O bond followed by subsequent hydrogenation of the adsorbed species leads to alcohols and organic acids, which are undesirable final products [40]. Hydrogenation of carbon monoxide can lead to alkanes, which can be desirable for aqueous phase reforming though it reduces the overall hydrogen selectivity [40].

Dumesic et al. exmained aqueous phase reforming of ethylene glycol over a variety of silica-supported catalysts including Ni, Pd, Pt, Ru, and Rh [41]. The experimental conditions were 210 °C and 10 wt% ethylene glycol (≈ 1.6 M ethylene glycol). They noted the following trends for H_2 selectivity, eqn 2.2, and CO_2 turnover frequency, eqn 2.3 [41].

$$\text{H}_2\text{ Selectivity:}\quad \text{Pd} > \text{Pt} > \text{Ni} > \text{Ru} > \text{Rh} \tag{2.2}$$

$$\text{CO}_2\text{ Turnover:}\quad \text{Pt} \approx \text{Ni} > \text{Ru} > \text{Rh} \approx \text{Pd} \tag{2.3}$$

The selectivity of oxygenated hydrocarbons to hydrogen and alkanes of different oxygenated hydrocarbons via aqueous phase reforming is shown in Figure 2.3. The APR definition of alkane selectivity is number of gaseous alkane molecules normalized by number of carbon molecuels in the gas phase. Hydrogen selectivity is the number of hydrogen molecules normalized by the maximum theoretical yeild assuming all the carbon in the gas phase was from complete reforming. Illustrated is the difficulty of breaking all of the carbon-carbon bonds, especially as the hydrocarbon increases in chain length. For small single carbon molecules, like methanol, oxidation is facile and the reactant proceeds easily to CO_2 under APR conditions [2]. For larger molecules, breaking of the carbon-carbon bond and formation of carbon dioxide are hindered [46]. The non-zero alkane selectivity for methanol is due to the reverse steam reforming reaction also known as methanation, eqn 2.4.

$$CO + 3H_2 \longrightarrow CH_4 + H_2O \tag{2.4}$$

The apparent activation energy for ethylene glycol to hydrogen over a Pt/Al_2O_3 catalyst is about 100 kJ/mol [16]. The apparent activation energy does not account for deceasing hydrogen selectivity with increasing temperature [16].

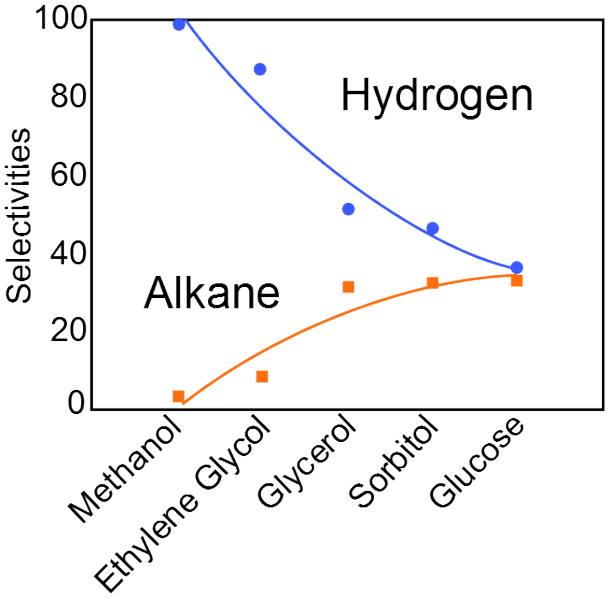

Figure 2.3: Selectivities (%) versus reactant in aqueous phase reforming. Alkane selectivity is defined as the number of gaseous alkane carbon atoms normalized by the total amount of gaseous carbon atoms. Hydrogen selectivity is the number of hydrogen moles present normalized by the maximum yield of hydrogen assuming all of the carbon atoms in the gas phase participated in reforming.

2.1.3 Addressing Carbon Monoxide as a Catalyst Poisoning

Catalyst poisons created as intermediates of heterogeneous reactions can lead to significant reductions in catalyst activity. In the case of oxidation of oxygenated hydrocarbons on platinum, carbon monoxide is the most prominant poison [34, 47]. Carbon monoxide was first observed by Lamy et al., who used electrochemical modulated infrared spectroscopy to look at methanol oxidation at room temperature [47, 48]. Ethylene glycol and glycerol have been observed to form carbon monoxide when exposed to clean platinum at room temperature [40].

There are three ways to make a catalytic system more CO tolerant: (1) increase the temperature [49, 50], (2) add more CO tolerant catalyst metals to the platinum catalyst [26], and (3) apply a potential on the catalyst sufficient to oxidize the adsorbed CO. High temperature operation of proton exchange membrane fuel cells has been shown to increase the tolerance of CO [49, 50]. Alberti et al. estimated that a fuel cell working above 120-130 °C would see a significant decease in carbon monoxide poisoning on platinum [51]. The increased tolerance is related to the thermodynamics of adsorption of carbon monoxide and hydrogen on the platinum catalyst. Competitive adsorption of carbon monoxide and hydrogen on the Pt surface may be described by Langmuir adsorption isotherms [50]. Carbon monoxide adsorbs associatively on platinum below about 230 °C (eqn. 2.5), whereas hydrogen is dissociatively adsorbed (eqn. 2.6) [52].

$$CO(g) + Pt \longrightarrow Pt - CO \tag{2.5}$$

$$H_2(g) + 2Pt \longrightarrow 2\,(Pt - H) \tag{2.6}$$

The Bocarsly group at Princeton investigated high temperature fuel cells as a way to increase tolerance to carbon monoxide [53]. They compared the two different catalysts Pt and Pt/Ru at two different temperatures 80 °C and 130 °C for the performance of the fuel cell when 100 ppm of carbon monoxide was introduced [53]. They found a significant increase in performance for the platinum fuel cell when heated. In addition, they saw an improved tolerance of the system for carbon monoxide with the incorporation of ruthenium in the platinum catalyst [53].

2.1.4 Electrochemical Oxidation of Ethylene Glycol

Electrochemical oxidation of ethylene glycol has been well studied [3, 25, 54–63]. Its potential as a fuel for direct alcohol fuel cells has motivated a majority of the investigators [64,65]. The ideal electrochemical reactions for ethylene glycol in a fuel cell are shown below, with ethylene glycol oxidation occurring at the anode, eqn. 2.7, and oxygen reduction occurring at the cathode, eqn. 2.8. The complete ideal oxidation reaction of ethylene glycol to carbon dioxide and water, eqn. 2.9, is exothermic with ΔH_{HHV} = -1,260 kJ mol^{-1}.

$$C_2H_6O_2 + 2H_2O \quad \longleftrightarrow \quad 2CO_2 + 10H^+ + 10e^- \tag{2.7}$$

$$4H^+ + 4e^- + O_2 \quad \longleftrightarrow \quad 2H_2O \tag{2.8}$$

$$C_2H_6O_2 + 2H_2O \quad \longleftrightarrow \quad 2CO_2 + 5H_2O \tag{2.9}$$

The majority of ethylene glycol electrooxidation work has been done at room temperature with alkaline [25,55–57] or acidic electrolytes [3,57–61]. However, some studies have looked a the kinetics and thermodynamics up to 100 °C [4,54,65].

Ethylene glycol is expected to completely oxidize by reacting along a sequence of 2 electron steps, culminating with CO_2. Each step forms partial oxidation products, which can either continue oxidizing or leave the system as a product. There is a consensus around a "dual path reaction mechanism" for oxidation of ethylene glycol [46,61]. The functional group oxidation pathway, Fig. 2.4, involves the successive oxidation of partial oxidation products without attacking the carbon-carbon bond [61]. The second pathway involves breaking the carbon-carbon bond with the formation of partial oxidation products, here exemplified by CH_2OH, and eventually the formation of adsorbed carbon monoxide [61], eqn 2.10.

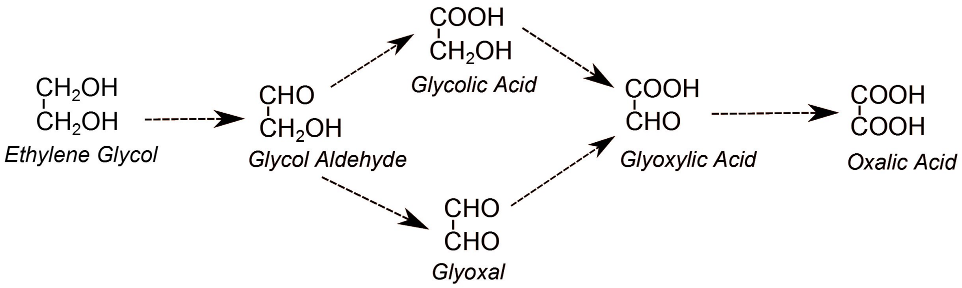

Figure 2.4: The partial oxidation pathway for ethylene glycol, adapted from Tornquist et al. [61]. Each arrow represents a two electron transfer step.

$$\mathrm{C_2H_6O_2} \rightarrow 2\,[\mathrm{CH_2OH}]_{\mathrm{ads}} \overset{8e^-}{\rightarrow} 2\,[CO]_{\mathrm{ads}} \rightarrow 2\mathrm{CO_2} \tag{2.10}$$

Researchers have measured a range of partial oxidation products for ethylene glcyol electrooxidation depending on the conditions: glycolaldehyde, glycolic acid, glyoxal, glyoxylic acid, oxalic acid, formic acid, and formaldehyde [60–62, 66, 67]. Vijh measured glyoxal and oxalic acid in a solution with an acidic electrolyte at room temperature and an applied potential of about 0.68 V_{RHE} [60]. Korzeniewski et al. detected glycoladehyde, glycolic acid, and oxalic acid from electrolysis of ethylene glycol in an acidic electrolyte at 0-0.6 V_{SCE} [62].

Belgsir et al. observed two cases of electrooxidation of ethylene glycol on a PtPb catalyst [66]. In the first case, the potential was set to 0.76 V_{RHE} for 30 seconds. This case generated large amounts of glycoladehyde and glycolic acid with trace amounts of oxalic acid along with carbon dioxide. The second case, the potential was set to 0.60 V_{RHE} followed by a step change to 0.15 V_{RHE} and finished with step change to 0.77 V_{RHE}. This case generated predominantly glycolaldehyde with trace amounts of glycolic acid. No oxalic acid or carbon dioxide were detected in the second case [66]

Reaction potential, reactant concentration, and catalyst loading have been seen to affect both the overall reaction rate of the electrooxidation of ethylene glycol and similar two carbon molecules and the partial oxidation product distribution [46, 68]. Increasing catalyst loading or reactant concentration increased the ethylene glycol electrooxidation rate. Reaction potential was also proportional to electrooxidation rate, but at the cost of additional overpotential. The pH of the electrolyte was also observed to affect the partial oxidation product distribution [61].

Reducing the required potential of the system will reduce the overpotential. However, at room temperature potentials less than 0.3 V_{RHE} are insufficient. For example, Vijh observed sustained oxidation at about 0.68 V_{RHE}. The combination of low kinetics at room temperature and the challenge of carbon monoxide as a catalyst poison contribute to inactivity of the reaction at low over potentials [49]. To achieve a goal to minimize the over potential, a higher temperature fuel cell is required [49].

2.2 High Temperature Electrolyte Membranes

Electrocatalytic reforming (ECR) has been investigated by our group as a route for hydrogen generation from biomass derived carbohydrates [69]. A crux in the design of the ECR is a high temperature proton conducting electrolyte membrane that is stable in aqueous environments. The membrane is needed to separate product H_2 from the reactants and CO_2. This separation is essential because hydrogen products derived from biomass can quickly react homogeneously with the biomass reactants or carbon dioxide, reducing the overall hydrogen yield and system efficiency.

Nafion, the dominant proton exchange electrolyte, has a temperature limit of about 120 °C due to dehydration and loss of mechanical strength [70]. The goal of ECR is to achieve at least 160 °C to examine predictions of complete etheylene glycol reforming into CO_2 in work published by Behm [4]. To achieve this temperature goal, a new proton exchange membrane material or anionic membrane is needed.

Temperature stability for membranes can be related to two different things: (1) thermal stability, which is related to melting point and combustion temperature, and (2) dissolution stability, which is the resistance of a polymer to dissolution in the aqueous phase under the reaction conditions. For Nafion, the problem is dissolution stability. Polymer dissolution involves two steps: solvent diffusion, and chain disentanglement [71]. Solvent diffusion starts when a polymer comes in contact with a suitable solvent. This leads to plasticization of the polymer and the creation of a gel layer. Chain disentanglement occurs at the interface between the gel layer and the solvent where polymer chains lose their structure and diffuse into the solvent [71]. In high glass transition temperature films of latex, Peckan et al. observed three stages of dissolution: 1) swelling of the polymer dominates and the gel layer increases with time, 2) the gel layer reaches an equilibrium when diffusion is approximately equal to the diffusion of the disentangled chains from the gel layer into the liquid layer, and 3) when the gel layer decrease in thickness with time because there is no more glassy polymer [72].

In literature, there are two classes of materials that have been extensively explored for high temperature proton exchange membranes: polybenzimidazole (PBI) and sulfonated-poly-ether-ether-ketone (sPEEK) [73,74]. PBI membranes have shown stability approaching temperatures of 200 °C [75] which wihtin the operating range of ECR.

However, PBI is not suitable for operation in conditions with liquid water. This is due to leaching of the phosphoric acid that PBI membranes rely on for conductivity [76–78]. In addition, the leached phosphoric acid reacts with the reactant carbohydrates in ECR to form undesirable products by acid hydrolysis. For that reason sPEEK was chosen as the general class of membrane materials to explore for high temperature operation in aqueous environments.

2.2.1 Sulfonated-Poly-Ether-Ether-Ketone Electrolytes

The conductivity of sPEEK is directly dependent on the degree of sulfonation (DS) of the polymer. The degree of sulfonation is defined as the number of sulfonic acid groups per repeat unit. The degree of sulfonation is a controlled by the time and temperature of sulfonation. Longer time leads to higher sulfonation degrees, and increased temperature lead to increased DS because of improved sulfonation kinetics [79].

Sulfonation of PEEK is performed by reacting the polymer with sulfuric acid. This can be done in two ways: heterogeneous sulfonation and homogeneous sulfonation. The distinction lies in how the polymer is dissolved. In heterogeneous sulfonation, PEEK is dissolved in sulfuric acid where it undergoes dissolution and sulfonation simultaneously. Homogeneous sulfonation is achieved by dissolving PEEK in methylsulfonic acid (MSA), which does not sulfonate the polymer. After the polymer is fully dissolved, sulfuric acid is added to sulfonate the mixture. A sPEEK sample that is heterogeneously sulfonated will have a wider distribution of chain lengths between the sulfoinc acid groups than the homogeneous route. This is because the simultaneous dissolution and sulfonation tends to form highly sulfonated regions in the polymer while separating the steps leads to a more uniform distribution of sulfonic acid sites.

It is unclear if one of the types of sulfonation will lead to a polymer that is more stable to high temperature dissolution than the other. Kim et al. compared homogeneous and heterogeneous sulfonation by looking at water uptake, conductivity, tensile strength, and glass transition temperature at room temperature [80]. They found that the homogeneous sample had higher proton conductivities for a given ion exchange capacity, which was related to larger water uptake of that polymer. The tensile strength was inversely proportional to the amount of water uptake of the membrane [80]. They attributed the decrease in tensile strength with increasing water to plasticization of sPEEK [80]. There was no difference between the two techniques for glass transition temperature, which increased with increasing degree sulfonation [80].

At high DS (DS $> 70\%$) sPEEK polymers swell and lose mechanical stability, limiting their applicability as proton exchange membranes. This swelling increases with temperature until the high-DS sPEEK membranes become fully solvated by water and completely lose their mechanical stability [81]. Solvation of sPEEK leads to fuel cross-over and electrode shorting [82]. Conversely, low DS levels do not permit sufficient water uptake for adequate proton conductivity [79].

Even with high degrees of sulfonation, sPEEK membranes with a similar equivalent weight (EW) to Nafion have a lower proton conductivity [82]. One suggestion to the difference was the distribution of sulfonic acid groups. In Nafion the groups form clusters; in sPEEK the distribution is more random. A complementary suggestion was that Nafion's perfluoether-based pendant side-chain can move and flex to aid proton transport, while sPEEK membranes are more rigid [82].

Work by Kreuer on the microstructure of Nafion and sPEEK attributes the difference in proton conductivity to functionalities of the polymer backbone [83, 84]. The Nafion backbone is highly hydrophobic with well defined channels, while sPEEK has a slightly hydrophilic backbone with poorly defined channels. The work also noted an increase in hydrogen bonding with sPEEK polymers.

While Nafion is widely used in PEM and DMFC applications, it suffers from high cost, and negative impacts from fuel cross-over. sPEEK membranes show promise when compared to Nafion when the polymer is cross-linked or blended because they can be tailored to have the desired physical and chemical properties [82]. Nafion membranes have a lower glass transition temperature (about 110 °C) than sPEEK membranes (about 160 °C) depending on the degree of sulfonation [85, 86]. This increase in glass transition temperature may lead to better stability than Nafion at high temperatures [86].

The irreversible swelling of high-DS sPEEK membranes in high temperatures liquid environments, is the main limitation for their widespread application as high temperature proton exchange membranes. There have been three main techniques used to improve the stability of sPEEK while still maintaining sufficient proton conductivity: inorganic fillers, polymer blending, and cross-linking.

2.2.2 *Inorganic Fillers and Polymer Blending*

Common inorganic fillers, used to increase the mechanical stability of proton exchange membranes, include: SiO_2 [87], ZrO_2, and TiO_2. A study by Yu et al. used a sol-gel reaction of tetraethylorthosilicate (TEOS) with a commercial Nafion 1135 (1100 molecular weight, 0.0035 inch thick (0.089 mm)) membrane to produce a composite nafion/silicon oxide(SiO_2) membrane [87]. They observed improved performance of the membrane in a fuel cell system at 110 °C and about 28% relative humidity (70 °C H_2, no O_2) over Nafion at ambient pressure. The attributed the improved performance of the SiO_2 composite mostly to an increase in hydration of the membrane. Their control Nafion membrane became dried out and failed due to water loss under these operating conditions. The improved performance of the membrane can be attributed to an improvement in water retention. They had no conclusive evidence of improved the stability of the these electrolyte at high temperatures. In addition, inorganic fillers frequently lead to porosity problems and pinholes due to poor adhesion between the fillers and polymer, making them unsuitable for applications where mechanical strength is needed [88].

2.2.3 *Cross-linked SPEEK*

There has been a significant amount of work exploring improved thermochemical stability of polymers such as PEEK from cross-linking. This work is motivated by findings that cross-linking of sPEEK polymers with small molecules can lead to polymers with restricted dimensional change and decreased water uptake [82]. This cross-linking can be done while maintaining high proton conductivities necessary for PEM fuel cell applications.

sPEEK has been cross-linked previously with aliphatic and aromatic molecules containing amine or amide functionalization as the crosslinker [89]. However, these reactions are thought to form sulfonamide linkages, which are known to undergo increasing rates of thermal hydrolysis with increasing temperatures [82], making them a poor choice for high temperature aqueous environments.

Kaliaguine et al. studied thermal cross-linking of previously cast sPEEK membranes with alcohols including: glycerol, ethylene-glycol, and meso-erythritol [90]. Cross-linking occurs via a condensation reaction between the sulfonic acid and hydroxyl functional groups [90]. This forms a sulfonic ester and causes an effective increase in the ionomer equivalent weight which leads to a lower proton conductivity. Unfortunately, the majority of sPEEK membranes cross-linked were soluble in water at 100 °C, although they did exhibit reduced swelling when compared to non-cross-linked membranes.

One of the most promising cross-linking techniques is Friedel-Crafts cross linking. Friedel-Crafts reactions, originally discovered in 1877, involve electrophillic aromatic substitution to attach substitutes to aromatic rings [91]. Since the 1980s these reactions have been used to attach aromatic C-H bonds asymmetrically to carbonyl compounds [91]. Due to the location of cross-linking on the sPEEK monomer away from the sulfonic acid group, the stability of the polymer can be improved without decreasing the effective degree of sulfonation. Friedel-Crafts cross-linking was previously used by Wilkie et al. to improve thermochemical stability of polystyrene [92, 93]. More recently, Friedel-Crafts cross-linking was used by Fenton et al. to improve the thermochemical stability of PEEK [82].

2.2.4 *Impact of Casting Solvent*

A variety of solvents have been used to solution cast sPEEK membranes including: dimethylacetamide (DMAc), dimethylformadmide (DMF), dimethylsulfoxide (DMSO), γ-butyrolacetone (GBL), n-methyl-2-pyrrolidone (NMP), water-acetone, and water [82, 94–97]. In literature, the choice of casting solvent was initially made based on its polarity and volatility [95]. The volatility of the casting solvent controls the morphology of the resultant membrane [95]. Typically, DMAc and DMF are used as casting solvents for lower degrees of sulfonation and water-acetone or water for higher levels of sulfonation [97]. However, two studies by Kaliaguine et al. found significant impact of the casting solvent on the proton conductivity and stability of the resultant membrane [95, 96]. Their conductivity data showed a significant decrease in conductivity of DMF membranes compared to DMAc. Kaliaguine et al. offered two likely reasons for that decease: (1) degradation of DMF and (2) hydrogen bonding by the DMF to the sulfonic acid sites of the sPEEK backbone. The degradation reaction for DMF observed at temperatures above of 60 °C was catalyzed by residual sulfuric acid and leads to the formation of n-methyl-methanamine salt, formic acid, and acetic acid. These degradation products interact with the sPEEK backbone and block sulfonic acid sites from proton conduction. Kaliaguine et al. observed that the degradation reaction also occurs with DMAc, but at higher temperatures (140 °C) [96]. Also, hydrogen bonding of DMF was significant in blocking proton conductivity [95]. This phenomenon was not observed to be significant with the use of DMAc or NMP as the casting solvent [96].

While there was no degradation pathway evident with NMP, Kaliaguine observed a decrease in conductivity due to the presence of the solvent in the resulting film [96]. Only when the solvent was sufficiently removed via heating at a vacuum oven at 130 °C for 24 hours did they see improved conductivity [96].

Other researchers have looked at the impact of casting solvents for sPEEK and other related membrane materials. Guan et al. looked at the impact of casting solvent on sulfonated polyethersulfone membranes. Similar to Kaliaguine et al., Guan et al. also observed decomposition of of membranes cast with DMF [98]. However, due to the low degree of sulfonation (DS = 26.7%) and low temperatures of their conductivity studies, they were unable to observe any quantifiable differences between DMAc and NMP as casting solvents [98].

One technique to avoid the impact of casting solvents on the proton conductivity is to start with a polymer with a high enough degree of sulfonation that it can completely dissolve in water at elevated temperatures, effectively using waster as the casting solvent. After casting the membrane can be cross-linked to give it appropriate stability for aqueous applications. To accomplish this Kaliaguine et al. found the degree of sulfonation threshold for complete solvation in water or water-acetone was about 80% [97]. However, it was difficult to accomplish because before casting the polymer was difficult to clean of residual acid [95]. Fenton et al. used water as their casting solvent in the fabrication of their Fiedel-Crafts cross-linked membranes [82].

A recent paper by Kim et al. studied removing residual solvent from the membrane after casting. They soaked membranes that had been cast with NMP, DMAc, DMSO, and DMF in 1 M sulfuric acid at 80 °C for 12 hours to remove the solvent [94]. Kim et al. saw dramatically improved conductivity and performance and observed that sPEEK membranes cast with NMP and cleaned of solvent showed cell performance that was comparable to Nafion 117 [94].

2.3 Summary

The objective of this research is to test the feasibility of ECR for generating hydrogen from biomass. To investigate the challenge of increasing partial oxidation products with increasing carbon chain length, we will be using ethylene glycol as the model molecule for biomass reforming. A series of reactor operation parameters will be explored to maximize reaction rate and product selectivity while minimizing temperature and potential applied. To understand the complete reaction, analytical tools will be used to track the partial and complete oxidation products of the reforming reaction. Of particular interest will be the conditions that favor carbon-carbon bond scission and minimize the impact of carbon monoxide poisoning.

To compare ECR to APR, similar reaction temperatures pressures will be pursued. To reach higher temperatures than is allowable by a Nafion electrolyte, we will be investigating the high temperature stability of a cross-linked sPEEK electrolyte membrane. Effects of fabrication techniques on the membrane stability including casting solvent will be explored.

Chapter 3

MATERIALS AND METHODS

This chapter was designed as a basis for future chapters and covers a wide range of methods and procedures including: analytical tools for measuring the oxidation products of the ECR reactor, membrane fabrication, membrane testing by TGA, DSC, and conductivity measurements, and finally MEA fabrication. Due to its significance, the fabrication of the ECR reactor will be discussed in its own chapter, chap. 4. The first section is a list of chemicals of materials used.

3.1 Chemicals and Materials

Chemicals and materials used in this research are listed in Table 3.1. The PEEK (Victrex© 450PF), obtained by a donation from Victrex USA inc, has a particle size of 50 μm. Water was supplied from a Barnstead Nanopure model D4751 or distilled from a reverse osmosis source in our laboratory. All reagents and solvents were used as received, unless noted. All references to room temperature in the procedure refer to a temperature of 21 °C.

Graphite for the flow field plates was obtained from St. Marys Carbon Company as grade 213 resin-infused graphite plates with dimensions: 10.16 x 10.16 x 1.27 cm (4 x 4 x 0.5 in.). End mills with two cutting ends and four flutes made with a cobalt cutting surface were purchased from ENCO in the sizes of 1.27 cm (1/2 in.), 3.18 mm (1/8 in.), and 9.53 mm (3/8 in.) and one that was single end two flute 2.54 mm (0.100 in.) size. All metals were purchased from Onlinemetals.com or acquired from the Chemical Engineering and Mechanical Engineering Shops. The 100 W cartridge heaters were purchased from Omega Engineering. Silicone rubber for the gaskets was purchased from Diversified Silicone Products in sheets. Gas bags for sample collection and GC analysis were purchased from SKC.

Chemical	Source
sulfuric acid	Mallinckrodt Chemicals
n,n-dimethlacetamid (DMAc)	Acros
n-methylpyrrolidone (NMP)	Acros
methylsulfonic acid (MSA)	Acros
1,4-benzendimethanol (BDM)	Sigma Aldrich
glyoxal solution, 40 wt% in H_2O	Sigma Aldrich
glycolic acid, 99%	Sigma Aldrich
glyoxylic acid solution, 50 wt% in H_2O	Sigma Aldrich
oxalate standard for IC, puriss, in H_2O	Sigma Aldrich
formaldehyde solution, 37 wt% in H_2O	Sigma Aldrich
formate standard for IC, puriss, in H_2O	Sigma Aldrich
acetate standard for IC, puriss, in H_2O	Sigma Aldrich
nafion solution, 5 wt% in H_2O and methanol	Sigma Aldrich
glycerol	
methanol	
50 wt% platinum on carbon	FuelCellStore.com
carbon cloth, untreated	FuelCellStore.com
zinc chloride	J.T. Baker Chemicals
hydrogen	Praxair
carbon monoxide and nitrogen	Praxair
nitrogen	Praxair
helium	Praxair
argon	Praxair
platinum foil	Alfa Aesar
platinum wire	ESPI
PEEK	Victrex USA Inc

Table 3.1: List of all chemicals and materials acquired for the ECR research project.

3.2 ECR Reactor Product Analysis

Two analytical tools were used for analysis of partial oxidation products of the ethylene glycol reforming reaction. The gas chromatograph (GC) was located in our laboratory and high pressure liquid chromatograph (HPLC) was located in Forest Resources.

3.2.1 Gas Chromatography

The GC analysis was performed on an Agilent Micro 3000A GC with three available columns: Mol Sieve, Plot U, and OV-1. All calibrations were performed relative to two gas blends from Aglilent: Universal Gas Mixture and Refinery Gas Analyzer Mixture. The detector for the GC was a performance-enhanced thermal conductivity detector (TCD) with a listed accuracy of 0.5% of the concentration. The carrier gases were helium and argon. An example plot of GC data is shown in Figure 3.1.

For components of interest for biofuels, the calibration gases spanned a range of relevant molecules and concentrations listed in table 3.2. These gases were used to make two point calibration curves for each gas of interest to determine the concentration of the unkonwn gases. The columns were baked out periodically for 10-12 hours at 160 °C to remove gases that had adsorbed to the column walls.

Gas	Refinery Gas	Universal Gas
H_2	12.1	0.0987
CO_2	2.99	0.0500
CO	1.01	0.0995
N_2	64.3	0.1000
O_2	4.93	0.0500
CH_4	4.99	Balance

Table 3.2: The concentrations of gases of interest in the two calibration gases from Agilent. The concentrations are shown in mole percent.

There was some variability with the baseline signal from the GC, particularly on the mol-sieve column. This variability was the highest immediately after a column bake out.

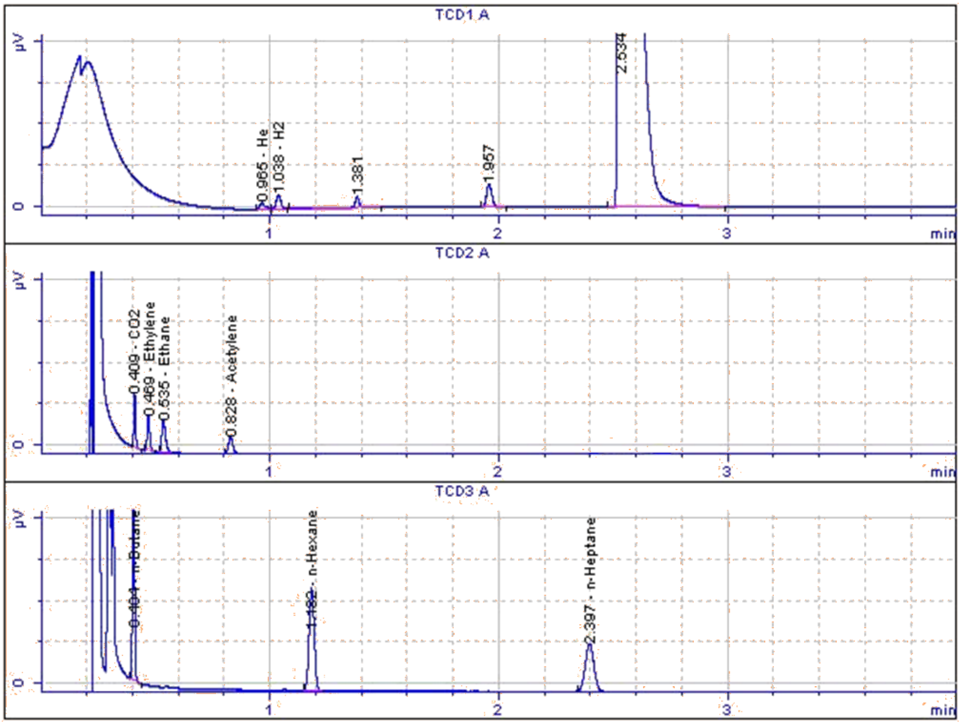

Figure 3.1: An example plot of data showing the separate elution curves of the three columns. The three columns were: (TCD1) Mol-sieve, (TCD2) Plot-U, and (TCD3) OV-1. The detector used in all analysis was a thermal conductivity detector. All peaks, including peak apexes outside the range of the elution curve scale are measured. The large peaks early in the curves are the carrier gas. Peak labels of chemical identity are from calibration gas data.

To circumvent this effect, blank samples were run until the mol-sieve baseline looked reasonable. To ensure the most accurate value for the sample concentrations, atleast three analyses were performed per sample. The procedure on the GC was optimized by changing column temperature and run time to get the most repeatable measurements.

Gas samples were collected in foil SKC gas-tight bags during the experiment. The bag was removed from the ECR reactor system and attached to the GC. First, the bag was placed in ice water to reduce the volatility of any larger molecules that may have entered the bag. Next, the valve was opened and the GC analysis initiated. To ensure adequate pressure for the GC to take a sample, a small weight was placed on top of the bag. At the end of sampling the bags were emptied and flushed with argon gas 5 times to ensure that there were no remaining gases that could contaminate the next sample.

During the analysis of the gas bags, there was consistently the presence of unexplained oxygen and increased nitrogen. There are two possible sources of this problem: (1) air in the connection tubing between the gas bag and the GC and (2) a leak inside the GC that allowed a small amount of air to enter. Due to the variability of this error and the presence of higher then expected N_2 and O_2 in the calibration gases, the most likely source was an internal GC leak. The signal for air was subtracted from all the data.

3.2.2 HPLC Analysis

The HPLC used in the liquid analysis was a Shimadzu Prominence LC with a RID-10A refractive index detector. The column, Phenomenex Rezex RHM H+, was set to a temperature of 63 °C. The mobile phase of the HPLC was isocratic, one solution, of 0.05 mM H_2SO_4 pumped at 0.6 mL min^{-1}. A volume of 20-50 μL of each sample was injected.

There were several standards used in the HPLC analysis: acetic acid, oxalate, formate, formaldehyde, glyoxal, glycolic acid, ethylene glycol, and glycolaldehyde. Three samples; formate, oxalate, and acetic acid; were purchased as ion chromatography (IC) standards and used as is. The remaining liquid samples were diluted to a target of 0.5 g/L. Two samples existed in the powder form and were prepared by dissovling in water. These samples, glycolic acid and glycolaldehyde, were diluted from that dissolution to 0.5 g/L for measurement.

One sample, oxalate, eluded almost immediately after the solvent, making its identity and amount difficult to quantify. We tested cooling the column and decreasing the effluent flow rate to try to increase separation between the two peaks. However these parameters had little impact on the their relative location. Glycolaldehyde and glycolic acid came off the column close together and their peaks overlapped. The areas of their respective peaks were estimated. The remaining samples were easily identifiable and quantifiable.

3.3 Membrane Fabrication

There are multiple steps to the fabrication of a proton conducting membrane of sPEEK. First, the PEEK must be sulfonated to increase its conductivity. Next, the sulfonated sPEEK must be cast into a membrane. Finally, the membrane must be cross-linked and conditioned to remove any remaining casting solvent. The complete step be step process will be discussed in this section.

3.3.1 Sulfonation of PEEK

The PEEK powder was dried in a vacuum oven at 110 °C and a pressure of 10.13 kPa for 2 hours to remove any traces of water. The PEEK was sulfonated homogeneously following a procedure from Do et al. [99]. Five grams of PEEK were dissolved in 25 mL of methylsulfonic acid (MSA) in a vigorously stirred, round bottom flask for 24 hours that was purged with nitrogen and sealed with a rubber stopper. The beige powder turned blood red when mixed with the acid, indicating significant dehydration of the polymer. After dissolution, 200 mL of sulfuric acid (H_2SO_4) was added and the solution mixed for 150-280 hours at room temperature, depending on desired degree of sulfonation. At completion of the sulfonation, the reaction was terminated by precipitation of the sulfonated poly ether ether ketone (sPEEK) in a large excess of ice water. The polymer water mixture was filtered by a glass frit vacuum funnel to remove the solid sPEEK particles from the acidic aqueous phase. The sPEEK was reintroduced to water and filtered as before until the pH was neutral (pH 5-7). The sPEEK product was air dried at room temperature for 1-3 days, and dried in a vacuum oven at 110 °C for 4-6 hours. The resultant products were powdered in a mortar and pestle, and returned to the vacuum oven for about 1 hour. The powdered sPEEK was placed in a vial inside an evacuated desiccator for storage until needed.

The degree of sulfonation of the sPEEK polymer was determined by titration. First the powder was placed in dialysis tubing and soaked in DI water to remove any traces of acid left over from fabrication. Then the powder was weighed and placed in a known quantity of sodium hydroxide for three days. Sodium displaces the proton on the sulfonic acid sites. The solution was titrated with hydrochloric acid to determine the remaining concentration of sodium hydroxide.

$$NaOH_{\text{excess}} + HCl \rightarrow NaCl + H_2O \tag{3.1}$$

$$x = V_{NaOH}M_{NaOH} - V_{HCl}M_{HCl} \tag{3.2}$$

In equation 3.2 the number of sulfonated repeat units in sPEEK molecules, x, was calculated. The volume and molarity are V_i and M_i respectively. The number of non-sulfonated units in sPEEK molecules, y, was calculated from equation 3.3, where W is the mass of the sPEEK sample, and M_s and M_{non} are the molecular weights of the sulfonated and non-sulfonated repeat units.

$$y = \frac{(W - M_s x)}{M_{non}} \tag{3.3}$$

The degree of sulfonation (DS) and ion exchange capacity (IEC) can be calculated from the ratio of the sulfonated and non-sulfonated polymers.

$$DS = \frac{x}{x+y} \tag{3.4}$$

$$IEC = \frac{1000x}{W} \tag{3.5}$$

3.3.2 Membrane Fabrication

The sPEEk was dissolved in n,n-dimethylacetamid (DMAc) or n-methylpyrrolidone (NMP), producing a 2-5 weight percent solution. The membranes were cast by pouring the solution through a glass frit funnel onto leveled glass or ceramic plates and allowing them to air-dry for 3-5 days at room temperature. The glass frit funnel removed particulates that lead to mechanical weakness in the finished membrane.

3.3.3 Crosslinking

The cross-linked membranes were created using a procedure from Fenton et al. [82]. The cross-linked membranes were formed by adding BDM (1,4-benzendimethanol) cross-linker in 10-12 wt% ratios to the sPEEK solution with 1 wt% $ZnCl_2$ as a cross-linker catalyst. These solutions were cast on glass and ceramic plates using the same procedure previously mentioned.

To complete the cross-linking process the membranes were thermally treated. First, the membranes were dried in a vacuum oven at 110 °C for 1 hour. They were moved to a 200 °C oven where they were baked for 15 minutes and quickly quenched in room temperature water. The membranes were then transferred to a 60 °C water bath for 45 minutes. They were removed and placed in a well stirred room-temperature solution of sodium hydroxide (0.5 M) for 30 minutes. The membranes were rinsed thoroughly with water and placed in a room temperature sulfuric acid solution (0.5 M) for 30 minutes. The membranes were rinsed thoroughly and placed in a large volume of water for 4-6 hours, then rinsed and placed in a fresh vat of water overnight to remove any traces of sulfuric acid. Finally, the membranes were placed between paper towel and a moderate weight (about 10 kg) to facilitate drying in a planar orientation.

3.3.4 Physical properties of the membranes

The thickness of membranes was determined with a micrometer. Membranes in the dry state are transparent brown in color. The membranes were checked for pin-holes by placing 12 mm diameter samples between a modified VCR fitting, which has an outside diameter of 9.53 mm and an inside diameter of 6.35 mm, and placed inside a flask of water. Argon gas was pressurized to 137.9 kPa gauge pressure on one side of the membrane and the regulator was closed. Any large membrane holes resulted in bubble formation, smaller holes would lead to a decrease in the static pressure in the system over time. The membrane samples produced here did not have any pinholes.

3.4 Membrane Analysis

To study the impact of experimental parameters, such as casting solvent and membrane thickness, on the stability of the sPEEK membranes, a variety of analytical tools were used. The purpose of these tools was to screen membranes capable of high temperature stability that could be used to form MEAs and tested in the ECR reactor.

3.4.1 Thermal Studies

Differential scanning calorimetry (DSC) was performed using a TA Q200 DSC. The sample, enclosed in a inert atmosphere of flowing nitrogen, was heated to 140 °C at a rate of 10 °C min^{-1} to remove trapped water. The sample was cooled to 0 °C and then ramped to 300 °C at 10 °C min^{-1}.

Thermogravimetric analysis (TGA) was carried out by loading ≈5 mg of each sample into a platinum sample pan and heating in the TA Q50 TGA under a nitrogen atmosphere. The temperature of the sample in the TGA was ramped from 25 °C to 600 °C at a rate of 10 °C min^{-1}.

3.4.2 Conductivity Measurement

For conductivity measurements the ECR reactor was modified. The ECR reactor, which is explained in more detail in chapter 4, is depicted in Figure 3.2. Starting inside, on opposite sides of the electrolyte membrane are two graphite flow field plates, which are supported by aluminum current collection blocks. The aluminum blocks also act as structural support and supply pressure to the system via a ring of bolts. To measure conductivity the electrolyte membrane was removed and replaced with a multi-layer conductivity measurement system, Figure 3.3. The advantage of using the ECR reactor was that the system was already designed to seal high temperature and pressure liquids while measuring current.

The multi-layer conductivity system had outer copper sheets for electrical connection

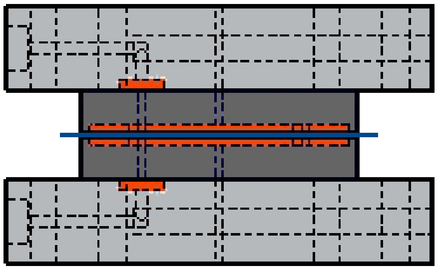

Figure 3.2: Side view of the ECR reactor showing two aluminium support plates which compress two graphite flow-field plates that are separated by the electrolyte membrane.

to the graphite plates. Inside the copper sheets were 2-3 sheets of Teflon for electrical insulation. Inside the Teflon sheets were two platinum foil electrodes supported on Teflon foam for stability. These foil electrodes were electrically connected to each of the copper layers via a platinum wire. On top of the platinum electrodes was the membrane sample of interest. In the case of the 4-electrode set up, two platinum wires were placed on the opposite side of the membrane sample from the foil electrodes. These wires acted as local potential probes removed the iR chop of the test current. The wires passed over an outer silicone gasket, where they were connected to the potentiostat. To ensure that no leaks occurred where the platinum wires contacted the gasket, the wires were sealed between two separate gaskets using a cured liquid gasket material (LOCTITE Copper High Performance RTV Silicone Gasket Maker). This seal was measured effective at 700+ kPa gauge.

There were two orientations for measuring conductivity, (1) along the membrane where the electrodes are on the same side, also known as tangential orientation, and (2) across the membrane where the electrodes are on opposite sides of the membrane, referred to as the normal direction conductivity [70]. Originally, tangential orientation was chosen to probe a larger volume of membrane, which would be more susceptible to changes due to dissolution [100]. However, a paper by Casciola et al. found that tangential analysis was blind to the decay conductivity consistent with high temperature swelling [70].

We performed conductivity measurements in two different orientations, Fig 3.3: two-probe orientation and four-probe orientation. Early work focused on the two probe tech-

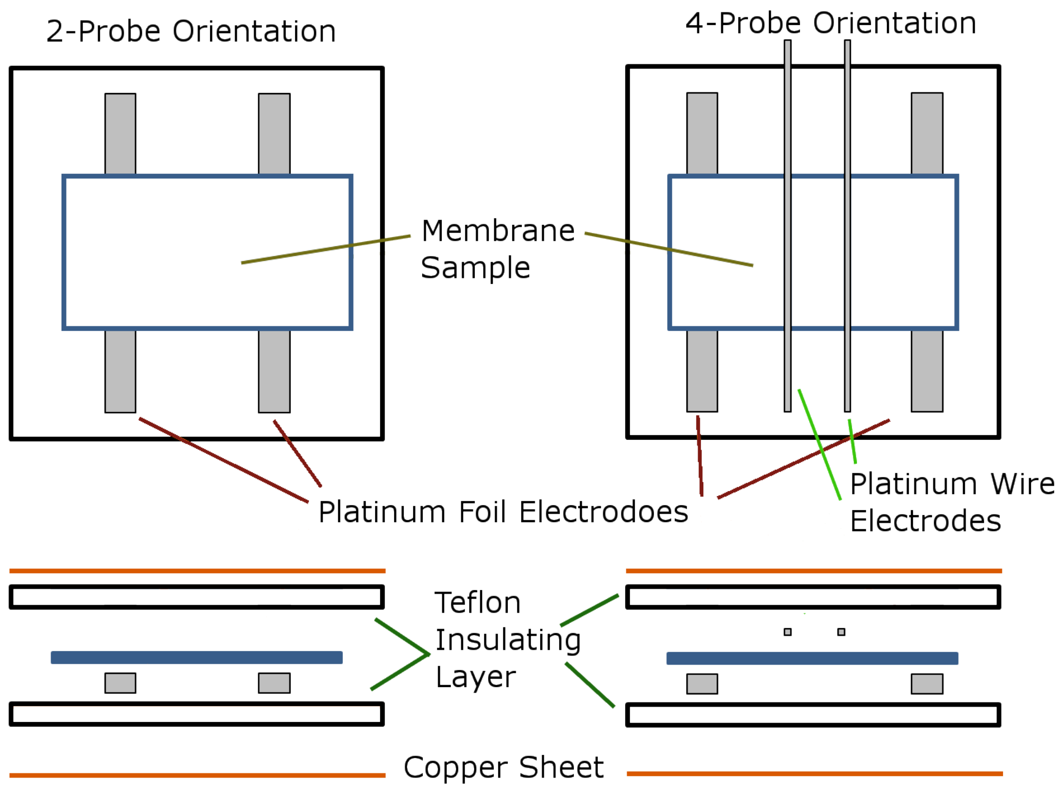

Figure 3.3: Conductivity measurement design sandwich that is placed inside the ECR reactor. The left pair is the two probe tangential conductivity measurement design. The right pair is the 4-probe conductivity design. Shown here is the Teflon sheet with two platinum foil electrodes, membrane sample and in the 4-probe case, platinum wire reference electrodes.

nique because of difficulty incorporating additional electrically independent connections inside the volume of the ECR reactor system. When it was determined that tangential measurements would not work, we modified the set up to the four-probe for normal conductivity analysis. The four-probe conductivity arrangement is preferred because it yields narrower data dispersion and smaller relative errors [101].

Conductivity measurements were performed using electrochemical impedance spectroscopy on a Solatron Instruments SI 1260 frequency response analyzer and a Solatron Instruments SI 1287 potentiostat, fig 3.4. The frequency limits of the sinusodial signals were typically set between 300 kHz and 1 Hz, with an oscillation of 50 mV. The Z' intercept of the Cole-Cole plot was used as the bulk resistance of the membrane sample. The conductivity was calculated from the membrane thickness and active membrane area, eqn. 3.6.

$$\sigma = \frac{L}{R \cdot A} \tag{3.6}$$

Where σ is conductivity ($S \cdot cm^{-1}$), L is membrane thickness (cm), A is electrode area (cm^2), and R is the bulk resistance (Ω).

3.5 MEA Fabrication

Multiple procedures were used to make catalyst ink and membrane electrode assemblies. A brief consultation with Dr. Peter Rieke and Silas Towne at PNNL, was helpful for creation these procedures. The PNNL procedures, for Nafion PEM fuel cell MEAs, were modified for aqueous phase with a sPEEK electrolyte.

3.5.1 Catalyst Ink Procedure

There are two main purposes of catalyst ink: (1) to evenly disperse the catalyst with a high volatility solvent, and (2) to connect the catalyst to the electrolyte via a dissolved ionomer that is recast when drying. The ionomer in the ink needs to be the same as the electrolyte because dissimilar ionomers can lead to bad adhesion of the catalyst layer and contact resistances [102].

First a solution of sPEEK was generated by dissolving sPEEK in NMP to 10 wt% sPEEK.

One gram of 50% Pt/C was placed with a stirring rod in a container with a lid. The catalyst was covered with a small amount of DI water to prevent it from oxidizing the solvent in the ionomer solution. This is because, the high surface area platinum will quickly cause alcohol or solvent vapors to combust without the water. A total 4g of 10wt% sPEEK solution was added to the catalyst along with 10mL of a 50% mixture of methanol and water. The catalyst was stirred for atleast 24 hours and shaken vigorously before painting.

3.5.2 Painting Procedure

There were two types of painting procedures used to make MEAs. The decal method and the direct painting method. The decal method gave bad MEA performance so the direct painting method was used primarily.

Decal Method

Two pieces of carbon paper were cut to the size of the desired catalyst area, 5 cm x 5 cm. The carbon paper used was not teflon treated because there was no need for hydrophobic pores in an aqueous MEA. The catalyst ink was painted directly on the carbon paper and the paper was placed in a 110 °C vacuum oven for 15 min. After weighing to determine the loading, this step was repeated until a desired loading of 4 mg cm^{-2}. After final loading was achieved the decals were dried for 24 hours in the 140 °C vacuum oven.

To complete the MEA the catalyst carbon paper were pressed on to the electrolyte using a hydraulic press. Inside the press the incomplete MEA was placed between a series of layers, from inside out: a teflon sheet, a graphite plate, and layer of silicone rubber. The purposed of graphite and silicone were for force and temperature distribution. The MEA was pressed for 3 minutes with 1,200 lb force and a temperature of 210 °C.

Direct Painting Method

Instead of painting on carbon paper, the catalyst ink was painted directly on the electrolyte membrane. After each painting the membrane was dried in a 95 °C oven for 15 minutes to drive off the solvent. Since both sides were painted simultaneously, the exact loading was difficult to quantify but an average loading of 4 mg cm^{-2} was achieved. The membrane was pressed in a similar way to the decal method with black carbon paper placed over the catalyst. The MEA was pressed for 3 minutes with 1,000 lb force and a temperature of 120 °C.

3.5.3 Protonation Procedure

To ensure a completely protonated membrane after pressing, the membrane was placed in 80 °C 0.5M H_2SO_4 for 4 hours. The membrane was rinsed with DI water and placed it 80 °C water for 4 hours to remove any acid. To dry the membrane it was put between layers of tissue paper and pressed with a moderate mass that maintained planar orientation as it dried. The final MEA was stored in a dry state until needed.

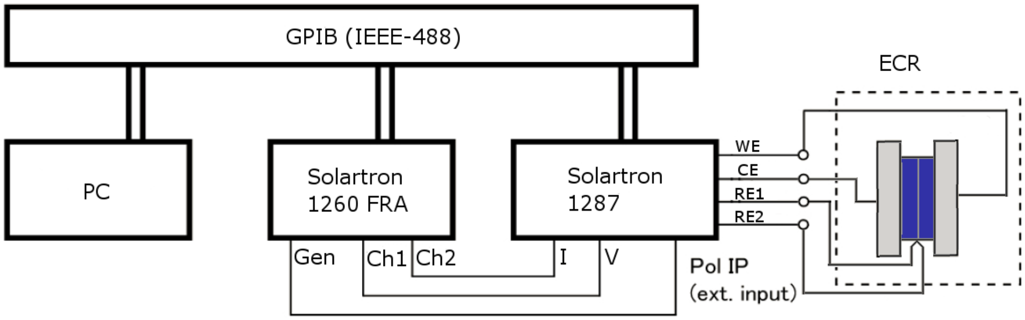

Figure 3.4: Connections for conductivity impedance measurement. The system consists of a Solatron SI 1287 potentiosat and a Solatron SI 1260 FRA.

Chapter 4

ECR REACTOR FABRICATION AND TESTING

The purpose of the electrocatalytic reforming reactor is to study the high temperature electrooxidation of ethylene glycol for formation of hydrogen. Presented here are the design aspects of the reactor and some investigations into parameters important for ethylene glycol electro-reforming.

4.1 ECR System Design Overview

The main design criteria of the electro-catalytic reforming reactor system involved (1) operation with high temperature, high pressure aqueous solutions, (2) membrane electrode assemblies (MEA) suitable for high temperature, and (3) reactor-design to maintain separation, at desired conditions, of reaction products. Table 4.1 lists specific criteria for each of the areas.

Electrolyte
· High temperature stability · Proton conductivity · Product separation (low-crossover) · Oxidation and reduction stability
Membrane Electrode Assembly
· Aqueous transport in diffusion layer · Appropriate catalyst for activity and stability
Reactor Design
· Appropriate heating and temperature control · Electrical isolation of electrodes · High pressure stability · Gas and liquid sample analysis

Table 4.1: ECR System Design Table

The electrolyte, an important design difference between ECR and APR, was necessary for anode and cathode product separation. Additional design criteria included: high temperature stability, high proton conductivity, and stability in simultaneous oxidizing and reducing environments. Product separation, and low-cross of undesirable species, prevented hydrogen gas from reacting with ethylene glycol and partial oxidation products. Hydrogen would readily react with these species under normal ECR conditions, and decrease hydrogen selectivity. The ionomer membrane materials capable of sufficient proton conductivity have temperature limits due to dissolution (Section 2.2), which prevent their inclusion in high temperature experiments. However, the highest possible temperature was needed to improve the reaction kinetics and reduce the necessary overpotential. More discussion on the temperature impacts of the electrolyte will be discussed in chapter 5.

The inclusion of catalyst and diffusion layers, for the formation of the membrane electrode assembly (MEA,) had additional design criteria: aqueous transport in the anode diffusion layer, and appropriate catalyst for activity and stability. Unlike proton exchange membrane (PEM) fuel cells, transport on the anode side of the ECR MEA is completely liquid phase. The Teflon coating, typically implemented to encourage gas pore formation, was removed to maximize liquid phase transport. The electrocatalyst used in the ECR work was platinum on carbon for its well established activity for hydrocarbon oxidation and stability in aqueous phase systems.

In order to investigate ethylene glycol reforming over the range of experimental conditions, gas and liquid sample analysis by gas chromatography (GC) and high pressure liquid chromatography (HPLC) must be sufficiently sensitive to detect partial oxidation products. Aqueous phase reforming observed a low turnover frequency of 1.33×10^{-3} sec^{-1} (0.08 min^{-1}) [2] for ethylene glycol reforming at 498 K. To promote a reaction rate for sufficient measurable products in ECR under an expected low turnover frequency, a high catalyst loading of 4 mg cm^{-2} platinum over 25 cm^{2} was used as the catalyst at each electrode. The samples were collected during 120 minutes constant potential runs to ensure sufficient product formation.

Additional reactor design criteria included: appropriate heating and temperature control, and electrical insulation of both electrodes, and high pressure stability. The ethylene glycol reforming reaction is endothermic, eqn 4.1.

$$C_2H_4(OH)_2 + 2H_2O \longrightarrow 2CO_2 + 5H_2 \qquad \Delta H^{\circ}_{\text{rxn}} = 172.5 \ \text{ kJ mol}^{-1} \tag{4.1}$$

In addition, there is heat loss through convection to the surroundings, conduction into the tubing, and the discharge of heated products. To reach and maintain the temperatures required for the experiments, sufficient heating and insulation were required. To control the temperature, two K-type thermocouples were used, one (TC1) connected to a temperature controller on the heaters and one (TC2) connected to a temperature gauge for manual adjustment of the heating tape and hot plate used for preheating, Figure 4.1. Since the system is designed for high temperature aqueous phase experiments, it had to be designed to withstand the high pressures required to stay above the vapor pressure of water for a given temperature. To test the pressure rating the reactor was sealed from the rest of the experimental system without an MEA, and water was pumped in until the pressure read 2.41 MPa. The system was left for 4-8 hours and the pressure measured again to verify no loss in pressure. The ECR design relied on each side of the reactor to be connected to the electrodes on the MEA. To apply pressure while electrically isolating the sides from each-other insulated bolts were used for the connection.

4.2 ECR System Design

The basic layout for the ECR system can be seen in figure 4.1. The ethylene glycol reactant was pumped via an HPLC pump into the anode side of the reactor. Hydrogen gas was humidified and flowed to the cathode side of the reactor to act as a dynamic hydrogen reference electrode (DHE). The anode side products were collected for HPLC and GC analysis. The cathode side products were vented to the hood for disposal.

4.2.1 Reactant Preparation and Pumping

Prior to the experiments, a one liter solution of ethylene glycol was placed on a stirred hot plate set to 20-90 °C, depending on the final desired temperature, and monitored by a K-type thermocouple. To remove any dissolved gases, argon gas was sparged into the solution at 5-10 SCCM. The pump inlet was below the solution/gas interface, to obtain

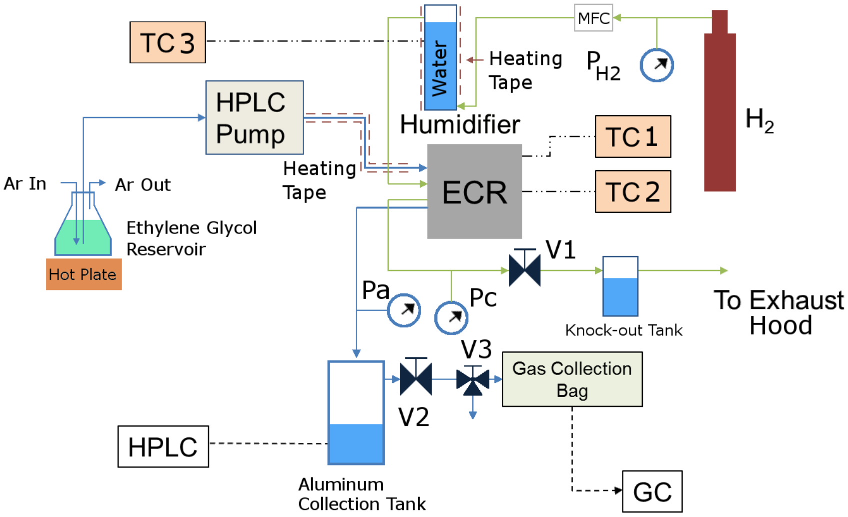

Figure 4.1: A block diagram of the ECR reactor system showing all of the major components. The two outside lines entering the ECR are the inlet/outlet for the anode, the inside lines for the cathode. The cathode exhaust was throttled by a variable control needle valve (V1). The gas exiting the collection tank was controlled by variable control valve (V2) that was left closed except to vent the tank pressure as needed. The T-valve (V3) upstream of the gas collection bag was used to dump pressure into the environment in cases where the bag reached maximum capacity.

the cleanest solution. Argon was pretreated by a gas cleaner prior to use to remove trace compounds that could end up being oxidized in the reactor.

An Eldex Optos series positive displacement HPLC pump was used. The flow rate was set at the pump to a typical value of 4.0 mL min^{-1}. This flow rate was slow enough for measurable conversion of the ethylene glycol, but fast enough that the system pressure would build at an appreciable rate in the collection tank.

For high temperature experiments, above 90 °C, a second heating step was used to bring the solution up to temperature prior to entering the reactor. The stainless steel tubing that transported the fluid into the reactor was wrapped with a 250 W heating tape controlled by a Powerstat variable transformer.

Prior to the humidifier, hydrogen passed through an Aalborg mass flow controller to maintain constant mass flow. Unless otherwise noted, the hydrogen gas mass flow rate was set to 350 SCCM for all runs. The hydrogen gas humidifier was a 3 cm diameter quartz tube approximately 25 cm in length and sealed on both ends. The end plugs included 1/4" Swagelok connections for the flow of gas. Heating tape was wrapped around the quartz tube and insulation was wrapped around the heating tape. The tube was filled 80-90% with water prior to each run. The humidifier temperature was set to 80 °C and controlled by an Omega CN76000 PID temperature controller, TC3. This temperature was chosen to maintain a water partial pressure of about 48 kPa.

4.2.2 Exhaust and Product Collection

A pressurized reactor was required to maintain the operating pressure necessary to prevent boiling off of the reactants. The cathode and anode side had to be independently controlled because allowing one of them to vent would lead to a large pressure difference across the membrane, which could lead to rupture. Initially, both sides were controlled by back-pressure regulators. However, due to the nature of both exhausts being mixed flow, liquid and gas, the back pressure regulator had difficulty with the large viscosity differences and could not adequately control the pressure. The back pressure regulators were replaced with variable control valves that could be modulated to set the pressure.

The cathode exhaust was replaced with a variable needle valve, which was choked to maintain the appropriate experimental pressure on an upstream gauge. The cathode exhaust flowed into a fume hood to prevent hydrogen from building up in the room. The water carried in the cathode exhaust would lead to sporadic increases in pressure downstream of the reactor. To eliminate these pressure swings, a knock-out tank was added directly after the needle valve. This knock-out tank allowed liquid to collect while gases continued to the hood. Before each run the tank was emptied.

The anode exit stream collected in a pressurized collection tank. The collection tank, an aluminum cylinder fabricated at the UW Mechanical Engineering Machine Shop, was 705 mL in volume. The vessel exhaust was controlled by a variable valve that was opened to reduce pressure as needed, but closed most of the time. The exhaust valve was connected to a T-valve, one side exhausted into the environment and the other side exhausted into a SKC foil gas collection bag for GC analysis. The T-valve vented into the environment in cases where the gas bag reached maximum capacity. For start-up, the collection vessel was initially filled with nitrogen gas at the pressure of the system. This allowed the system to run quickly without relying on the pump to build up pressure in the vessel. This nitrogen gas of known quantity, estimated from pressure and volume, was used as a marker for the GC analysis.

The liquid products were collected in the aluminum cylinder after the completion of each experiment for analysis via HPLC. Due to the high heat conductivity of the aluminum cylinder and the low flow rate of hot products, the final temperature of the collection tank was room temperature independent of the operating temperature. This is important for estimates of vapor pressure and dissolved gas concentrations in the liquid, which will be discussed later.

4.2.3 Analytical Tools

There were two analytical tools used to determine the identity and concentration of any partial oxidation and complete oxidation products from the reforming reaction: gas chromatography and high performance liquid chromatography. The tools are described briefly below; for more detailed information see the methods chapter, Chap. 3.

The GC analysis was performed on an Agilent Micro 3000A GC. There are three columns in the system, Mol Sieve, Plot U, and OV-1. All calibrations were performed relative to two gas blends from Aglilent: Universal Gas Mixture and Refinery Gas Analyzer Mixture. The detector for the GC was a performance-enhanced thermal conductivity detector with a listed accuracy of 0.5% of concentration. The carrier gases used in the GC were helium and argon. The system was periodically baked out to remove any adsorbed species on the column walls and return the system to a repeatable baseline.

The HPLC analysis was performed on a Shimadzu Prominence LC with a RID-10A refractive index detector with a Phenomenux Rezex RHM H+ column. Known concentrations of each analyte were run with the experimental samples as standards.

4.2.4 ECR Reactor Design

The ECR reactor, Fig. 4.2, was a modified proton exchange membrane fuel cell design. The electrolyte membrane with catalyst layers was placed between two graphite flow field plates. These plates were supported by larger aluminum blocks that contain the inlet and outlet connections, electrical connections, and apply a compression force to seal the satck with respect to the system pressure. The aluminum blocks had the dimensions of 12.7 cm (5.0 in.) on each side and 3.81 cm (1.5 in.) thick.

Nine 1/4-28 bolts arranged in a ring around the flow field plates applied sealing force. Since the aluminum plates acted as electrical connections, the bolts were insulated from them. The bolts were wrapped in 5-6 layers of Teflon tape and had Teflon washers in contact with the back side of each plate. A metal washer was placed on top of each Teflon washer, and a 7/16 in. nut tightened with a torque wrench, to 15 inch-pound (1.7 Nm), to establish the sealing force on the plates. To insure complete electrical isolation of the bolts, their resistance relative to each plate was checked with a multimeter after each assembly and prior to experiments. A resistance higher than what was measurable on the multimeter (> 6 MΩ), indicated sufficient electrical isolation of the bolts.

Two 100 W heaters were inserted into holes drilled opposite the inlet and outlets. These holes were located in the direct center of the block and were drilled almost all the way through, allowing placement of the heaters in the direct center of each of the aluminum block. To ensure good thermal conductivity, each heater was coated with a high conductivity paste prior to insertion.

The heaters were controlled together by a single Omega CN76000 PID temperature controller. The controller used a thermocouple placed in a small through-hole on top aluminum block. The controller heater was set such that the temperature measured by a Fluke temperature probe in the center of the rector was the desired temperature.

The electrical connection to the potentiostat occurred on side of the aluminum plates as pictured in figure 4.2. An electrical lead was screwed in to the block with a stainless steel screw.

The graphite flow field plates, purchased from St. Marys Carbon, went through several designs and prototypes before settling on the current design, Fig. 4.3. The reactants and products were transported along a single serpentine channel 0.100 in. (0.254 cm) in depth and width. To seal the system at pressure a silicone gasket was placed between the two flow field plates. The gasket sat on series of a designed steps on the block, Figure 4.4. This design distributed forces on the gasket to prevent cuts, but allowed for the concentrated forces necessary to seal the system at maximum operating pressure.

Due to the stresses of threading, the taps required for Swagelok connections could not be cut into the graphite block. To address this issue they were moved into the outer aluminum plate. The inlets and outlets feed from the aluminum plate to the graphite block as shown in Figure 4.2. Gasket grooves for 1.0 in. diameter O-rings were cut into both the graphite and the aluminum plates to seal against the operating pressure.

Sufficient electrical connection between the graphite and aluminum plates was difficult, due to insufficient contact between the plates. To address this problem, conductive copper anti-sieze surface compound was spread on the backside of the graphite block, which improved the conductivity. The surface compound, Kopr-Shield was purchased on-line from Thomas & Betts.

During the ECR operation, stresses on the graphite flow-field plates caused breakages. To prevent further breakages, two flow field plates were constructed out of aluminum.

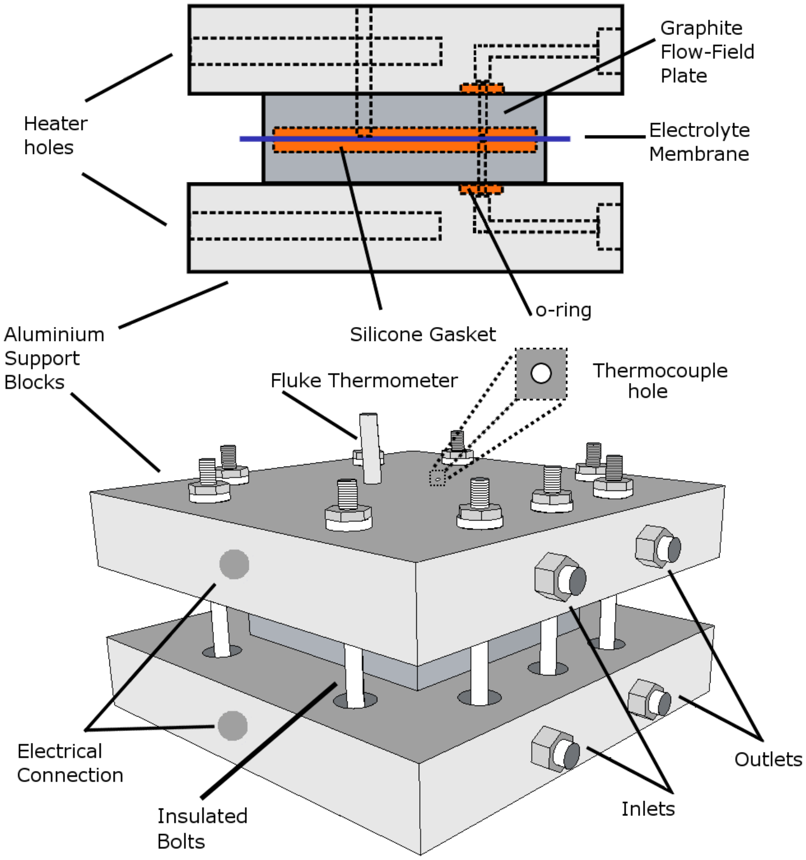

Figure 4.2: Electro-catalytic reforming reactor schematic showing the fully assembled system. The top diagram shows the internal workings of the system. The dashed lines indicate holes that are for heaters, the fluke thermometer, and the inlet/outlet holes. The bottom diagram shows a perspective view of the assembled system. Nine threaded rod bolts ring the reactor to apply even pressure on the graphite flow field plates.

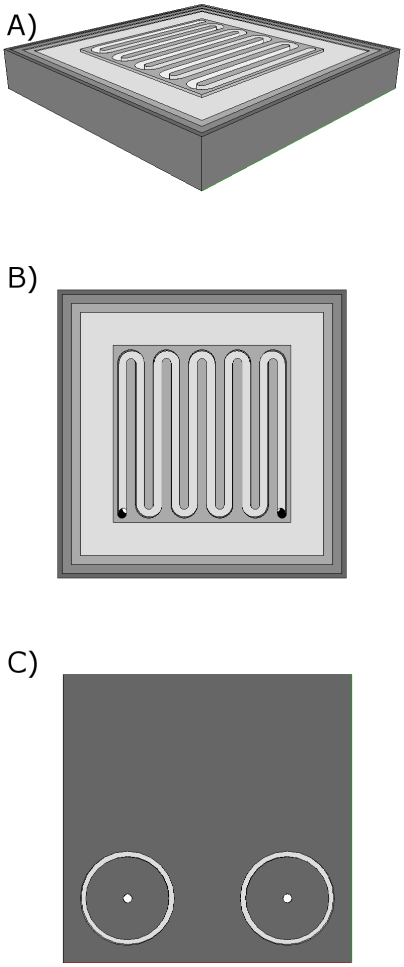

Figure 4.3: Graphite flow field plate depicted in three views: (A) isometric, (B) top, and (C) bottom. The block is 3.25 in. on a side and 0.5 in. thick.

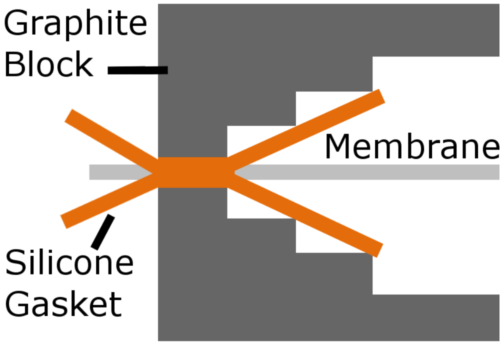

Figure 4.4: An illustration of the gasket steps machined into the flow-field plate to distribute forces on the gasket

However, due to the range of oxidation and reduction potentials occurring in the presence of water the plates quickly oxidized and became insulating. Graphite breakages were therefore dealt with on a case by case basis.

4.3 ECR Reactor Operation

4.3.1 Catalyst Cleaning

The catalyst on the MEAs was periodically cleaned to remove any built up poisons. To clean the catalyst the MEA was placed inside the ECR reactor and the temperature was set to 80 °C. Water was pumped on the anode side and humidified hydrogen was flowed on the cathode side. The voltage at the anode was swept from 0.06 V to 1.16 V and back to 0.06 V continuously at a scan rate of 50 mV s^{-1} until the measured current was repeatable between scans. This cleaning only cleaned the anode side so the system was rewired in the opposite arrangement to clean the cathode after the anode was clean. The MEA was verified clean prior to each day of experiments by sweeping with water until the CV matched a known clean electrode CV.

4.3.2 Cyclic Voltammetry

In cyclic voltammetry the potential difference between the working electrode and counter electrode is linearly ramped with time and the resultant current measured. This potentiodynamic measurement can investigate the time constants of adsorption, desorption, oxidation, reduction reactions [46]. Typically. the scans were performed between 0.06 V_{RHE} and 1.16 V_{RHE}. Various scan rates including 10 and 25 mV s^{-1} were examined.

4.3.3 Constant Potential

Potentiostatic measurements were used to discriminate between potential and time effects on the ethylene glycol electro-oxidation reaction. The procedure, adapted from Behm et al. [4], started with a system that had reached a steady state based on repeatable cyclic voltammetry measurements. The potential was held at 0.06 V_{RHE} for 20 seconds, then instantly it was changed to the potential of interest and held at steady state for 120 minutes. By starting at the same conditions prior to the step change, the same surface coverages of adsorbed species were present independent of the probed potential [4].

The steady state current value of each potential can be used to determine kinetics at a given applied potential. Multiple measurements across different temperatures can be used to determine the potential dependent apparent activation energy for the ethylene glycol reaction.

4.4 Experimental Procedure

To investigate scan rate and and reactant concentration effects, two experiments were performed. First, cyclic voltammetry was carried out at 60 °C, 80 °C, 90 °C and 100 °C with a scan rate of 10 mV s^{-1} and a concentration of 0.02 M ethylene glycol, Fig. 4.5. The second cyclic voltammetry experiment was performed at 60°C and 100°C with a scan rate of 25 mV s^{-1} with concentrations of 0.01, 0.05, and 0.1 M ethylene glycol, Fig 4.6. A pressure of 103 kPa gauge was applied for the 100°C experiments to guarantee liquid phase reactions.

4.5 Sample Results

At low potentials, electrooxidation was inhibited by the presence of adsorbed CO on the surface of the platinum [40, 103]. The onset potential, the potential at which sustained electrooxidation occurs, as a function of temperature can clearly be seen on Fig. 4.5. The onset potential at 333 K is approximately 0.35 V. As the temperatures, increase the onset potential shifts in the cathodic direction. At 80 and 90° this potential is about 0.32 V; at 373 K the onset potential is 0.3 V. The observed cathodic shift of the onset potential agrees well with previous studies [40, 61, 104]. At potentials above 0.7 V, the electrooxidation reaction rate is progressively suppressed by the presence of a second surfaces species, most likely OH groups [24].

For the lower temperatures two distinct oxidation peaks were visible in Fig. 4.5, I and II. At 60 °C the peaks were at 0.54 V and 0.58 V, respectively. As the temperature increased the first peak shifted in the cathodic direction. At 80 °C this peak is at 0.52 V and peak II remains at 0.58 V. As the temperature increased further, peak I became dominant and obscured peak II. At 100 °C the peak is at 0.50 V. The location of these peaks differs slightly from literature values [3, 105]. This could be due to differences in electrochemical system, reference electrode, or scan rate. There is a decrease in current around a potential of 0.75 V, characteristic of OH adsorption [106]

The two distinct oxidation peaks seen at the lower scan rate and concentration of Figure 4.5 are not visible with the faster scan rate of 25 mV s^{-1} in Figure 4.6. The peak locations of the faster scan match well with literature values [3, 4, 105]. The decease in current, characteristic of OH and seen with the slower scan rate, is significantly diminished with the faster rate. It is more pronounced in the lower temperature case, while almost non-existent in the 100°C data.

Studies looking at the impact of increasing scan rate saw the emergence of an oxidation peak at about 0.6 V_{RHE} with increasing scan rate [46]. Our cyclic voltammegrams are inhibited in the positive sweep at that potential, but the negative sweep of the 60 °C 0.1 M run in Figure 4.6 shows a dramatic increase. The broad nature of this peak could be due to the Pt/C catalyst used instead of a polished platinum electrode [46].

For concentration impacts, the 100°C data at 0.6 V increased from 0.1 A to about 0.2 A with a 10 fold increase in ethylene glycol between 0.01 and 0.1 M. For the 60 °C case the current increased from 0.06 to 0.075 A over the same range of concentrations. The difference may indicate mass transfer limitations in addition to kinetic differences.

4.6 Conclusions

We have presented here the fabrication and operation of the electrocatalytic reforming reactor. Using the reactor to study the reforming reaction of ethylene glycol, we were able to replicate oxidation peaks seen in the literature and show similar trends for scan rate and concentration.

We can see from the potentiodynamic measurements that even at 100 °C the rate of ethylene glycol electrooxidation was suppressed in the low potential region below 0.5 V. The predicted trend for reforming ethylene glycol is that lower potentials have a higher CO_2 selectivity. The CO_2 selectivity is higher because the surface is blocked by CO. Whatever reaction does occur is a reaction does not produce a CO intermediate and therefore goes directly to CO_2. Additional information about the kinetics and the products formed are needed to complete the understanding of the ethylene glycol reforming reaction. These issues will be address in Chapter 6.

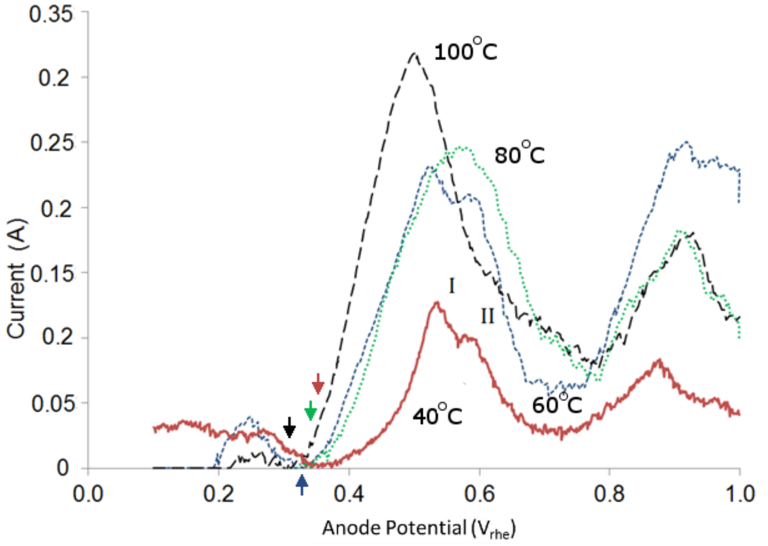

Figure 4.5: Cyclic voltammetry recorded at four different temperatures, 60°C, 80°C, 90°C, and 100°C, with a scan rate of 10 mV s^{-1}. The concentration of ethylene glycol was 0.02M. The data were corrected for pseudo-capacitance due to double layer charging. The arrows illustrate the shifting onset potential

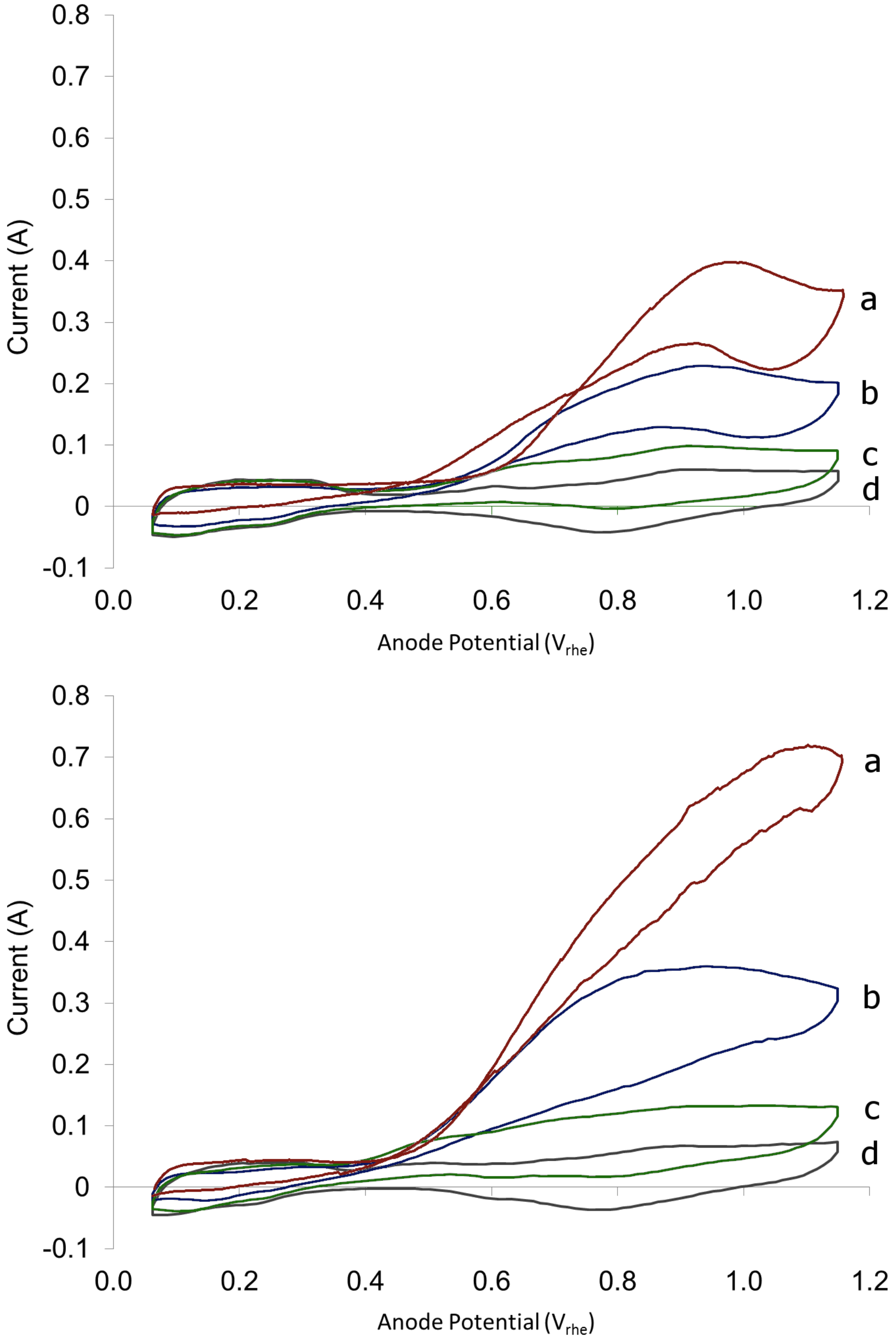

Figure 4.6: Cyclic voltammetry recorded at three concentrations of ethylene glycol, (a) 0.1 M , (b) 0.05M, and (c) 0.01M shown with (d) water. The scan rate is 25 mv s^{-1}. The top graph is at 60°C and the bottom graph was at 100°C.

Chapter 5

FEASIBILITY OF SPEEK MEMBRANES FOR ECR APPLICATIONS

5.1 Introduction

Since APR occurs at temperatures of 200 °C and pressures of 1.6 MPa, it is reasonable to begin ECR studies in this range of conditions. A main advantage of ECR is the use of an electrolyte membrane to separate reactants from hydrogen. An electrolyte membrane that is stable at these high temperatures in aqueous phase is needed. The dominant electrolyte membrane material is Nafion. Unfortunately, the maximum operating temperature for Nafion electrolyte membranes is 120-150 °C [70].

An alternative to Nafion is sulfonated poly-ether-ether-ketone or sPEEK. However, sPEEK membranes have a lower dissolution temperature than Nafion and will irreversibly swell in boiling water [107, 108]. To improve its resistance to dissolution, Fenton et al. developed a Fridel-Crafts cross-linking reaction with benzene di-methanol and observed noticeable increases in membrane stability. They measured no mass loss on membranes after boiling them in different solvents, including water, dimethylacetamide(DMAc), and n-methyl-2-pyrrolidone(NMP) [82]. Their theory is that cross-linking decreases water uptake and restricts the dimensional change of sPEEK.

Casting solvent also affects the stability of sPEEK membranes [94, 95, 99, 109]. One solvent, dimethylformamide (DMF), has a direct negative impact on the stability of the sPEEK membrane [99]. Jun et al. found that soaking a DMF cast membrane in sulfuric acid improved its stability relative to a non-soaked membrane [94].

The objective of this work is to investigate the stability of Friedel-Crafts, cross-linked, sPEEK electrolyte membranes in high temperature aqueous phase environments. To do this we want to look at the thermal stability of the membrane using thermogravimetric analysis (TGA) and differential scanning calorimetry (DSC), as well as its resistance to dissolution by measuring the conductivity of the membrane under reactor operating conditions. Finally, we want to produce a sPEEK membrane electrolyte assembly and test it under ECR operation.

5.2 Results & Discussion

5.2.1 Thermal Stability Measurements

Thermogravimetric analysis was performed to determine the temperatures that the membranes exhibit mass loss. Figure 5.1 shows the TGA of four sPEEK samples and the original PEEK sample. The sPEEK samples represent two different casting solvents (DMAc & NMP), with and without sulfuric acid cleaning, and with and without cross-linking. A clear impact of casting solvents can be seen in the low temperature region. The decrease in mass between 100 and 150 °C of the NMP membranes may be due to loss of residual solvent. NMP would be expected to have a larger mass of residual solvent because it is less volatile than DMAc. NMP has a boiling point of 202°C and DMAc has a boiling point of 165 °C [110].

The mass loss at the first onset (I) is the thermal scission of the sulfonic acid groups that were added during sulfonation. The slight increase of onset temperature for the DMAc membrane without cross-linking may be related to its ability to swell before breaking bonds. Over this range of temperatures, however, it lost more mass which may be related to decreased stability when swollen. There is no evidence to support the hypothesis that the sulfuric acid cleaning will improve the stability of the membrane. Instead the cleaned membrane lost more mass after the first onset.

The second mass loss onset (II) is the breakdown of the PEEK backbone. Compared to unmodified PEEK, all of the sPEEK samples exhibited a decrease in temperature for the second onset. This may be due to a reduction in strength of the polymer matrix after sulfonation. The faster mass loss of the non-cleaned NMP sample, compared to the cleaned NMP sample, may be evidence of a weakened polymer structure from the larger initial presence of casting solvent. the DMAc membrane, which had not been cleaned, did not show evidence of this increased breakdown rate. There are noticeable impacts of the casting solvent and cleaning by sulfuric acid in the TGA data. However, all the membranes were stable above the 200° goal for the ECR.

For phase change information differential scanning calormetry was performed, fig. 5.2. The same four sPEEK samples as TGA are plotted. There is a slight decrease in heat flow around 160 °C for all samples, which is likely the glass transition temperature for the sPEEK. A notable decrease in heat flow around 200 to 280 °C is a crystallization of the sPEEK. After about 280 °C the samples show the system acting endothermic which may be the loss of sulfonic acid groups visible in the TGA.

The DSC showed no noticeable impact of the cross-linked or sulfuric acid cleaned samples on the heat flow. This indicates that the casting solvent and the sulfuric acid cleaning are not impacting phase change information visible to the DSC measurement. The crystallization peak indicates that the maximum operating temperature for these membranes is below about 200 °C because crystallization dramatically decreases proton conductivity.

5.2.2 Conductivity Measurements

The thermal stability measurements did not exclude any materials from ECR applications. This is an unexpected result because Fenton et al. had observed non-cross-linked sPEEK membranes becoming irreversibly swollen in boiling water. The only explanation is that resistance of the membrane to dissolution is not measurable by DSC or TGA. To simulate ECR conditions, we tested the conductivity of these membranes in high temperature and high pressure aqueous environments to find a measurement capable of seeing dissolution stability.

For appropriate determination of the conductivity from impedance measurements the thickness of the membranes was needed. Due to the fabrication nature of the membranes, there was a thickness distribution across the membrane, Tbl. 5.1. The mean value of the membrane thickness was used in the calculation of the conductivity of the sample. About 10-15 measurements made by a micrometer over the entire cross-section of the membrane sample, including edges and interior, were used to determine these values.

The conductivity tests were two-probe measurements along the length of the membrane with the electrodes located on the same side of the membrane. The conductivity

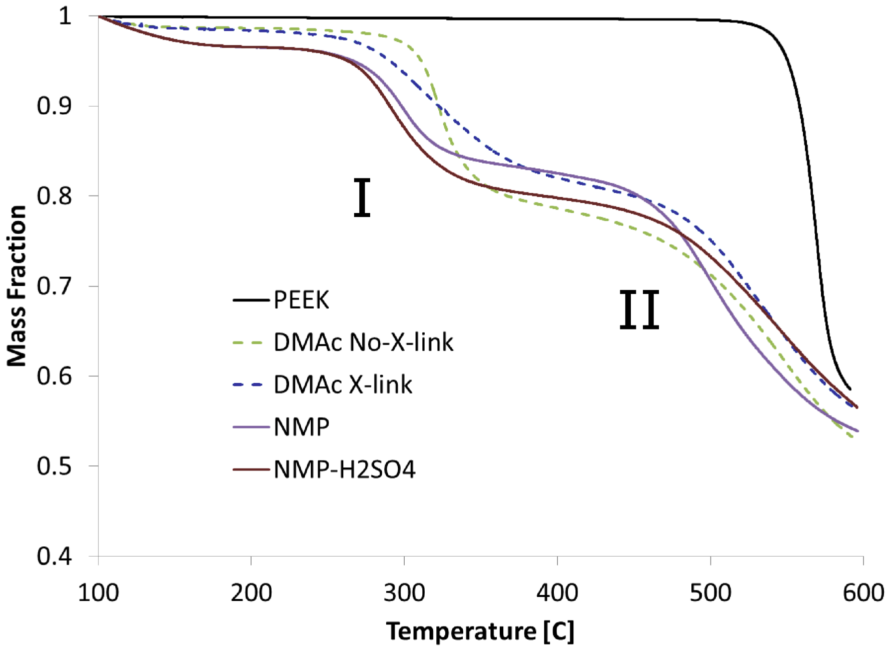

Figure 5.1: Thermogravimetric analysis of four sPEEK samples and original unmodified PEEK. The two onset temperatures (I & II) represent sulfonic acid group scission and PEEK backbone breakdown, respectively.

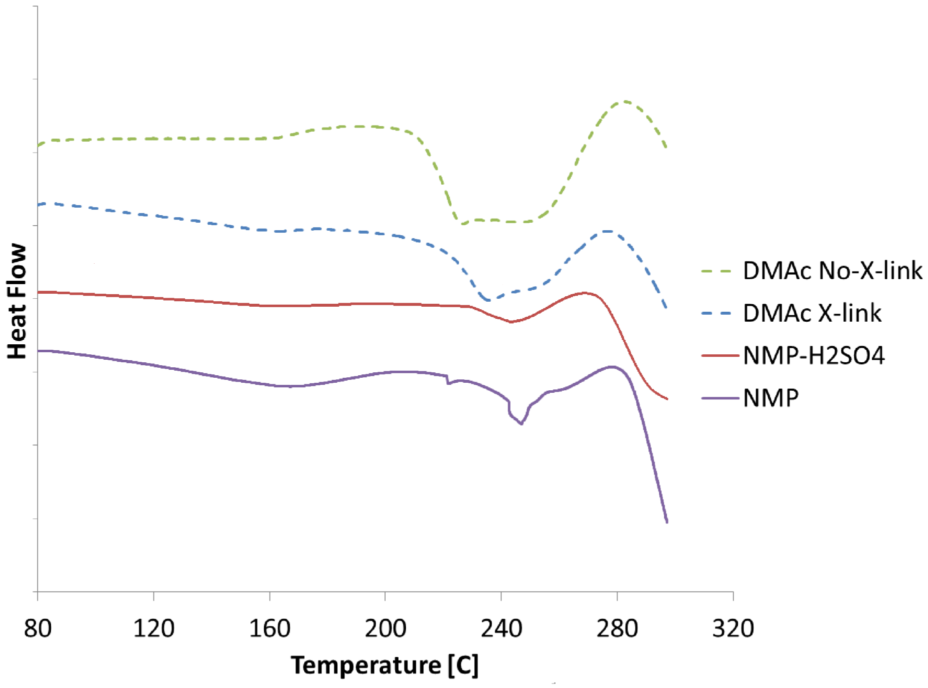

Figure 5.2: Differential scanning calorimetry measurements of four sPEEK samples. The heat flow of each sample has been offset to minimize data overlap.

Name	DMAc No X-Link	NMP	NMP H_2SO_4
Mean	31.8	81.7	53.0
Standard Deviation	7.18	43.9	22.0

Table 5.1: Thickness of membrane samples, μm

results in fig. 5.3 show a clear distinction between the DMAc sample that was not cross-linked and the two NMP samples. All the the sPEEK samples were tested by starting at low temperature and slowly increasing the temperature. The membranes were tested over about a 4 hour period of increasing temperatures.

The significant rise in conductivity of the sample without cross-linking illustrates the swelling and increased water incorporation into the membrane between 360-380 K. A similar trend is evident with the NMP sample between 370-400 K, but there were few data points in that range. The cleaned NMP membrane shows no evidence of this swelling trend. The cleaned NMP membrane had a nearly equivalent slope to its conductivity data as Nafion 117. This could mean similar water uptake mechanisms in both materials. The activation energies calculated from the slope of the least squares regression are: 18.9 kJ mol^{-1} for DMAc No x-link, 8.9 kJ mol^{-1} for NMP H_2SO_4, and 9.2 kJ mol^{-1} for Nafion. The best fit line for the NMP data set was nearly horizontal, so it was replaced with a horizontal line.

The conductivity data implies sample stability of the sulfuric acid cleaned NMP membranes out past 160 °C. However, when the samples were removed for inspection, they showed irreversible swelling charateristics. This indicates the 2-probe along the surface conductivity measurement of the membranes is not showing impacts of dissolution. This result was corroborated by work of Casciola et al. [70] that were able to only measure conductivity decay with electrodes on opposite sides of the membranes.

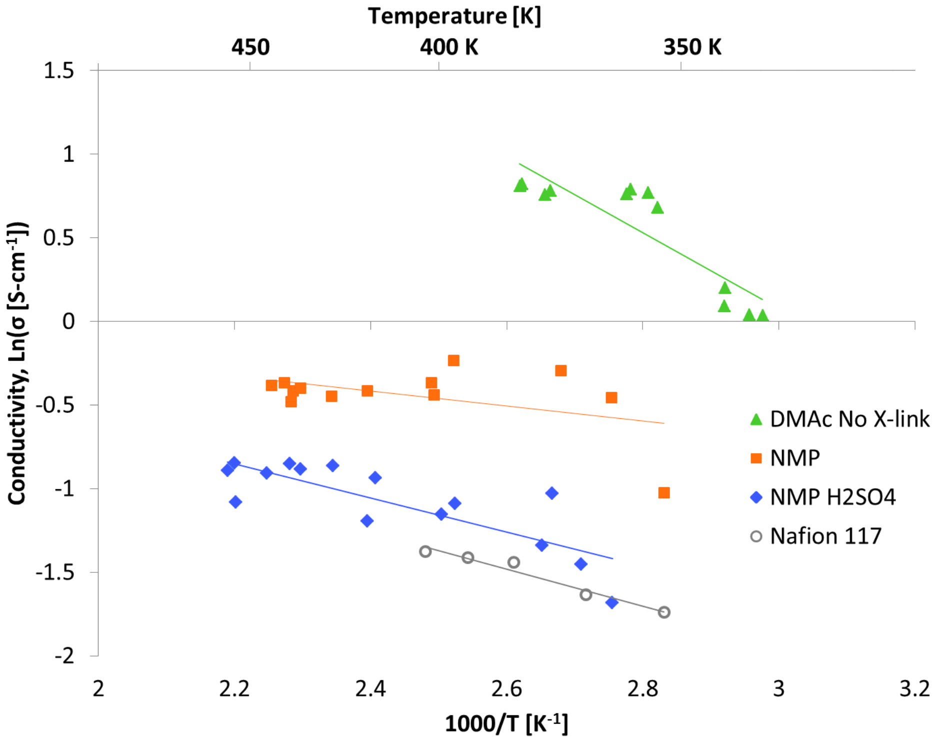

Figure 5.3: Two-probe, tangential, conductivity measurements on three different sPEEK membranes. The sPEEK membranes are compared to Nafion 117 data from Casciola et al. [70]

5.2.3 MEA Testing

To test the sPEEK membrane as an electrolyte, it was fabricated into a MEA. A NMP membrane that had been cleaned by sulfuric acid, was fabricated with 4 mg cm^{-2} loading of platinum by the direct painting method. The results of cyclic voltammetry with water at the anode and hydrogen at the cathode, at a temperature of 60 °C, are shown in Figure 5.4. The impact of contact resistance is significant (about 95 Ω cm^2) and is likely due to poor catalyst layer adhesion with the electrolyte membrane.

5.3 Conclusions

The results for the stability of Fridel-Crafts cross-linked SPEEK membranes indicate they are not sufficiently stable in high temperature aqueous environments for application in the ECR. The membranes do not burn or melt, but lose stability due to dissolution. We were unable to see the exact temperature of dissolution, however observations at 160° indicate that the membranes dissolved partially.

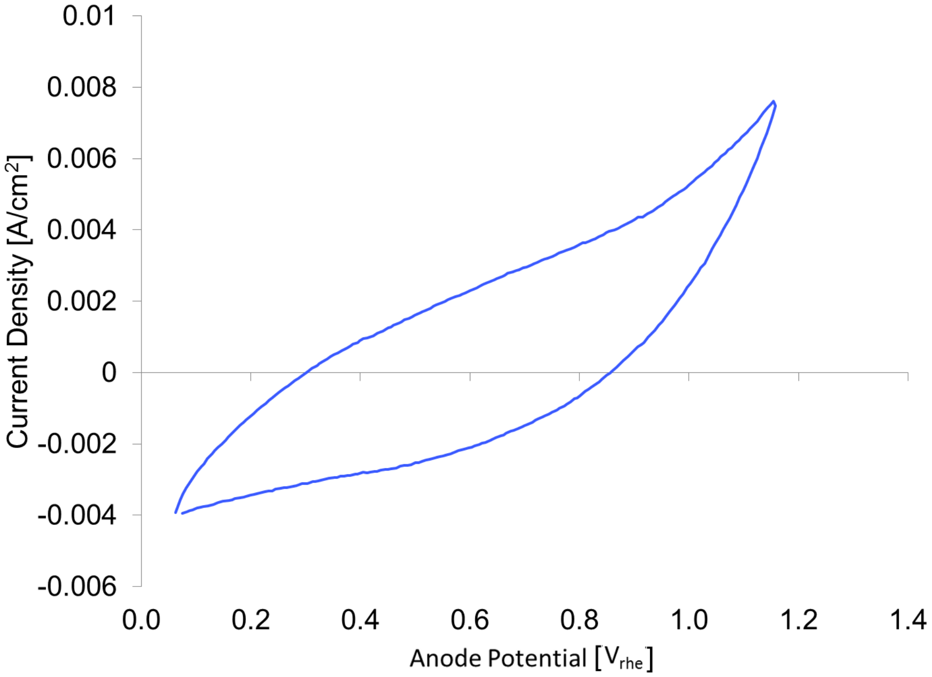

Figure 5.4: Cyclic voltammogram with a SPEEK electrolyte membrane at 60 °C in water.

Chapter 6

ECR ELECTROCHEMISTRY

6.1 Introduction

Electrocatalysis for biomass oxidation has been evaluated for a number of applications including direct alcohol fuel cells [111,112]. The limiting factor in complete breakdown of biomass into hydrogen and carbon dioxide is the breaking of C-C bonds [112]. Without complete breakdown of biomass, an electrocatalytic route for biomass to hydrogen is not economically viable.

Here, we present work to evaluate ECR as a route to convert biomass-derived compounds into hydrogen. Out model molecule is ethylene glycol due to its C-C bond and OH groups on each carbon. Evaluation of the potential of ECR a includes the following characteristics:

1. The potential required to sustain ethylene glycol electrooxidation as a function of temperature;
2. The apparent activation energies for the ECR reaction and CO_2 formation;
3. A complete mass balance including partial oxidation products and hydrogen yield;
4. Extent of C-C bond breakage and utilization of ethylene glycol;
5. Extent of complete oxidization at temperatures of 130-150 °C and a potential of 0.5 V; and
6. Comparison of ECR with APR.

6.2 Methods

The methods used in this research were presented Chapter 3. To accomplish the objectives of evaluating ECR we performed two types of measurements potentiodynamic measurements and potentiostatic measurements. In potentiodynamic measurements we linearly ramp the voltage as a function of time to evaluate the potential of different oxidation reactions. This measurement is also known as cyclic voltammetry. In potentiostatic measurement, the potential is held for a significant amount of time to evalute the reaction without time effects. This is used to determine the reaction kinetics and activation energy and to generate sufficient products to test by analytical tools.

6.3 Results & Discussion

6.3.1 Potentiodynamic Measurements

Cyclic voltammetry scans in the forward and reverse directions are shown in Figures 6.1 and 6.2, respectively. The scans were performed with 0.1 M ethylene glycol on a Pt/C catalyst with 4 mg cm^{-2} Pt loading, a catalyst area of 25 cm^2, and a Nafion electrolyte, at different temperatures. All temperatures have no current at low potentials, less than 0.3 V, which is characteristic of CO adsorption. The ignition point, where sufficient CO is oxidized and sufficient surface sites are available to oxidize ethylene glycol, occurs at about 0.45 V at 40°C and decreases to about 0.3 V at 137°C. Other studies that have observed CO adlayer oxidation also at 0.35 V [4, 104, 106, 113]. The calculated reversible potential of ethylene glycol reforming at 120°C and a system pressure of 241 kPa is 0.0583 V.

Interestingly, as visible in the 40°C scan, adsorbed carbon monoxide can be oxidized without sufficient potential to sustain ethylene glycol oxidation. The current increases at 0.35V and decreases again at 0.63V before increasing and sustaining oxidation. This decrease at 0.63V could be due to depletion of adsorbed CO, but is more likely related to a blocking of surface sites by the adsorption of ethylene glycol. Studies of methanol oxidation at room temperature on platinum saw a similar phenomenon, where sustained oxidation occurred above 0.65V and non-sustained oxidation was possible at lower poten-

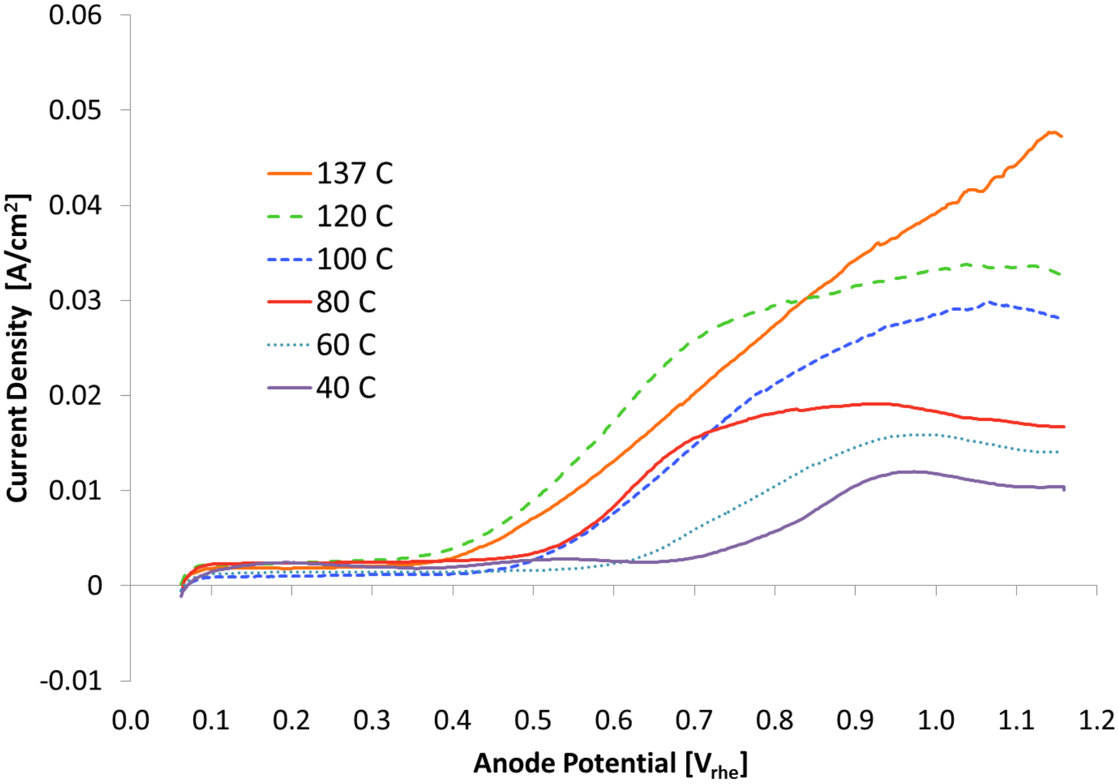

Figure 6.1: Forward sweep of cyclic voltammograms recorded at 25 mv s^{-1} with 0.1 M ethylene glycol on Pt/C catalyst with a loading of 4 mg cm^{-2} Pt and a Nafion electrolyte. Six temperatures of ethylene glycol electro-oxidation are illustrated: 40, 60, 80, 100, 120, and 137 °C. The arrows reflect the onset potentials for each temperature.

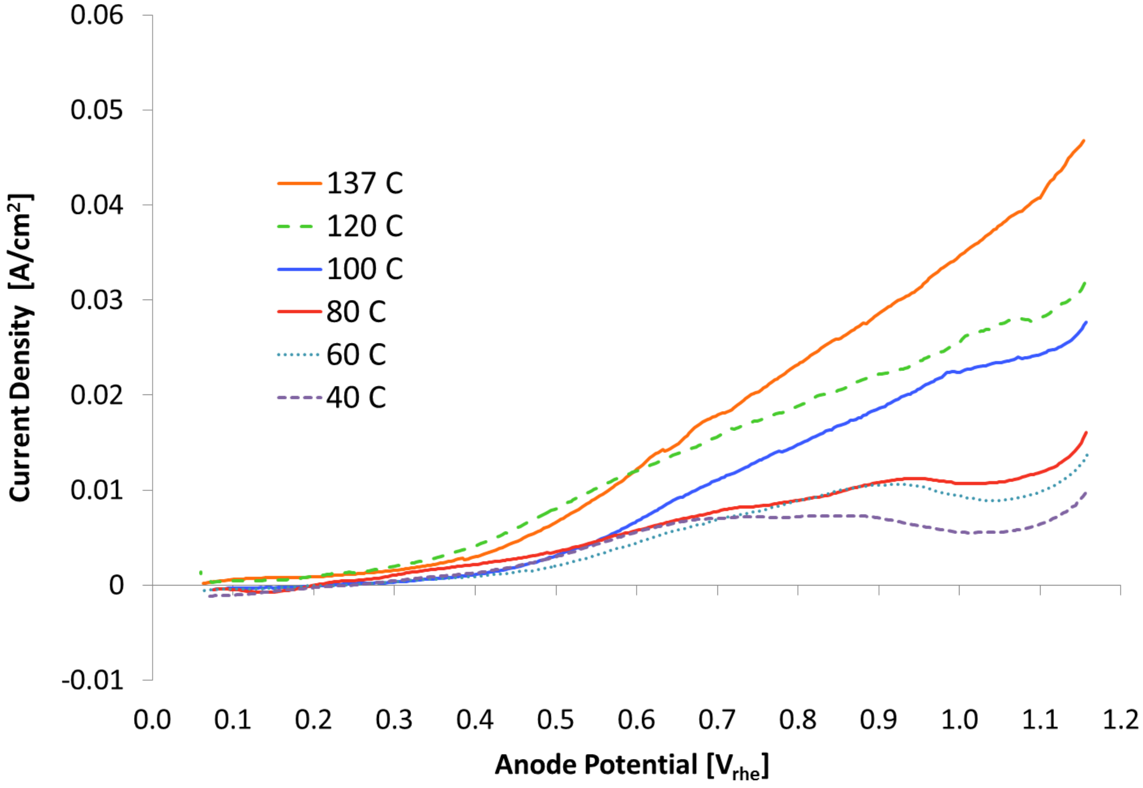

Figure 6.2: Reverse sweep cyclic voltammograms at 40, 60, 80, 100, 120, and 137 °C. The reactant concentration of ethylene glycol was 0.1 M ethylene glycol and the MEA was Pt/C catalyst with a loading of 4 mg cm^{-2} Pt and a Nafion electrolyte.

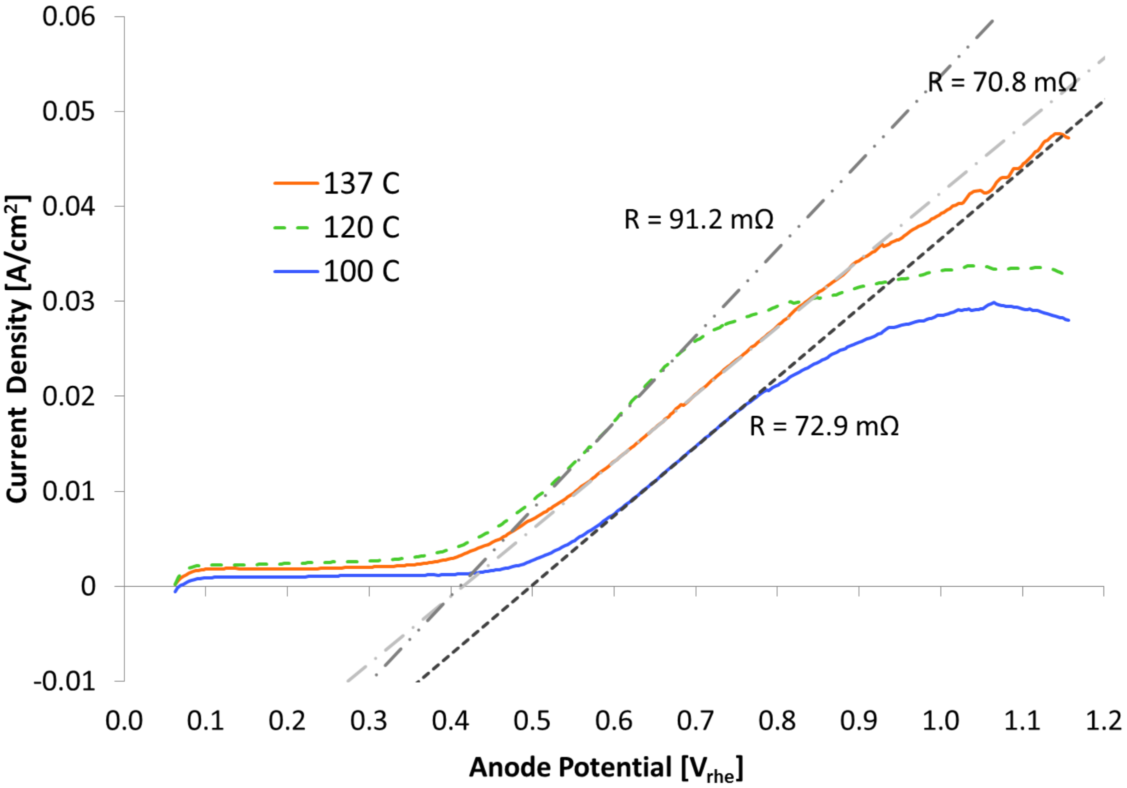

Figure 6.3: Forwards sweep cyclic voltammograms showing the impact of contact resistance on the current output from the ECR reactor. The resistance is related to the compression applied to the assembly of the ECR reactor and not related to temperature. The system is 0.1 ethylene glycol on Pt/C catalyst with a Nafion electrolyte.

tials [114].

Contact Resistance

capacitance

There is a limiting slope noticeable on the forward scan cyclic voltammetry of Figure 6.1, which is shown in more detail in Figure 6.3. The limit is due to contact resistance that results from the design of the ECR reactor.

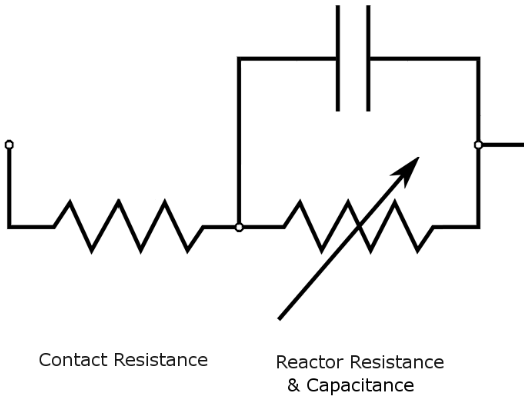

Figure 6.4: Contact resistance circuit representation.

The contact resistance acts as a resistor in series with the electrochemical reaction which can be represented as a variable resistor, Figure 6.4. The cyclic voltammetry measurements only measure the full system resistance, which is a combination of the resistance of the reaction and the contact resistance, eqn. 6.1.

$$R_{\text{system}} = R_{\text{contact}} + R_{\text{reaction}} \tag{6.1}$$

In potentials where the reaction would ordinarily have a high current density, the effective resistance of the reaction drops so the contact resistance dominates the measured system resistance and a limiting slope on the CV curve is seen. From this limiting slope the contact resistance is between about 11.5 Ω cm^2 to 14.0 Ω cm^2.

Contact resistance problems in fuel cell systems are not uncommon. There are many known sources of contact resistance in PEM fuel cell systems including: flow-field plate connection to the system [115], and gas diffusion layer compression resistance [116]. The combination of contact resistances is typically 0.02 - 0.2 Ω cm^2 for an estimated value of 8x10^{-1} to 8 mΩ for a 25cm ^{2} area system like the ECR reactor [115, 116].

Potentiodynamic Information

Lower temperature scans show a decrease in oxidization current possibly characteristic of OH adsorption visible in the potential range of 0.95 to 1.1 V. This is more noticeable in the reverse scan, Fig. 6.2. Behm et al. [4] also observed a similar decrease but at a potential of 0.8 V. Their decrease was more significant on the overall current, which may be related to larger surface area, or on the contact resistance.

Also visible is a cathodic shift of the onset potential of ethylene glycol as the temperature increases, Tbl. 6.1. The setdown potential, the potential for the intersection of the reverse scan with the double layer current, is smaller than the onset for each temperature. The similarity between the onset and setdown potentials at temperatures over 100 °C indicate less of an influence of CO poisoning on the forward scan. The cathodic shift of the onset has been seen in the oxidation of adsorbed carbon monoxide [105, 117]. In addition, Behm et al. [4] observed that the potential of complete oxidation of ethylene glycol shifted lower in potential with increased temperature.

Temperature, °C	Onset, V	Setdown, V
40	0.70	0.43
60	0.62	0.47
80	0.50	0.39
100	0.53	0.48
120	0.43	0.31
137	0.42	0.39

Table 6.1: Onset and setdown cell potentials for ethylene glycol ECR

Other researchers have observed a second oxidation peak for room temperature ethylene glycol electrooxidaiton, at a potential of about 0.9 V versus RHE [62,104]. The absence of the second oxidation peak could be due to not probing a wide enough potential range or the minimization of the decease associated with OH adsorption.

Other researchers have seen a significant anodic oxidation peak when reversing the scan of ethylene glycol electrooxidaiton on single crystal platinum [62]. We did not observe this peak to the same extent. There are indications that this peak does exist on the low temperature scans but its size is significantly reduced. This may be related to mass transport limitations.

6.3.2 Potentiostatic Measurements

To determine the apparent activation energy of ethylene glycol electro-oxidation and to generate products for analysis we performed potentiostatic measurements over a range of temperatures and potentials. The procedure, which is summarized in chapter 3, involves starting the scan at a potential of 0.06 V, performing a step change to the potential of interest, and holding for 120 minutes. This allows for a standard starting state across the potentials with a catalyst that is partly covered by a layer of adsorbed carbon monoxide [4].

Figure 6.5 shows current transients from the potentiostatic measurements. An unexpected result of the 137 °C data is a periodic increase in current. These local maxima occur between 25-35 seconds apart independent of potential and are approximately 6% larger than the sustained current floor. The pump, which has a flow rate of 4.0 mL min^{-1}, pumps at a regular rate of once per second. This is unlikely to be the source of this current change. Our hypothesis is that this periodic rate is related to bubbles or droplets in the system.

The steady-state current is used to calculate the apparent activation energies for the overall reaction, Fig. 6.6. The CO_2 formation apparent activation energy is calculated from the amount of current that can be attributed to the CO_2 formation. The apparent activation energy calculated for 0.5 V and 0.7 V are 20 kJ mol^{-1} and 17 ± 2 kJ mol^{-1}, respectively, over the temperature range of 40-137°C. The apparent activation energy for CO_2 formation is 43 kJ mol^{-1} and 30 ± 5 kJ mol^{-1} for 0.5 V and 0.7 V respectively. The error at 0.5 V

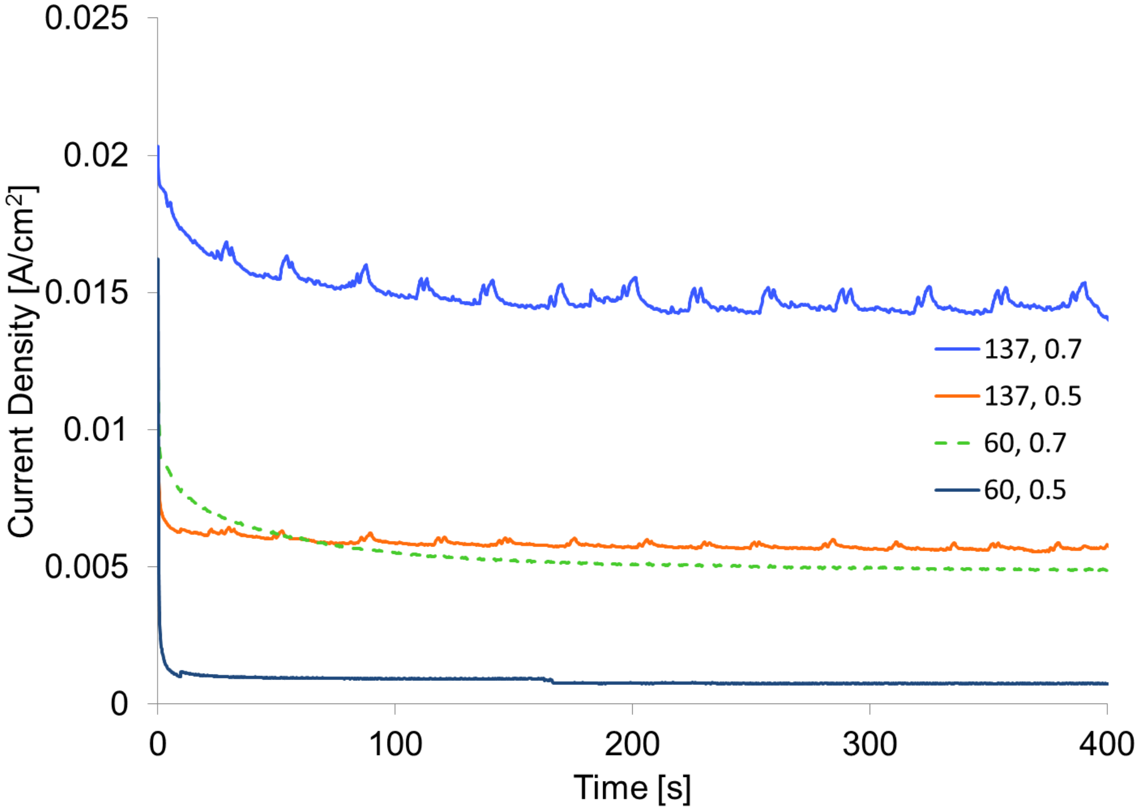

Figure 6.5: Example potentiostatic measurements for steady state current at a given temperature and potential. Measurements were performed for 120 minutes to ensure a steady-state value was measured.

was not calculated due to scatter. In comparison, Behm et. measured apparent activation energies of 50 and 30 kJ mol^{-1}, and CO_2 formation of 78 and 49 kJ mol^{-1} for 0.5 V and 0.7 V respectively [4] over a range of 23-100 °C. The larger apparent activation energy for CO_2 formation compared to total ethylene glycol electrooxidation is due to increasing CO_2 current efficiencies with increasing temperatures. This relationship between CO_2 formation and overall reaction rate has been seen before in ethylene glycol, methanol, and ethanol electrooxidation [4,28,118].

The temperature dependence of turnover frequency calculated for the ECR reaction with ethylene glycol is shown in Figure 6.7. The trend is increasing TOF with increasing temperature. However, at 137 °C at both 0.5 and 0.7 V there is a decrease. We hypothesize that this decrease is related to loss of catalyst due to the Nafion catalyst binder beginning to solubilize. The range of turnover frequency for ECR of ethylene glycol is $6.2\text{x}10^{-4}$-$1.8\text{x}10^{-2}$ sec^{-1}. Dumesic observed turnover frequency of $1.3\text{x}10^{-3}$ sec^{-1} for solutions of one weight percent ethylene glycol at 498 K (225 °C) [2].

The partial and complete oxidation products from the anode side of the ECR reactor were analyzed by GC and HPLC. Seven potential products were analyzed by the HPLC including: oxalic acid, acetic acid, formic acid, formaldehyde, glyoxal, glycolic acid, and glycolaldehyde. Of those possible products glycolic acid, oxalic acid and glycolaldehyde were detected at sufficient levels to quantify. The GC also detected carbon dioxide and hydrogen. The hydrogen detected by the GC at the anode side was either hydrogen left over from traditional aqueous phase reforming on the catalyst without electron transfer or from crossover from the cathode side. Due to the highly variable quantities of hydrogen and the slow rate of APR under these experimental conditions, we believe the hydrogen is from crossover. The mole fraction of products as a function of temperature and potential are shown in Figure 6.8. A ratio of moles of products to moles of ethylene glycol fed are shown in Figure 6.9. The products, overall ethylene glycol conversion, and estimated H_2 formation at the cathode can be seen in Tables 6.2 and 6.3. The products in the tables are listed in values of moles per mole of ethylene glycol reacted, a total reaction of ethylene glycol would yield 2 CO_2 and 5 H_2. The true amount of H_2 generated at the cathode was impossible to determine because hydrogen was supplied to the cathode side to maintain the electrode as a pseudo-reference electrode. The cathode gas stream was tested by GC and only H_2 was present. To estimate the amount of H_2 generated, it is assumed that one H_2 molecule is formed for every two faradaic electrons measured.

The larger CO_2 fraction of the oxidation products is expected, increasing temperature favors more complete oxidation. Interestingly, there was no oxalic acid at 0.5 V, while it was detected at 0.7 V. In addition, more glycolaldehyde was present at 0.5 V while more glycolic acid was present at 0.7 V. Overall, 0.7 V has a larger conversion of ethylene glycol than 0.5 V, Fig. 6.10.

The decrease in CO_2 current efficiency as the potential shifts from 0.5 V to 0.7 V is likely related to a change in rate limiting step. Behm et al. [4] noted that adsorbed CO oxidation is limiting at low potentials due to a limited quantity of adsorbed OH groups. According to Behm et al. [4], at the higher potential more OH is available and the rate limiting step shifts to C-C bond scission. The disappearance of oxalic acid from the 0.7V runs as the temperature increases suggests that the increase in temperature is increasing C-C breakage rates.

The CO_2 electron ratio, moles of CO_2 generated over moles e^- measured, is larger for 0.5V than for 0.7V, Figure 6.10. This is initially counter-intuitive because the reaction at 0.5V is mostly limited by CO oxidation on the catalyst surface, while 0.7V has a catalyst surface with more open sites. However, there are two explanations: (1) The larger rate of glycoaldehyde formation at 0.5V, which only requires 2 electrons (Fig. 6.11), instead of more oxidized products reduces electron consumption by products other than CO_2; (2) a lower probability of adsorption of ethylene glycol and a water molecule on neighboring surface sites due to the large CO coverage at 0.5 V reduces the chance that ethylene glycol will oxidize, instead it will either dissociatively adsorb or desorb.

6.3.3 APR Comparison

One of the main objectives of this research on ECR is to explore its viability compared to APR. There are two ways that ECR can to improve upon APR: catalyst utilization, and undesired side products. To examine catalyst utilization, turnover frequency and required

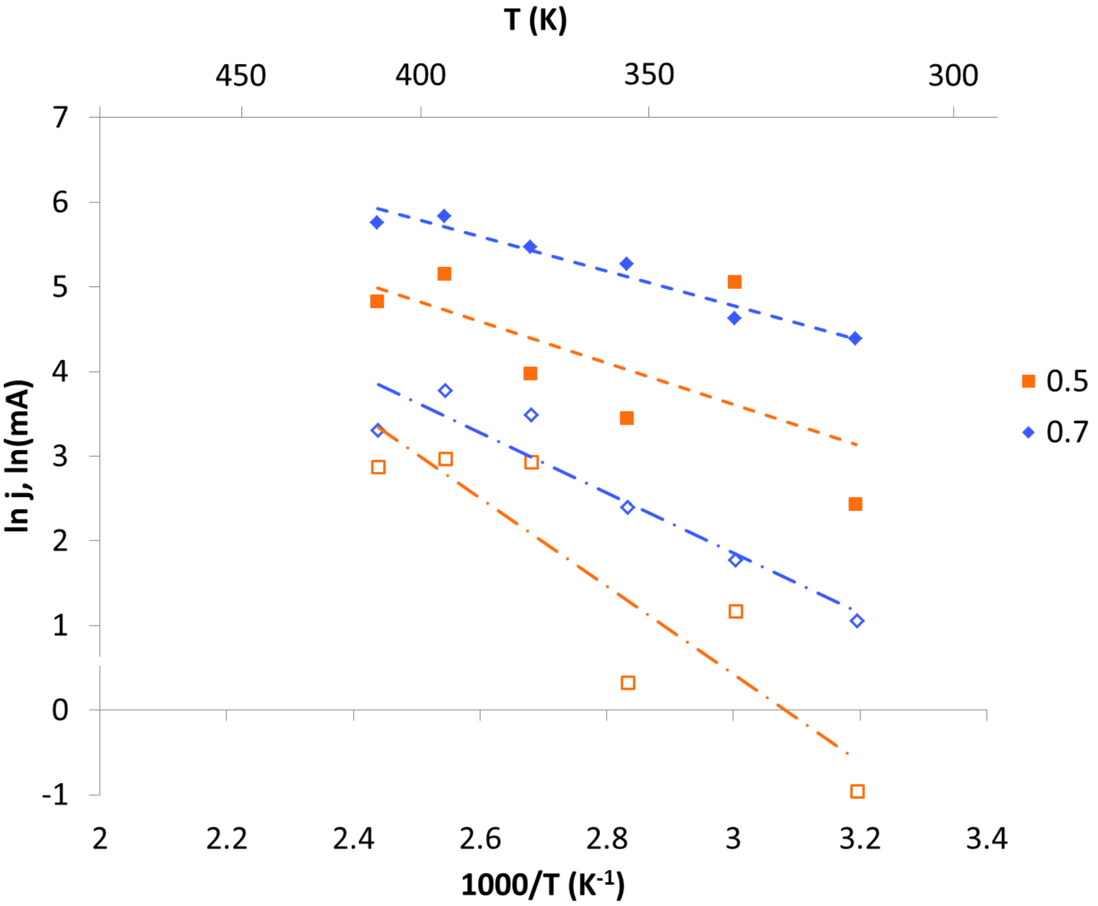

Figure 6.6: Arrhenius plot of apparent activation energy of the faradaic current (filled symbols) and the current efficiency for CO_2 formation (open symbols) for ethylene glycol electrooxidation over the temperature range of 40-137 °C. Two potentials, 0.5 V and 0.7 V are shown. The system is Pt/C catalyst with a Nafion electrolyte 0.1 M ethylene glycol with a flowrate 4.0 mL/min, and 4 mg/cm^2 Pt loading. The pressures for the system were: 207 kpa for temperatures of 40, 60, 80 & 100°C; 241 kpa for 120°C, and 531 kpa for 137°C.

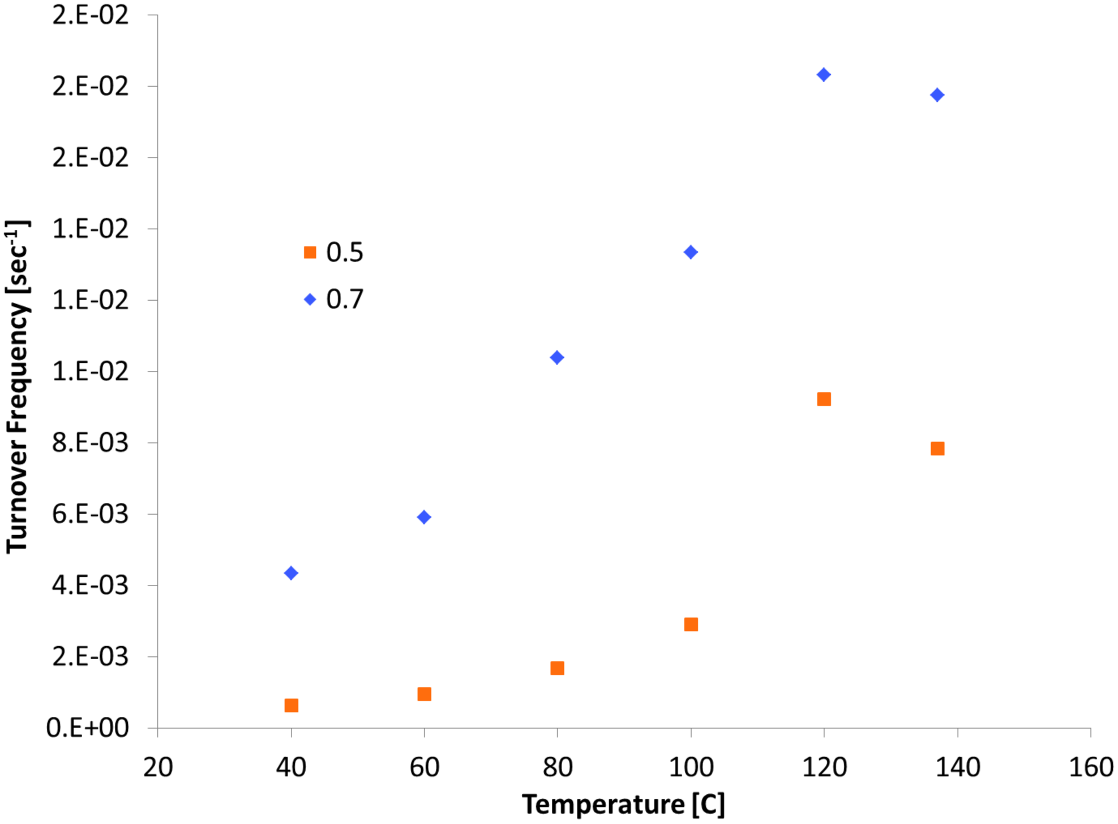

Figure 6.7: The turnover frequency for ethylene glycol ECR as a function of temperature.

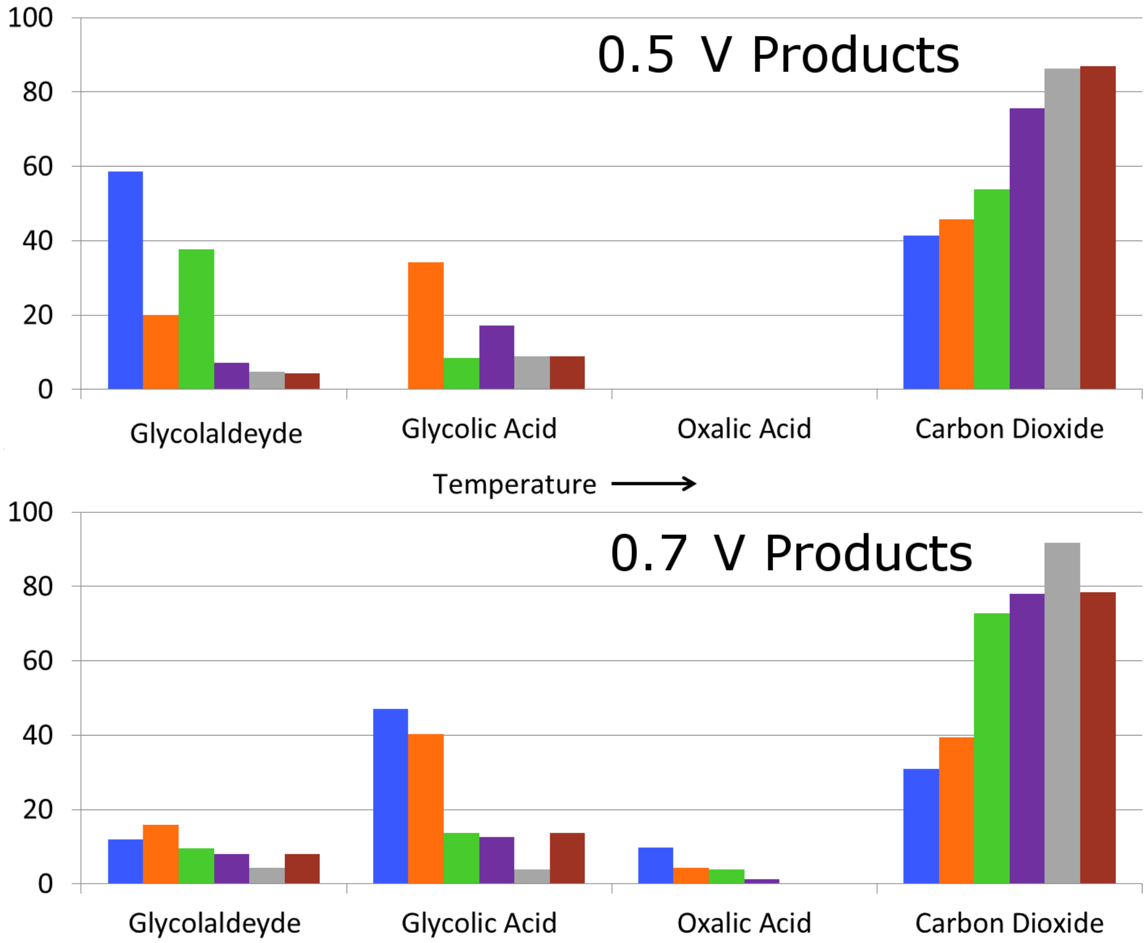

Figure 6.8: Products from ethylene glycol electrooxidation measured by HPLC and GC from potentials of 0.5 V and 0.7 V. Each bar represents a different temperature increasing from right to left in 20 °C intervals, starting at 40 °C. The values are mole percent of products.

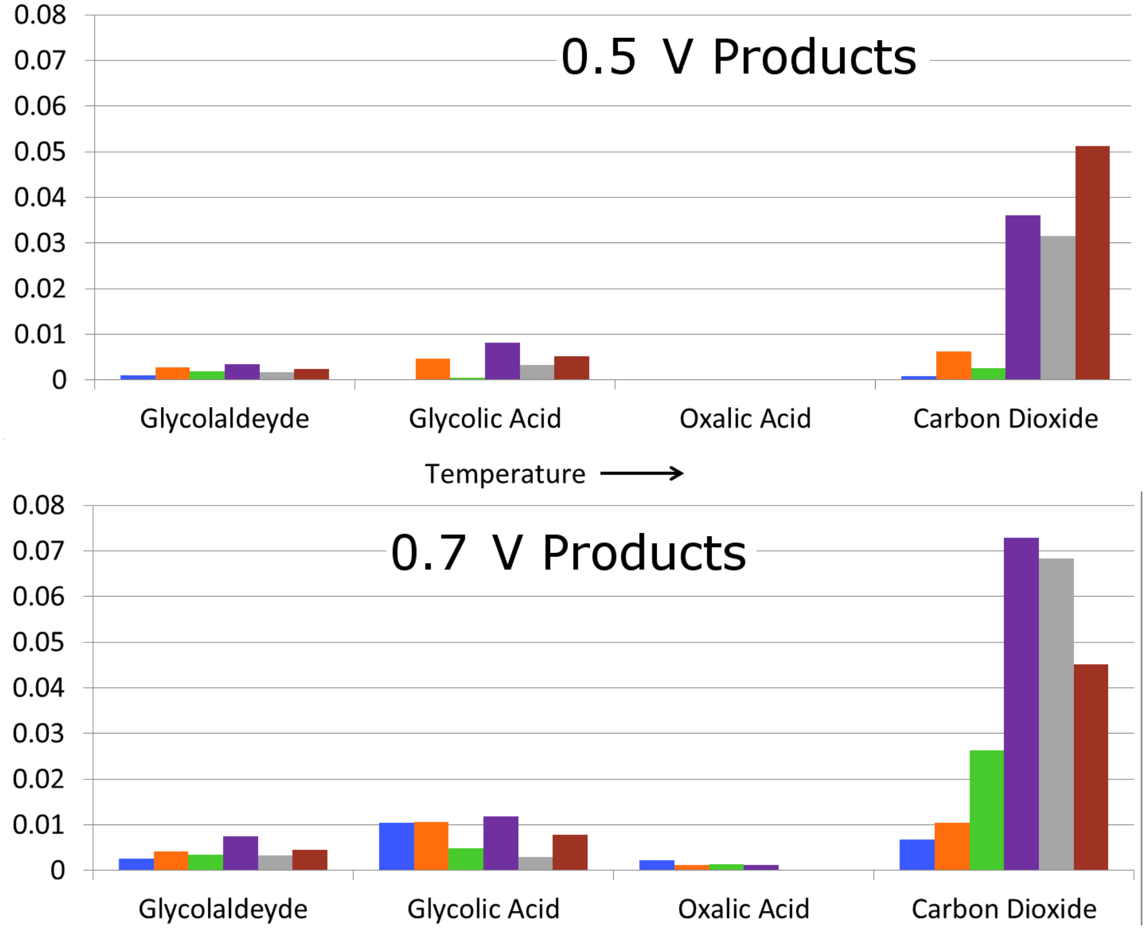

Figure 6.9: Products from ethylene glycol electrooxidation measured by HPLC and GC from potentials of 0.5 V and 0.7 V. Each bar represents a different temperature increasing from right to left in 20 °C intervals, starting at 40 °C. The values are moles of product per mole of ethylene glycol feed.

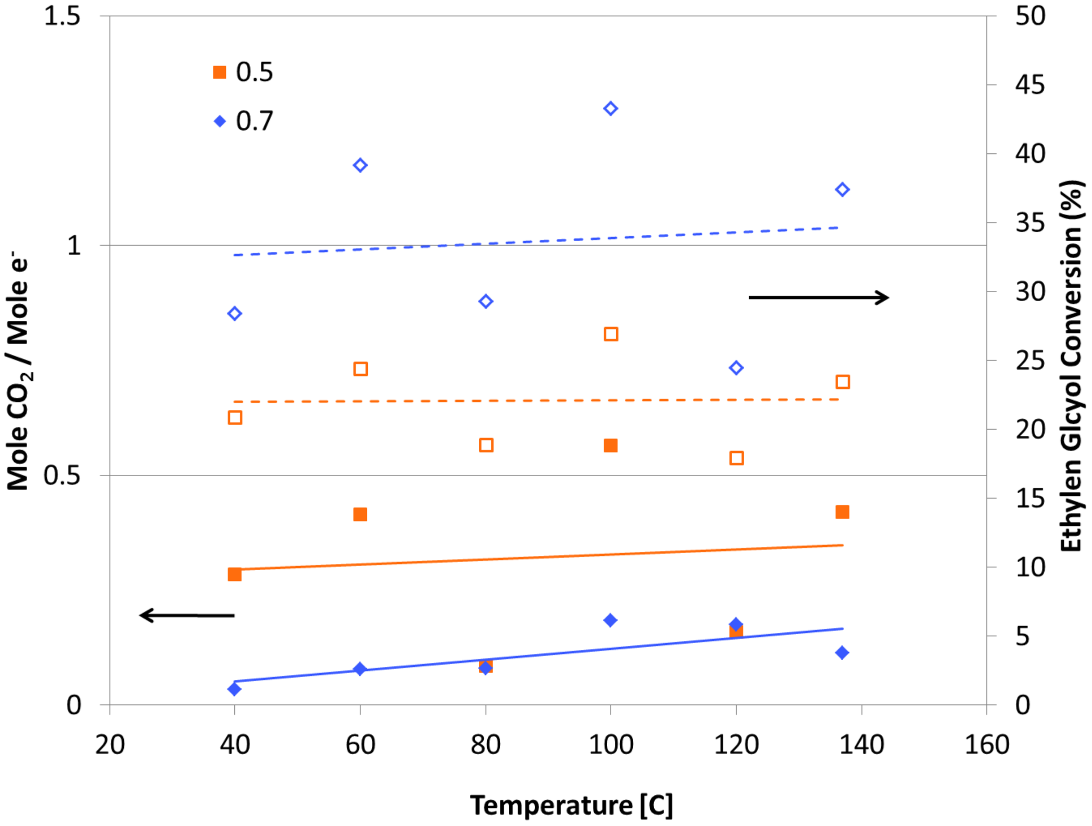

Figure 6.10: The CO_2 current ratio (filled symbols) and percent of ethylene glycol conversion (open symbols) as function of temperature and potential.

Potential, V	0.5					
Temperature, C	40	60	80	100	120	137
Ethylene glycol conversion %	20.8	24.4	18.9	26.9	17.9	23.5
Carbon dioxide	0.15	0.50	0.37	1.14	1.29	1.42
Glycolaldehyde	0.21	0.22	0.25	0.11	0.07	0.07
Glycolic acid	0	0.38	0.06	0.26	0.13	0.15
Oxalic acid	0	0	0	0	0	0
H_2 Anode	0.37	0.41	0.19	0.02	0.08	0.03
Estimated H_2 Cathode	0.27	0.60	2.13	1.01	4.03	1.69

Table 6.2: Products of ethylene glycol electrooxidation at 0.5 V_{RHE}. The products are normalized per mole of ethylene glycol consumed.

Potential, V	0.7					
Temperature, C	40	60	80	100	120	137
Ethylene glycol conversion %	28.4	39.2	29.3	43.3	24.5	37.4
Carbon dioxide	0.31	0.44	0.79	1.82	1.55	1.12
Glycolaldehyde	0.12	0.18	0.10	0.19	0.07	0.11
Glycolic acid	0.47	0.45	0.15	0.30	0.07	0.2
Oxalic acid	0.10	0.05	0.04	0.03	0	0
H_2 Anode	0.02	1.15	0.06	0.01	0.02	0.02
Estimated H_2 Cathode	4.42	2.82	4.93	4.94	4.41	4.96

Table 6.3: Products of ethylene glycol electrooxidation at 0.7 V_{RHE}. The products are normalized per mole of ethylene glycol consumed.

catalyst to react one mole of ethylene glycol per hour were examined. The parameters and calculation of catalyst utilization is shown in Tables 6.4 and 6.5 and equations 6.2, 6.3, and 6.4. A clear advantage in catalyst use for ECR relative to APR seen. Under the conditions calculated, ECR needs about 95% less platinum catalyst than APR. The decrease in platinum requirement for ECR can be explained by improved reaction rate and catalyst utilization visible in the turnover frequency. The increased reaction rate may be related to a decease in CO coverage at operating conditions.

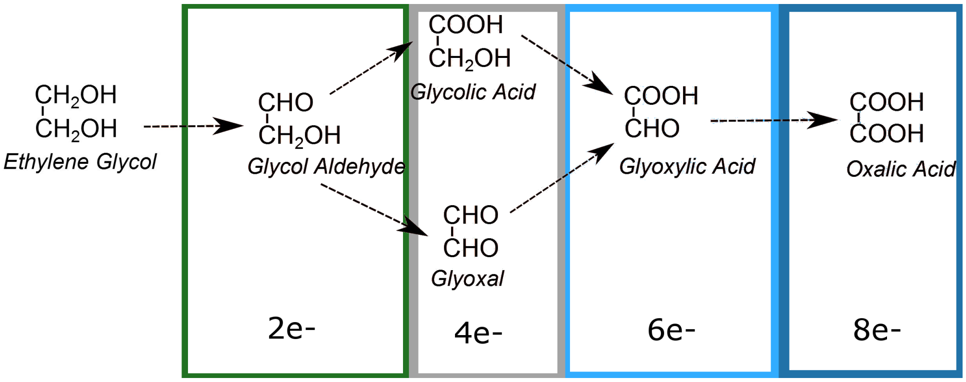

Figure 6.11: The functional group oxidation pathway for ethylene glycol. The total electrons needed to reach each partial oxidation product are listed across the bottom

APR [2]	
Temperature, C	265
Conversion, %	99
WHSV, $g_{fed}\ g_{cat}^{-1}\ hr^{-1}$	0.008
Platinium Loading, wt%	3
TOF, sec^{-1}	$1.33x10^{-3}$
Platinum, g	227

Table 6.4: APR catalyst utilization calculation

$$\frac{1\text{ mole EG react}}{1\text{ hour}}\cdot\frac{1\text{ mole fed}}{0.99\text{ mole react}}\cdot\frac{62.07\text{ g}}{1\text{ mole EG}}\cdot\frac{g_{cat}\cdot\text{hr}}{0.008\ g_{EG}}\cdot\frac{0.03\ g_{Pt}}{1\ g_{cat}}=227\ g_{Pt}\tag{6.2}$$

$$\frac{4\ mg_{pt}}{cm^2}\cdot\frac{25\ cm^2}{1\text{ MEA}}\cdot\frac{\text{min}\cdot\text{MEA}}{4\ mL_{soln}}\cdot\frac{1000\ mL_{soln}}{1\ L_{soln}}\cdot\frac{\text{hr}}{60\text{ min}}\cdot\frac{g_{Pt}}{1000\ mg_{Pt}}=\frac{0.417\text{ hr}\cdot g_{Pt}}{L_{soln}}\tag{6.3}$$

$$\frac{0.417\text{ hr}\cdot g_{Pt}}{L_{soln}}\cdot\frac{L_{soln}}{0.1\text{ mole }EG_{fed}}\cdot\frac{1\text{ mole }EG_{fed}}{0.374\text{ mole }EG_{react}}\cdot\frac{1\text{ mole }EG_{react}}{\text{hr}}=11.1\ g_{Pt}\tag{6.4}$$

Under the previously stated reaction conditions the APR system generated small amounts of methane and ethane from reactions of carbon dioxide and hydrogen [2]. These were not

ECR	
Temperature, C	137
Potential, V	0.7
Conversion, %	37.4
Concentration, M	0.1
Pump Rate, L/min	0.004
Platinum Loading, mg/cm^2	8.0
MEA Area, cm^2	25
TOF, sec^{-1}	1.77x10^{-2}
Platinum, g	11.1

Table 6.5: ECR catalyst utilization calculation

present in the ECR system because of separation of the reactions. This prevention of undesired side products improves the overall hydrogen yield of the reforming reaction.

The two previous comparisons simplify the overall difference between the two processes. The additional voltage of ECR potentially has an energy cost relative to APR. This difference comes out to be about 675 kJ for every mole of ethylene glycol reacted. Which is equivalent to heating 10 kg of water (≈1 mole of ethylene glycol at 0.1M) by a change of 16.2°C. This may not be a penalty, however, because any overpotential will decease the heating load of the system.

6.4 Conclusions

Our conclusions are listed in Below:

1. Potential required to sustain ethylene glycol consumption as a function of temperature.

Increasing temperature shifts the ignition point of ethylene glycol in the cathodic direction. At 40 °C the onset potential was 0.70 V and at 137 °C the onset potential was 0.42 V.

2. The apparent activation energy for the ECR reaction and CO_2 formation.

The apparent activation energy for ethylene glycol electrooxidation is 20 kJ mol^{-1} and 17 kJ mol^{-1} for 0.5V and 0.7V respectively. The apparent activation for CO_2 formation is larger at 43 kJ mol^{-1} at 0.5V and 30 kJ mol^{-1} at 0.7V. The formation of CO_2 increased as the formation of partial oxidation products deceased with increased temperature.

3. A complete mass balance including partial oxidation products.

We have presented a mostly complete mass balance of the ethylene glycol electrooxidation reaction including partial oxidation products. Overall, only 3 of the partial oxidation products are detected, glycolaldehyde, glycolic acid, and oxalic acid. At all temperatures CO_2 is the dominate oxidation product.

4. Can ECR sustain C-C bond breakage and complete utilization of ethylene glycol?

We see an increase in C-C bond scission with increasing temperatures at potentials of 0.7 V. More data are needed to determine if the ECR can sustain them C-C bonds breakage.

5. Will ethylene glycol completely oxidize at temperatures of 130-150 °C and a potential of 0.5 V?

We see complete oxidation products of ethylene glycol at 137°C and 0.7V. We are not completely oxidizing all of the ethylene glycol; there is still some trace amounts of partial oxidation products.

6. How does catalyst utilization of ECR compare with APR?

ECR uses about 68% less platinum than APR, when normalized to one mole of ethylene glycol consumed per hour. For the conditions tested, ECR has low overall conversion, 5.74%, but that was not an optimized parameter.

Chapter 7

SUMMARY AND RECOMMENDATIONS

This study has investigated electro-catalytic reforming of ethylene glycol as a model molecule for carbohydrate reforming. The technique proved difficult, due partially to the high temperature requirement, but possible and promising for conversion of oxygenated hydrocarbons to hydrogen and carbon dioxide.

We set out a series of design criteria to accomplish with the ECR reactor including: high temperature operation, high pressure aqueous phase, sufficient partial oxidation products for analysis, and electrooxidation results that mirrored known literature. Our system was successfully designed to accomplish all of them except for the high temperature electrolyte. We were able to reach a temperature that is greater than any known published ethylene glycol electrooxidation data. The quantification of high temperature partial oxidation products, including glycolic acid, glycolaldehyde, and oxalic acid, was the first to our knowledge. Previous work by Behm et al. quantified CO_2 but now partial oxidation products [4].

There were numerous design issues with the electrolyte. Data gathered with a Nafion membrane had problems with contact resistance. Long term viability of Nafion membranes is questionable because operation at temperatures above 120 °C will eventually break down the Nafion [70]. Experiments with cross-linked sPEEK membranes found a maximum operating temperature that was not sufficient to increase the temperature range of the ECR reactor beyond that of Nafion.

The work with cross-linked sPEEK membranes did not yield a functional high temperature proton conducting membrane. For future investigations, there are two avenues that show the most promise: block co-polymer or inorganic fillers. With increased temperatures the conductivity of polymers become less of a concern, therefore a combination of a stable polymer and a conducting polymer, which normally would reduce the overall conductivity, could allow the system to operate at higher temperatures. The co-polymer would have to be designed with polymer dissolution in mind, a review by Koenig et al. noted that a blend of polymers could dissolve one polymer and leave behind the stable polymer [71]. Recent work with a cross-linked sPEEK membrane with trisilanol phenyl polyhedral oligosilsesquioxane (TSP POSS) filler showed promise of a slight decease water uptake at 100 °C [119].

Removing the membrane from the ECR reactor would have additional benefits. A redesigned system with a liquid electrolyte would allow for easier introduction of a true reference electrode. This would permit complete analysis of the hydrogen product, since there would be no secondary source of hydrogen. In addition, a true reference would help with identifying contaminated electrodes and would prevent unexpected potential shifts.

While the membrane had problems and prevented the inclusion of a reference electrode, removing it causes other issues. Without the separation of hydrogen from the carbon dioxide and other products, methanation and homogeneous hydrogen consumption reactions would reduce the overall hydrogen yield and selectivity. To replace the membrane, a liquid electrolyte with sufficient ions for ionic conductivity is needed, but each option has trade-offs. If replaced with an acid, the acid would hydrolyze the reactants like glucose and lead to a distribution of products including hydroxymethulfurfural (HMF), 1,6-anhydroglucose, levulinic acid, and formic acid, which complicate the chemistry and reduce the hydrogen selectivity [120]. If replaced with a base, the stability of partial oxidation products would change and hydrogen selectivity would decrease [55]. If replaced with a salt, adsorption of salt on the catalyst would lead to decreased catalytic activity.

The experiments with reforming ethylene glycol using a Nafion electrolyte on temperatures up to 137 °C were enlightening. We did not detect any oxalic acid at temperatures above 120 °C. We did not see evidence of any change in electrooxidation mechanism with increased temperature. We affirmed previous work that saw a stronger relationship between carbon dioxide formation and temperature than total reaction rate and temperature.

Future work investigating larger carbohydrates, like glycerol, would be valuable to understanding of conditions that can break carbon-carbon bonds. Aqueous phase reforming saw a decrease in hydrogen selectivity when increasing carbon chain length from two to three [2]. Long term future work looking at reforming products from actual biomass would be an exciting way to test the real world applicability of this technology.

A summary of our conclusions and future work can be seen in below.

Conclusions

1. Increasing temperature shifts the ignition point of ethylene glycol in the cathodic direction.

2. The ethylene glycol reaction rate and CO_2 current efficiency increase with increasing temperature with no evidence of a mechanism change. We observed complete oxidation of ethylene glycol at 130 °C and 0.5 V as predicted by Behm et al. [4] but did not oxidize all of the ethylene glycol.

3. The electrooxidaiton of ethylene glycol gives 5 main products which vary in concentration depending on the reaction conditions. These products are: carbon dioxide, hydrogen, glycolaldehyde, glycolic acid, and oxalic acid. At a potential of 0.5 V no oxalic acid was formed.

4. We saw an increase in C-C bond scission with increasing temperatures at potentials of 0.7 V. More data are needed to determine if ECR can sustain C-C bonds breakage.

5. ECR uses about 36% less platinum than APR, when normalized to an equivalent amount of ethylene glycol consumed per hour.

Future Work

1. Investigation of glycerol or larger carbohydrates would be helpful in understanding the C-C bond breakage capability of ECR.

2. Incorporation of acid hydrolysis products from biomass understand the complications of real life reactants.

BIBLIOGRAPHY

[1] G. W. Huber, J. Shabaker, S. Evans, and J. a. Dumesic, "Aqueous-phase reforming of ethylene glycol over supported Pt and Pd bimetallic catalysts," *Applied Catalysis B: Environmental*, vol. 62, pp. 226–235, Feb. 2006.

[2] R. D. Cortright, R. R. Davda, and J. a. Dumesic, "Hydrogen from catalytic reforming of biomass-derived hydrocarbons in liquid water.," *Nature*, vol. 418, pp. 964–7, Aug. 2002.

[3] H. Wang, Z. Jusys, and R. Behm, "Adsorption and electrooxidation of ethylene glycol and its C2 oxidation products on a carbon-supported Pt catalyst: A quantitative DEMS study," *Electrochimica Acta*, vol. 54, pp. 6484–6498, Nov. 2009.

[4] M. Chojak Halseid, Z. Jusys, and R. Behm, "Electrooxidation of ethylene glycol on a carbon-supported Pt catalyst at elevated temperatures and pressure: A high-temperature/high-pressure DEMS study," *Journal of Electroanalytical Chemistry*, vol. 644, pp. 103–109, June 2010.

[5] "International Energy Outlook 2010," 2010.

[6] G. Magdalena, S. Joshi, and H. L. MacLean, "A review of u.s. and canadian biomass supply studies," *Bioresources*, vol. 4, no. 1, pp. 341–369, 2009.

[7] J. Hughesturnbull and P. Ah, "Developing an integrated approach to biomass energy systems in the united states," *Biomass and Bioenergy*, vol. 6, no. 1-2, pp. 151–158, 1994.

[8] G. Morris, "The Value of the Benefits of The Value of the Benefits of U. S. Biomass Power," Tech. Rep. November, Green Power Institute, Berkeley, California, 1999.

[9] S. Kumarappan, S. Joshi, and H. MacLean, “Biomass Supply for Biofuel Production: Estimates for the United States and Canada,” *BioResources*, vol. 4, no. 3, pp. 1070–1087, 2009.

[10] J. M. Ogden, “Prospects for Building a Hydrogen Energy Infrastructure,” *Annual Review of Energy and the Environment*, vol. 24, pp. 277–279, 1999.

[11] J. J. Alves and G. P. Towler, “Analysis of Refinery Hydrogen Distribution Systems,” *Industrial & Engineering Chemistry Research*, vol. 41, pp. 5759–5769, Nov. 2002.

[12] Z. Qi, Q. Zhang, J. Chang, T. Wang, and Y. Xu, “Review of biomass pyrolysis oil properties and upgrading research,” *Energy Conversion and Management*, vol. 48, pp. 87–92, Jan. 2007.

[13] “Regulation of Fuels and Fuel Additives: Changes to Renewable Fuel Standard Program,” tech. rep., Environmental Protection Agency, Washington D.C., 2010.

[14] F. Mahfud, F. Ghijsen, and H. Heeres, “Hydrogenation of fast pyrolyis oil and model compounds in a two-phase aqueous organic system using homogeneous ruthenium catalysts,” *Journal of Molecular Catalysis A: Chemical*, vol. 264, pp. 227–236, Mar. 2007.

[15] J. Shabaker, G. W. Huber, R. Davda, R. Cortright, and J. a. Dumesic, “Aqueous-phase reforming of ethylene glycol over supported platinum catalysts,” *Catalysis Letters*, vol. 88, no. May, pp. 1–8, 2003.

[16] J. Shabaker, R. Davda, G. W. Huber, R. Cortright, and J. a. Dumesic, “Aqueous-phase reforming of methanol and ethylene glycol over alumina-supported platinum catalysts,” *Journal of Catalysis*, vol. 215, pp. 344–352, Apr. 2003.

[17] G. Huber, R. Cortright, and J. a. Dumesic, “Renewable alkanes by aqueous-phase reforming of biomass-derived oxygenates.,” *Angewandte Chemie (International ed. in English)*, vol. 43, pp. 1549–51, Mar. 2004.

[18] R. R. Davda, J. J. Shabaker, G. G. Huber, R. R. Cortright, and J. a. J. Dumesic, "A review of catalytic issues and process conditions for renewable hydrogen and alkanes by aqueous-phase reforming of oxygenated hydrocarbons over supported metal catalysts," *Applied Catalysis B: Environmental*, vol. 56, pp. 171–186, Mar. 2005.

[19] J. R. Salge, B. J. Dreyer, P. J. Dauenhauer, and L. D. Schmidt, "Renewable hydrogen from nonvolatile fuels by reactive flash volatilization.," *Science (New York, N.Y.)*, vol. 314, pp. 801–4, Nov. 2006.

[20] J. Shabaker, G. W. Huber, and J. a. Dumesic, "Aqueous-phase reforming of oxygenated hydrocarbons over Sn-modified Ni catalysts," *Journal of Catalysis*, vol. 222, pp. 180–191, Feb. 2004.

[21] J. Shabaker, D. Simonetti, R. Cortright, and J. a. Dumesic, "Sn-modified Ni catalysts for aqueous-phase reforming: Characterization and deactivation studies," *Journal of Catalysis*, vol. 231, pp. 67–76, Apr. 2005.

[22] J. Shabaker and J. a. Dumesic, "Kinetics of aqueous-phase reforming of oxygenated hydrocarbons: Pt/Al2O3 and Sn-Modified Ni catalysts," *Ind. Eng. Chem. Res*, vol. 43, no. 12, pp. 3105–3112, 2004.

[23] S. Sriramulu, T. Jarvi, and E. Stuve, "A kinetic analysis of distinct reaction pathways in methanol electrocatalysis on Pt(111)," *Electrochimica Acta*, vol. 44, pp. 1127–1134, Nov. 1998.

[24] R. de Lima, V. Paganin, T. Iwasita, and W. Vielstich, "On the electrocatalysis of ethylene glycol oxidation," *Electrochimica Acta*, vol. 49, pp. 85–91, Dec. 2003.

[25] N. Marković, M. Avramov-Ivić, N. Marinković, and R. Adžić, "Structural effects in electrocatalysisEthylene glycol oxidation on platinum single-crystal surfaces," *Journal of Electroanalytical Chemistry and Interfacial Electrochemistry*, vol. 312, pp. 115–130, Aug. 1991.

[26] H. Dinh, "Electrocatalysis in direct methanol fuel cells: in-situ probing of PtRu anode catalyst surfaces," *Journal of Electroanalytical Chemistry*, vol. 491, pp. 222–233, Sept. 2000.

[27] R. G. C. S. Reis, C. a. Martins, and G. a. Camara, "The Electrooxidation of 2-Propanol: An Example of an Alternative Way to Look at In Situ FTIR Data," *Electrocatalysis*, vol. 1, pp. 116–121, June 2010.

[28] H. Wang, Z. Jusys, and R. J. Behm, "Ethanol Electrooxidation on a Carbon-Supported Pt Catalyst: Reaction Kinetics and Product Yields," *The Journal of Physical Chemistry B*, vol. 108, pp. 19413–19424, Dec. 2004.

[29] Z. Jusys, J. Kaiser, and R. J. Behm, "Methanol Electrooxidation over Pt/C Fuel Cell Catalysts: Dependence of Product Yields on Catalyst Loading," *Langmuir*, vol. 19, pp. 6759–6769, Aug. 2003.

[30] S. Song, W. Zhou, Z. Zhou, L. Jiang, G. Sun, Q. Xin, V. Leontidis, S. Kontou, and P. Tsiakaras, "Direct ethanol PEM fuel cells: The case of platinum based anodes," *International Journal of Hydrogen Energy*, vol. 30, pp. 995–1001, Aug. 2005.

[31] H.-F. Wang and Z.-P. Liu, "Comprehensive mechanism and structure-sensitivity of ethanol oxidation on platinum: new transition-state searching method for resolving the complex reaction network.," *Journal of the American Chemical Society*, vol. 130, pp. 10996–1004, Aug. 2008.

[32] A. Kowal, M. Li, M. Shao, K. Sasaki, M. B. Vukmirovic, J. Zhang, N. S. Marinkovic, P. Liu, A. I. Frenkel, R. R. Adzic, and R. Adžić, "Ternary Pt/Rh/SnO2 electrocatalysts for oxidizing ethanol to CO2.," *Nature materials*, vol. 8, pp. 325–30, Apr. 2009.

[33] H. Nonaka and Y. Matsumura, "Electrochemical oxidation of carbon monoxide, methanol, formic acid, ethanol, and acetic acid on a platinum electrode under hot

aqueous conditions," *Journal of Electroanalytical Chemistry*, vol. 520, pp. 101–110, Feb. 2002.

[34] C. Lamy, "Electrocatalytic oxidation of organic compounds on noble metals in aqueous solution," *Electrochimica Acta*, vol. 29, no. 11, pp. 1581–1588, 1984.

[35] T. Kawaguchi, "Temperature dependence of the oxidation of carbon monoxide on carbon supported Pt, Ru, and PtRu," *Electrochemistry Communications*, vol. 6, pp. 480–483, May 2004.

[36] E. Peled, V. Livshits, and T. Duvdevani, "High-power direct ethylene glycol fuel cell (DEGFC) based on nanoporous proton-conducting membrane (NP-PCM)," *Journal of Power Sources*, vol. 106, pp. 245–248, Apr. 2002.

[37] F. A. Carey, *Chapter 17: Aldehydes and Ketones. Nucleophilic Addition to C=O*. McGraw Hill, 4th ed., 2000.

[38] P. Dauenhauer, J. Salge, and L. Schmidt, "Renewable hydrogen by autothermal steam reforming of volatile carbohydrates," *Journal of Catalysis*, vol. 244, pp. 238–247, Dec. 2006.

[39] R. D. Cortright, R. R. Davda, and J. A. Dumesic, "Hydrogen from catalytic reforming of biomass-derived hydrocarbons in liquid water," *Nature*, vol. 418, no. 6901, p. 964, 2002.

[40] G. Huber and J. a. Dumesic, "An overview of aqueous-phase catalytic processes for production of hydrogen and alkanes in a biorefinery," *Catalysis Today*, vol. 111, pp. 119–132, Jan. 2006.

[41] R. R. Davda, J. J. Shabaker, G. W. Huber, R. R. Cortright, and J. a. J. Dumesic, "Aqueous-phase reforming of ethylene glycol on silica-supported metal catalysts," *Applied Catalysis B: Environmental*, vol. 43, pp. 13–26, June 2003.

[42] R. R. R. R. Davda and J. a. Dumesic, “Catalytic reforming of oxygenated hydrocarbons for hydrogen with low levels of carbon monoxide.,” *Angewandte Chemie (International ed. in English)*, vol. 42, pp. 4068–71, Sept. 2003.

[43] R. R. Davda and J. A. Dumesic, “Renewable hydrogen by aqueous-phase reforming of glucose.,” *Chemical Communications*, pp. 36–7, Jan. 2004.

[44] G. W. Huber, J. J. N. Chheda, C. J. C. Barrett, and J. a. Dumesic, “Production of liquid alkanes by aqueous-phase processing of biomass-derived carbohydrates.,” *Science (New York, N.Y.)*, vol. 308, pp. 1446–50, June 2005.

[45] G. W. G. Huber, S. Iborra, and A. Corma, “Synthesis of transportation fuels from biomass: chemistry, catalysts, and engineering.,” *Chemical reviews*, vol. 106, pp. 4044–98, Sept. 2006.

[46] H. Wang, Z. Jusys, and R. Behm, “Electrochemical oxidation kinetics and mechanism of ethylene glycol on a carbon supported Pt catalyst: A quantitative DEMS study,” *Journal of Electroanalytical Chemistry*, vol. 595, pp. 23–36, Sept. 2006.

[47] B. Beden, C. Lamy, A. Bewick, and K. Kunimatsu, “Electrosorption of methanol on a platinum electrode. IR spectroscopic evidence for adsorbed CO species,” *Journal of Electroanalytical Chemistry*, vol. 121, pp. 343–347, Nov. 1981.

[48] B. Beden, A. Bewick, K. Kunimatsu, and C. Lamy, “Infrared study of adsorbed species on electrodes: Adsorption of carbon monoxide on Pt, Rh and Au,” *Journal of Electroanalytical Chemistry*, vol. 142, no. 1-2, pp. 345–356, 1982.

[49] C. Yang, S. Srinivasan, A. B. Bocarsly, S. Tulyani, and J. B. Benziger, “A comparison of physical properties and fuel cell performance of Nafion and zirconium phosphate/Nafion composite membranes,” *Journal of Membrane Science*, vol. 237, pp. 145–161, July 2004.

[50] K. T. Adjemian, S. Lee, S. Srinivasan, J. B. Benziger, and A. B. Bocarsly, “Silicon oxide Nafion composite membranes for proton-exchange membrane fuel cell operation at 80-140 C,” *Journal of the Electrochemical Society*, vol. 149, no. 3, p. A256, 2002.

[51] G. Alberti, M. Casciola, L. Massinelli, and B. Bauer, “Polymeric proton conducting membranes for medium temperature fuel cells (110-160C),” *Journal of Membrane Science*, vol. 185, pp. 73–81, Apr. 2001.

[52] C. Yang, P. Costamagna, S. Srinivasan, J. B. Benziger, and A. B. Bocarsly, “Approaches and technical challenges to high temperature operation of proton exchange membrane fuel cells,” *Journal of Power Sources*, vol. 103, no. 1, pp. 1–9, 2001.

[53] K. T. Adjemian, R. Dominey, L. Krishnan, H. Ota, P. Majsztrik, T. Zhang, J. Mann, B. Kirby, L. Gatto, M. Velo-Simpson, J. Leahy, S. Srinivasan, J. B. Benziger, and A. B. Bocarsly, “Function and Characterization of Metal OxideNafion Composite Membranes for Elevated-Temperature H2/O2 PEM Fuel Cells,” *Chemistry of Materials*, vol. 18, pp. 2238–2248, May 2006.

[54] H. Ewe, E. Justi, and M. Pesditschek, “Ethylene glycol as fuel for alkaline fuel cells,” *Energy Conversion*, vol. 15, no. 1-2, pp. 9–14, 1975.

[55] W. Hauffe and J. Heitbaum, “The electrooxidation of ethylene glycol at platinum in potassium hydroxide,” *Electrochimica Acta*, vol. 23, no. 4, pp. 299–304, 1978.

[56] P. Christensen and A. Hamnett, “The oxidation of ethylene glycol at a platinum electrode in acid and baseAn in situ FTIR study,” *Journal of Electroanalytical Chemistry*, vol. 260, pp. 347–359, Mar. 1989.

[57] F. Hahn, B. Beden, F. Kadirgan, and C. Lamy, “Electrocatalytic oxidation of ethylene glycol:: Part III. In-situ infrared reflectance spectroscopic study of the strongly bound species resulting from its chemisorption at a platinum electrode in aqueous medium,” *Journal of Electroanalytical Chemistry*, vol. 216, no. 1-2, pp. 169–180, 1987.

[58] F. Kadirgan, B. Beden, and C. Lamy, “Electrocatalytic oxidation of ethylene-glycol:: Part I. Behaviour of platinum ad-atom electrodes in acid medium,” *Journal of Electroanalytical Chemistry*, vol. 136, no. 1, pp. 119–138, 1982.

[59] G. Horanyi, V. E. Kazarinov, Y. B. Vassiliev, and V. N. Andreev, “Electrochemical and Adsortption Behaviour of Ethylene Glycol and Its Oxidative Derivatives at Platinum Electrodes Part II: Electrocatalytic Transformations Under Steady-State Experimental Conditions at a Platinized Platinum Electrode in Acid Medium,” *Journal of Electroanalytical Chemistry*, vol. 147, pp. 263–278, 1983.

[60] A. K. Vijh, “Anodic Oxidation of Ethylene Glycol on Platinum: a Mechanistic Study,” *Canadian Journal of Chemistry*, vol. 49, pp. 78–88, 1971.

[61] B. Wieland, J. P. Lancaster, C. S. Hoaglund, P. Holota, and W. J. Tornquist, “Electrochemical and Infrared Spectroscopic Quantitative Determination of the Platinum-Catalyzed Ethylene Glycol Oxidation Mechanism at CO Adsorption Potentials,” *Langmuir*, vol. 12, pp. 2594–2601, Jan. 1996.

[62] A. Dailey, J. Shin, and C. Korzeniewski, “Ethylene glycol electrochemical oxidation at platinum probed by ion chromatography and infrared spectroscopy,” *Electrochimica Acta*, vol. 44, pp. 1147–1152, Nov. 1998.

[63] O. Cherstiouk, E. Savinova, L. L. Kozhanova, and V. V. Parmon, “Electrocatalytic oxidation of ethylene glycol on dispersed Pt: Determination of the reaction products,” *Reaction Kinetics and Catalysis Letters*, vol. 69, no. 2, pp. 331–338, 2000.

[64] A. K. Vijh, “Anodic Oxidation of Ethylene Glycol on Platinum: a Mechanistic Study,” *Canadian Journal of Chemistry*, vol. 49, no. 1, pp. 78–88, 1971.

[65] Z. Jusys and R. J. Behm, “DEMS Analysis of Small Organic Molecule Electrooxidation: A High-Temperature High-Pressure DEMS study,” *ECS Transactions*, vol. 16, no. 2, pp. 1243–1251, 2008.

[66] E. Belgsir, E. Bouhier, H. Essis Yei, K. Kokoh, B. Beden, H. Huser, J. Leger, and C. Lamy, "Electrosynthesis in aqueous medium: a kinetic study of the electrocatalytic oxidation of oxygenated organic molecules," *Electrochimica acta*, vol. 36, no. 7, pp. 1157–1164, 1991.

[67] F. Kadirgan, E. Bouhier-Charbonnier, C. Lamy, J. Leger, and B. Beden, "Mechanistic study of the electrooxidation of ethylene glycol on gold and adatom-modified gold electrodes in alkaline medium," *Journal of Electroanalytical Chemistry*, vol. 286, pp. 41–61, 1990.

[68] H. Wang, Y. Zhao, Z. Jusys, and R. Behm, "Ethylene glycol electrooxidation on carbon supported Pt, PtRu and Pt3Sn catalystsA comparative DEMS study," *Journal of Power Sources*, vol. 155, pp. 33–46, Apr. 2006.

[69] K. A. Spies and E. M. Stuve, "Hydrogen Generation by Electrocatalytic Reforming of Ethylene Glycol on a Platinum Electrode," *ECS Transactions*, vol. 35, no. 28, pp. p 31–35, 2011.

[70] M. Casciola, G. Alberti, M. Sganappa, and R. Narducci, "On the decay of Nafion proton conductivity at high temperature and relative humidity," *Journal of Power Sources*, vol. 162, pp. 141–145, Nov. 2006.

[71] B. a. Miller-Chou and J. L. Koenig, "A review of polymer dissolution," *Progress in Polymer Science*, vol. 28, pp. 1223–1270, Aug. 2003.

[72] O. Pekcan, M. Canpolat, and D. Kaya, "In situ fluorescence experiments for real-time monitoring of annealed highT latex film dissolution," *Journal of Applied Polymer Science*, vol. 60, pp. 2105–2112, June 1996.

[73] J. Wainright, J.-t. Wang, and D. Weng, "Acid-Doped Polybenzimidazoles: A New Polymer Electrolyte," *Journal of the*, vol. 142, no. 7, pp. 121–123, 1995.

[74] B. Bauer, D. Jones, and J. Roziere, "Electrochemical characterisation of sulfonated polyetherketone membranes," *Journal of New Materials for Electrochemical Systems*, vol. 3, pp. 93–98, 2000.

[75] Y.-L. Ma, J. S. Wainright, M. H. Litt, and R. F. Savinell, "Conductivity of PBI Membranes for High-Temperature Polymer Electrolyte Fuel Cells," *Journal of The Electrochemical Society*, vol. 151, no. 1, p. A8, 2004.

[76] H. Lin, C. Zhao, Z. Cui, W. Ma, T. Fu, H. Na, and W. Xing, "Novel sulfonated poly(arylene ether ketone) copolymers bearing carboxylic or benzimidazole pendant groups for proton exchange membranes," *Journal of Power Sources*, vol. 193, pp. 507–514, Sept. 2009.

[77] Q. Li, J. O. Jensen, R. F. Savinell, and N. J. Bjerrum, "High temperature proton exchange membranes based on polybenzimidazoles for fuel cells," *Progress in Polymer Science*, vol. 34, pp. 449–477, May 2009.

[78] J. a. Kerres, "Development of ionomer membranes for fuel cells," *Journal of Membrane Science*, vol. 185, pp. 3–27, Apr. 2001.

[79] R. Y. M. Huang, P. Shao, C. M. Burns, and X. Feng, "Sulfonation of poly(ether ether ketone)(PEEK): Kinetic study and characterization," *Journal of Applied Polymer Science*, vol. 82, pp. 2651–2660, Dec. 2001.

[80] K. Do and D. Kim, "Comparison of homogeneously and heterogeneously sulfonated polyetheretherketone membranes in preparation, properties and cell performance," *Journal of Power Sources*, vol. 185, pp. 63–69, Oct. 2008.

[81] X. Jin, M. Bishop, T. Ellis, and F. Karasz, "A sulfonated poly (aryl ether ether ketone)," *British Polymer Journal*, vol. 17, no. 1, pp. 4–10, 1985.

[82] S. L. Rhoden, C. a. Linkous, N. Mohajeri, D. J. Díaz, P. Brooker, D. K. Slattery, and J. M. Fenton, "Low equivalent weight Friedel-Crafts cross-linked sulfonated

poly(ether ether ketone)," *Journal of Membrane Science*, vol. 376, pp. 290–301, July 2011.

[83] K. D. Kreuer, "On the development of proton conducting polymer membranes for hydrogen and methanol fuel cells," *Journal of Membrane Science*, vol. 185, pp. 29–39, 2001.

[84] K.-D. D. Kreuer, "On the development of proton conducting materials for technological applications," *Solid State Ionics*, vol. 97, no. 1, pp. 1–15, 1997.

[85] H. Corti, F. Norespondal, and M. Pilarbuera, "Low temperature thermal properties of Nafion 117 membranes in water and methanol-water mixtures," *Journal of Power Sources*, vol. 161, pp. 799–805, Oct. 2006.

[86] A. Reyna-Valencia, S. Kaliaguine, and M. Bousmina, "Tensile mechanical properties of sulfonated poly(ether ether ketone) (SPEEK) and BPO4/SPEEK membranes," *Journal of Applied Polymer Science*, vol. 98, pp. 2380–2393, Dec. 2005.

[87] J. Yu, M. Pan, and R. Yuan, "Nafion/Silicon oxide composite membrane for high temperature proton exchange membrane fuel cell," *Journal of Wuhan University of Technology-Mater. Sci. Ed.*, vol. 22, pp. 478–481, Sept. 2007.

[88] M. Di Vona, S. Licoccia, and P. Knauth, "Organicinorganic hybrid membranes based on sulfonated polyaryletherketones: Correlation between water uptake and electrical conductivity," *Solid State Ionics*, vol. 179, pp. 1161–1165, Sept. 2008.

[89] F. Helmer-Metzmann, F. Osan, and A. Schneller, "Polymer electrolyte membrane, and process for the production thereof," 2001.

[90] S. D. Mikhailenko, K. Wang, S. Kaliaguine, P. Xing, G. P. Robertson, and M. D. Guiver, "Proton conducting membranes based on cross-linked sulfonated poly(ether ether ketone) (SPEEK)," *Journal of Membrane Science*, vol. 233, pp. 93–99, Apr. 2004.

[91] M. Bandini, A. Melloni, and A. Umani-Ronchi, “New catalytic approaches in the stereoselective Friedel-Crafts alkylation reaction.,” *Angewandte Chemie (International ed. in English)*, vol. 43, pp. 550–6, Feb. 2004.

[92] J. Wang, J. Du, H. Yao, and C. a. Wilkie, “XPS characterization of Friedel-Crafts cross-linked polystyrene,” *Polymer Degradation and Stability*, vol. 74, pp. 321–326, Jan. 2001.

[93] J. Zhu and M. McKinney, “Stabilization of polystyrene by Friedel-Crafts chemistry: effect of position of alcohol and the catalyst,” *Polymer degradation and stability*, vol. 66, pp. 213–220, 1999.

[94] M.-S. Jun, Y.-W. Choi, and J.-D. Kim, “Solvent casting effects of sulfonated poly(ether ether ketone) for Polymer electrolyte membrane fuel cell,” *Journal of Membrane Science*, vol. 396, pp. 32–37, Apr. 2012.

[95] G. P. Robertson, S. D. Mikhailenko, K. Wang, P. Xing, M. D. Guiver, and S. Kaliaguine, “Casting solvent interactions with sulfonated poly(ether ether ketone) during proton exchange membrane fabrication,” *Journal of Membrane Science*, vol. 219, pp. 113–121, July 2003.

[96] S. Kaliaguine, S. D. Mikhailenko, K. P. Wang, P. Xing, G. Robertson, and M. Guiver, “Properties of SPEEK based PEMs for fuel cell application,” vol. 82, pp. 213–222, 2003.

[97] S. D. Mikhailenko, G. P. Robertson, M. D. Guiver, and S. Kaliaguine, “Properties of PEMs based on cross-linked sulfonated poly(ether ether ketone),” *Journal of Membrane Science*, vol. 285, pp. 306–316, Nov. 2006.

[98] R. Guan, H. Dai, C. Li, J. Liu, and J. Xu, “Effect of casting solvent on the morphology and performance of sulfonated polyethersulfone membranes,” vol. 277, pp. 148–156, 2006.

[99] K. Do and D. Kim, “Synthesis and Characterization of Homogeneously Sulfonated Poly(ether ether ketone) Membranes : Effect of Casting Solvent,” *Journal of Applied Polymer Science*, vol. 110, no. 3, pp. 1763–1770, 2008.

[100] P. Rieke, “Personal Interview,” 2011.

[101] S. Ma, A. Kuse, and Z. Siroma, “Measuring Conductivity of Proton Conductive Membrane in the Direction of Thickness,” *Espec Technology Report No*, vol. 1, pp. 12–20, 2006.

[102] J. Peron, D. Edwards, A. Besson, Z. Shi, and S. Holdcroft, “Microstructure Performance Relationships of sPEEK-Based Catalyst Layers,” *Journal of The Electrochemical Society*, vol. 157, no. 8, p. B1230, 2010.

[103] H. Wang, Z. Jusys, and R. J. Behm, “Adsorption and electrooxidation of ethylene glycol and its C2 oxidation products on a carbon-supported Pt catalyst: A quantitative DEMS study,” *Electrochimica Acta*, vol. 54, pp. 6484–6498, Nov. 2009.

[104] J. F. E. Gootzen, W. Visscher, and J. a. R. van Veen, “Characterization of Ethanol and 1,2-Ethanediol Adsorbates on Platinized Platinum with Fourier Transform Infrared Spectroscopy and Differential Electrochemical Mass Spectrometry,” *Langmuir*, vol. 12, pp. 5076–5082, Jan. 1996.

[105] E. Herrero, B. Álvarez, J. M. Feliu, S. Blais, Z. Radovic-Hrapovic, and G. Jerkiewicz, “Temperature dependence of the COads oxidation process on Pt(111), Pt(100), and Pt(110) electrodes,” *Journal of Electroanalytical Chemistry*, vol. 567, pp. 139–149, June 2004.

[106] Y.-J. Fan, Z.-Y. Zhou, C.-H. Zhen, C.-J. Fan, and S.-G. Sun, “Kinetics of dissociative adsorption of ethylene glycol on Pt(1 0 0) electrode surface in sulfuric acid solutions,” *Electrochimica Acta*, vol. 49, pp. 4659–4666, Oct. 2004.

[107] R. Jiang, H. R. Kunz, and J. M. Fenton, "Investigation of membrane property and fuel cell behavior with sulfonated poly(ether ether ketone) electrolyte: Temperature and relative humidity effects," *Journal of Power Sources*, vol. 150, pp. 120–128, Oct. 2005.

[108] W. Zhang, V. Gogel, K. A. Friedrich, and J. Kerres, "Novel covalently cross-linked poly(etheretherketone) ionomer membranes," *Journal of Power Sources*, vol. 155, pp. 3–12, Apr. 2006.

[109] G. Ye, C. Mills, and G. Goward, "Influences of casting solvents on proton dynamics within sulfonated polyether ether ketones (S-PEEKs) studied using high-resolution solid-state NMR," *Journal of Membrane Science*, vol. 319, pp. 238–243, July 2008.

[110] R. Weast and J. Grasselli, eds., *CRC Handbook of Data on Organic Compounds, 2nd Edition*. Boca Raton, FL: CRC Press, 1989.

[111] K. Matsuoka, Y. Iriyama, T. Abe, M. Matsuoka, and Z. Ogumi, "Alkaline direct alcohol fuel cells using an anion exchange membrane," *Journal of Power Sources*, vol. 150, pp. 27–31, Oct. 2005.

[112] V. Bambagioni, C. Bianchini, A. Marchionni, J. Filippi, F. Vizza, J. Teddy, P. Serp, and M. Zhiani, "Pd and PtRu anode electrocatalysts supported on multi-walled carbon nanotubes and their use in passive and active direct alcohol fuel cells with an anion-exchange membrane (alcohol=methanol, ethanol, glycerol)," *Journal of Power Sources*, vol. 190, pp. 241–251, May 2009.

[113] B. Wieland, J. P. Lancaster, C. S. Hoaglund, P. Holota, and W. J. Tornquist, "Electrochemical and Infrared Spectroscopic Quantitative Determination of the Platinum-Catalyzed Ethylene Glycol Oxidation Mechanism at CO Adsorption Potentials," *Langmuir*, vol. 12, pp. 2594–2601, Jan. 1996.

[114] T. D. Jarvi, S. Sriramulu, and E. M. Stuve, “Potential Dependence of the Yield of Carbon Dioxide from Electrocatalytic Oxidation of Methanol on Platinum(100) ,” *The Journal of Physical Chemistry B*, vol. 101, pp. 3649–3652, May 1997.

[115] A. Kraytsberg, M. Auinat, and Y. Ein-Eli, “Reduced contact resistance of PEM fuel cell’s bipolar plates via surface texturing,” *Journal of Power Sources*, vol. 164, pp. 697–703, Feb. 2007.

[116] I. Nitta, O. Himanen, and M. Mikkola, “Contact resistance between gas diffusion layer and catalyst layer of PEM fuel cell,” *Electrochemistry Communications*, vol. 10, pp. 47–51, Jan. 2008.

[117] E. Herrero, J. M. Feliu, S. Blais, Z. Radovic-hrapovic, and G. Jerkiewicz, “Oxidative Desorption on the Pt (111) Electrode,” *Langmuir*, vol. 16, pp. 4779–4783, 2000.

[118] S. Sun, M. C. Halseid, M. Heinen, Z. Jusys, and R. Behm, “Ethanol electrooxidation on a carbon-supported Pt catalyst at elevated temperature and pressure: A high-temperature/high-pressure DEMS study,” *Journal of Power Sources*, vol. 190, pp. 2–13, May 2009.

[119] D. Gupta and V. Choudhary, “Sulfonated poly(ether ether ketone)/ethylene glycol/polyhedral oligosilsesquioxane hybrid membranes for fuel cell applications,” *International Journal of Hydrogen Energy*, vol. 37, pp. 5979–5991, Apr. 2012.

[120] Q. Xiang, Y. Y. Lee, R. W. Torget, and N. Renewable, “Kinetics of glucose decomposition during dilute-acid hydrolysis of lignocellulosic biomass.,” *Applied biochemistry and biotechnology*, vol. 113-116, pp. 1127–38, Jan. 2004.

[121] “U.s. department of energy: Energy efficiency & renewable energy: Biomass program.” `http://www1.eere.energy.gov/biomass/`.

[122] “Global bioenergy partnership.” `http://www.globalbioenergy.org/`.

[123] S. Thorsell, F. M. Epplin, R. L. Huhnke, and C. M. Taliaferro, "Economics of a coordinated biorefinery feedstock harvest system: lignocellulosic biomass harvest cost," *Biomass and Bioenergy*, vol. 27, pp. 327–337, 2004.

[124] G. M. Banowetz, A. Boateng, J. J. Steiner, S. M. Griffith, V. Sethi, and H. El-Nashaar, "Assessment of straw biomass feedstock resources in the pacific northwest," *Biomass & Bioenergy*, vol. 32, pp. 629–634, 2008.

[125] R. Perlack, L. Wright, A. Turhollow, R. Graham, B. Stokes, D. Erbach, and O. R. N. L. TN, "Biomass as feedstock for a bioenergy and bioproducts industry: the technical feasibility of a billion-ton annual supply," *Agriculture*, 2005.

[126] G. Gordon, N. Parker, P. Tittmann, Q. Hart, M. Lay, J. Cunningham, B. Jenkins, R. Nelson, K. Skog, M. P. Mallory, R. Rummer, R. J. Barbour, J. Stewart, E. Gray, A. Schmidt, C. Lindsey, G. Morris, A. Milbrandt, J. Kerstetter, and R. Overend, "Strategic assessment of bioenergy development in the west: Biomass resource assessment and supply analysis for the wga region," *Kansas State University and the U.S. Forest Service*, 2008.

[127] S. Kumarappan, S. Joshi, and H. L. MacLean, "Biomass supply for biofuel production: Estimates for the united states and canada," *Bioresources*, vol. 4, no. 3, pp. 1070–1087, 2009.

[128] M. E. D. De Oliveira, B. E. Vaughan, and E. J. Rykiel, "Ethanol as fuels: Energy, carbon dioxide balances, and ecological footprint," *Bioscience*, vol. 55, no. 7, pp. 593–602, 2005. 40 AMER INST BIOLOGICAL SCI WASHINGTON 942CH.

[129] J. Hill, E. Nelson, D. Tilman, S. Polasky, and D. Tiffany, "Environmental, economic, and energetic costs and benefits of biodiesel and ethanol biofuels," *Proceedings of the National Academy of Sciences of the United States of America*, vol. 103, no. 30, pp. 11206–11210, 2006.

[130] D. Agarwal, L. Kumar, and A. K. Agarwal, "Performance evaluation of a vegetable oil fuelled compression ignition engine," *Renewable Energy*, vol. 33, no. 6, pp. 1147–1156, 2008.

[131] J. E. Campbell, D. B. Lobell, and C. B. Field, "Greater transportation energy and ghg offsets from bioelectricity than ethanol," *Science*, vol. 324, no. 5930, pp. 1055–1057, 2009.

[132] T. U. of California Davis, "Strategic assessment of bioenergy development in the west: spatial analysis and supply curve development: final report," 2008.

[133] G. Perez-Verdin, D. L. Grebner, C. Sun, I. A. Munn, E. B. Schultz, and T. G. Matney, "Woody biomass availability for bioethanol conversion in mississippi," *Biomass & Bioenergy*, vol. 33, no. 3, pp. 492–503, 2009.

[134] B. L. Polagye, K. T. Hodgson, and P. C. Malte, "An economic analysis of bio-energy options using thinnings from overstocked forests," *Biomass & Bioenergy*, vol. 31, no. 2-3, pp. 105–125, 2007.

[135] "Treaty with the yakama, 1855." `http://www.ccrh.org/comm/river/treaties/yakima.htm`. United States, Dept. of State.

[136] K. Olney, Personal Communication, 2009.

[137] "Washington department of ecology. solid waste disposal data." `http://www.ecy.wa.gov/programs/swfa/solidwastedata/`, 2007.

[138] "2006 solid waste management plan update: Benton county solid waste department." `http://www.mrsc.org/GovDocs/B461SolidWstPlan.pdf`. SCS Engineers.

[139] "Office of financial management: State of washington: Poplution." `http://www.ofm.wa.gov/pop/`.

[140] "United states department of agriculture: National agricultural statistics service." `http://www.nass.usda.gov/`, 2009.

[141] R. G. Nelson, M. Walsh, J. J. Sheehan, and R. Graham, "Methodology for estimating removable quantities of agricultural residues for bioenergy and bioproduct use," *Applied Biochemistry and Biotechnology*, vol. 113-116, pp. 13–26, 2004.

[142] J. D. Kerstetter and J. K. Lyons, "Wheat straw for ethanol production in washington: A resource, technical, and economic assessment," *Washington State University*, 2001.

[143] S. Gupta, C. Onstad, and W. Larson, "Predicting the effects of tillage and crop residue management on soil erosion," *Journal of Soil and Water Conservation*, vol. 34, pp. 77–79, 1979.

[144] J. O. Howard, "Ratios for estimating logging residue in the pacific northwest," *U.S.D.A. Forest Service, Pacific Northwest Forest and Range Experiment Station*, 1981.

[145] "Washington depeartment of natural resources, washington state timber harvest." `http://www.dnr.wa.gov/BusinessPermits/Topics/Budget/Pages/washington_state_timber_harvest.aspx`, 2002.

[146] "Forest management play: Yakama reservation." United States Department of Interior: Bureau of Indian Affairs, 2005.

[147] J. A. Blackard, M. V. Finco, E. H. Helmer, G. R. Holden, M. L. Hoppus, D. M. Jacobs, A. J. Lister, G. G. Moisen, M. D. Nelson, R. Riemann, B. Ruefenacht, D. Salajanu, D. L. Weyermann, K. C. Winterberger, T. J. Brandeis, R. L. Czaplewski, R. E. McRoberts, P. L. Patterson, and R. P. Tymcio, "Mapping u.s. forest biomass using nationwide forest inventory data and moderate resolution information," *Remote Sensing of Environment*, vol. 112, no. 4, pp. 1658–1677, 2008.

[148] "Fuel treatment evaluator 3.0." `http://www.fpl.fs.fed.us/documnts/techline/fuel-treatment-evaluator.pdf`, 2006. USDA Forest Service Forest Product Laboratory.

[149] D. Gaveau and R. Hill, "Quantifying canopy height underestimation by laser pulse pentration in small-footprint airborne laser scanning data," *Canadian Journa of Remote Sensing*, vol. 29, no. 5, pp. 650–657, 2003.

[150] "The environmental costs and benefits of biomass energy use in california." `http://www.osti.gov/bridge/product.biblio.jsp?osti_id=481490`, 1997. NREL, editor. Berkeley, California: Futuer Resrouces Associates, Inc.

[151] B. Rummer, "Assessing the cost of fuel reduction treatments: A critical review," *Forest Policy and Economics*, vol. 10, no. 6, pp. 355–362, 2008.

[152] C. L. Mason, R. Gustafson, J. Calhoun, B. R. Lippke, and N. Raffaeli, "Wood to Energy in Washington : Imperatives , Opportunities , and Obstacles to Progress," Tech. Rep. May, University of Washington College of Forest Resources, Seattle, WA, 2009.

[153] "Forests and rangelands: Managing our natural heritage." `http://www.forestsandrangelands.gov/overview/index.shtml`, 2010.

[154] "A strategic assessment of forest biomass and fuel reduction treatments in western states." `http://www.fs.fed.us/rm/pubs/rmrs_gtr149.pdf`, March 2005. United States Department of Agriculture, Forest Service, Rockey Mountain Research Station.

[155] S. Rigdon, Personal Communication, 2009.

[156] K. Nordt, Personal Communication, 2009.

[157] R. D. Perlack and A. F. Turhollow, "Feedstock cost analysis of corn stover residues for further processing," *Energy*, vol. 28, pp. 1395–1403, 2002.

[158] "Kenworth truck company." `http://www.kenworth.com/1000_hom.asp`, 2010.

[159] H. Mahmudi and P. C. Flynn, "Rail vs truck transport of biomass," *Applied Biochemistry and Biotechnology*, vol. 129-132, pp. 129–132, 2006.

[160] L. O. Pordesimo, W. C. Edens, and S. Sokhansanj, "Distribution of aboveground biomass in corn stover," *Biomass and Bioenergy*, vol. 26, no. 4, pp. 337–343, 2004.

[161] D. Wang and X. S. Sun, "Low density particleboard from wheat straw and corn pith," *Industrial Crops and Products*, vol. 15, no. 1, pp. 43–50, 2002.

Appendix A

THE COMPLEX ECONOMICS OF BIOENERGY IN THE UNITED STATES: LESSONS FROM A YAKAMA NATION CASE STUDY

A.1 Abstract

The increasing demand for bioenergy in the United States necessitates detailed case studies of cost and supply to assess its feasibility. We have developed supply curves based on six feedstocks in five counties surrounding the Yakama Nation in central Washington using spatially explicit estimates of supply and transportation cost. The supply curves were used to examine a base case supply for a bioenergy plant, to analyze the effects of land ownership, and examine the impacts of uncertainty in parameters used to determine cost and supply. The results show that existing industries produce the cheapest supply of feedstock as a byproduct of their operations, while supplies harvested specifically for bioenergy are considerably more expensive. Fragmented land ownerships lead to the necessity of cooperation between owners and highlight the importance of a strong anchor supply close to the plant. Lastly, uncertainty in supply and cost parameters leads to larger ranges in available biomass, leading to reluctant investment in large plants.

Keywords: bioenergy, tribal, cogeneration, energy transportation, yakama, supply economics

A.2 Introduction

The United States is experiencing rapidly increasing demand for bioenergy from both the private and public sectors [121, 122]. Feedstocks as diverse as forest slash, corn stover, switchgrass, corn starch, sugarcane, and soybean oil are championed as solutions to the US problems of energy security, rural employment and development, and green house gas emissions [123,124]. The widely cited Billion Ton Study has estimated over 1 billion tons of sustainably harvested biomass available for bioenergy [125]. Like fossil fuel power plants, economics of scale are important for reducing capital costs per unit energy of bioenergy plants [124]. However, the size of a bioenergy facility is limited by the supply of biomass available at prices that can be competitive with the current market. Understanding the economics of bioenergy is therefore imperative to understanding its real world viability. Biomass markets tend to be regional since raw biomass is too low value and low energy density to transport long distances [126].

The US has many energy requirements that can be generally categorized into electricity, liquid transportation fuels, and heat [127]. Bioenergy has been shown to be capable of supplying any of these energy types. Liquid transportation fuels are currently produced by fermenting sugars and starches into ethanol and by transesterification of seed and waste oils into biodiesel [128–131], and in addition, there are several emerging technologies for converting biomass to liquid fuels (eg. lignocellulosic ethanol, algae biodiesel, etc). Heat can be produced by biomass combustion or gasification where it is typically coupled with a generator for the production of electricity. The researchers of this report have worked in close collaboration with the Confederated Tribes and Bands of the Yakama Nation in studying the biomass supply for a planned biomass combustion boiler on the Yakama Nation, and thus this report focuses on combustion for the combined generation of heat and power (CHP). However, supply economics factors are of principle importance for any type of bioenergy facility. One of the difficulties in accurately assessing the impacts of supply economics at a local scale is the high degree of spatial variability in feedstock price and density. Previous studies have solved this problem by developing spatial models to determine transportation and processing costs. However, these studies either looked at large spatial scales that leave out smaller roads and aggregate biomass supply at county centroids [132] or used spatially explicit estimates of biomass supply but fixed transportation costs [133]. Since transportation costs are often assumed to be the majority of the cost associated with obtaining biomass feedstock [133], there is a need to understand the fine scale interactions of transport and supply in a real world situation.

The myriad land ownerships, whether federal, state, tribal, or private found in the US also complicate the potential available supply. Each land owner tends toward different management objectives and may have budgetary restrictions or incentives that relate to bioenergy development and limit a resources availability. Ownership patterns also often resemble a checkerboard (eg, Fig A.1), yet spatial patterns of biomass seldom follow ownerships boundaries. In order to produce the most efficient use of the available resource, cooperation between owners is essential, yet the ramifications of ownership fragmentation on bioenergy economics is poorly understood.

Uncertainty in the parameters used to estimate bioenergy cost and supply is also an important, but often overlooked aspect of the economics of bioenergy. It is an oversimplification to use a single value to represent the costs. Processing steps such as truck loading and unloading or specific recoverable fractions of biomass vary by region, feedstock, season, topography, and other dynamic factors. Yet, due to information availability it is common to use a single value when assessing the economics of bioenergy [125, 132–134], with figures often cited and re-cited from previous sources. In this study, we have acknowledged the uncertainty in the cost and supply parameters and have attempted to show the effects of this uncertainty on the final supply curves.

A.3 Objective

We present a case study of a proposed direct combustion combined heat and electricity plant on the Yakama Nation in central Washington by assessing the supply and cost of feedstock in a five county area surrounding the proposed plant location. Our objective is to:

1. Develop a method that integrates spatially explicit transportation costs and supply into the production of supply curves for the proposed plant,

2. Analyze the effects of land ownership, and

3. Examine the impacts of uncertainty in cost and supply

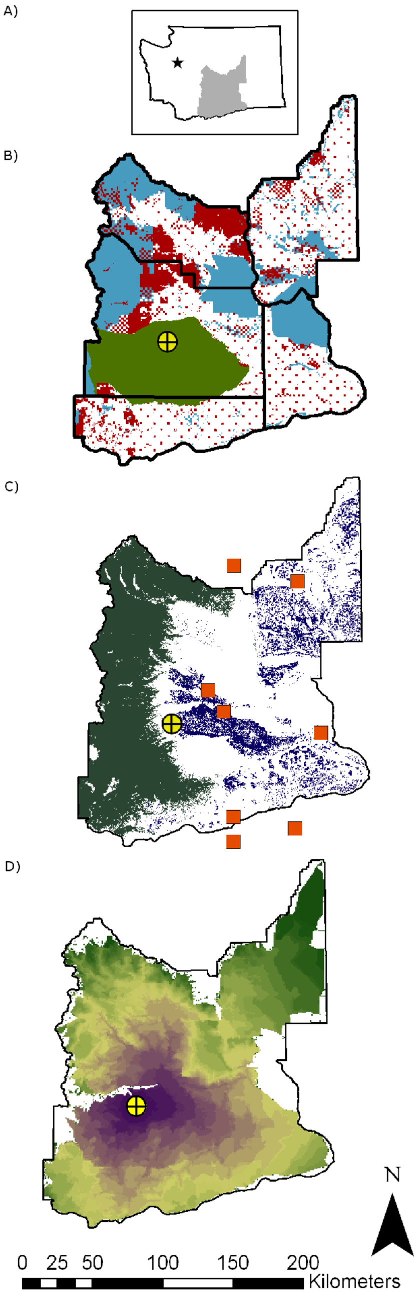

Figure A.1: (A) The 5 counties of the study region are illustrated on the map of Washington. Seattle is represented by the star. (B) Four land ownership groups within the study area: Yakama Nation (green), Federal land (blue), Washington State (red), and Private (white). (C) The spatial distribution of three biomass types: forest biomass (green), agricultural biomass (blue), and urban waste collection sites (orange boxes). (D) The effect of existing road network on round trip trucking costs, ranging from $19 (purple) to $343 (dark green). The yellow crosshairs represents the proposed cogeneration plant in (B), (C), and (D).

A.4 Methods

A.4.1 Study Area

Costs and supply were modeled for a five county extent in Washington, surrounding a proposed cogeneration power plant in White Swan, WA (Fig. A.1). The counties were selected because of their spatial proximity to the plant, their concentration of biomass resources, and their inclusion in legally recognized territory, ceded to the United States government by the Yakama Nation in 1855, on which the Yakama retain certain management rights [135].

A.4.2 Uncertainty

Developing a supply curve required selecting specific cost and supply parameters. In all cases, we attempted to use well cited values from the literature, but in no cases was there a value we considered to be unequivocal. Therefore, we assigned each parameter an uncertainty value from 1-4 based on our perception of the uncertainty in the assumption of that value for the parameter. These uncertainty values reflect our best judgment and those of an expert Yakama Nation forester [136]. The uncertainty value was used to populate a range in the parameter value according to Table 1.

A.4.3 Base Case Supply Estimates

Table 2 reports the supply parameters that were used to build the final supply quantities. Methodologies for selecting each parameter source are described below. Note that while the sawmill at the proposed site produces mill residues that could be used as a feedstock, we did not examine the effects these residues may have on the supply and economics.

Urban Waste

Urban biomass was limited to woody waste, appropriate for combustion. County totals of municipal waste were averaged from 2004-2007 [137] and reduced to 13% to account for the wood fraction [138]. The contributions of recycled and diverted waste to the urban waste stream was only available at the state level [137]. County totals were thus estimated using a ratio of county to state population [139]. Since some of the wood waste is already being used for hog fuel, animal bedding, and ground cover, we assumed that 45 percent of the waste would be available for this project from the counties of interest.

Agricultural Residues

There are several different sources of agricultural residues in the study area: annual crop residues (wheat straw, oat straw, barley straw, and corn stover), and perennial crop trimmings (orchard and vineyard). The annual crop yields were estimated using an average of USDA National Agricultural Statistical Services (NASS) information for 1990-2007 [140]. The estimated acreage for both annual and perennial crops was identified from the 2007 NASS totals. Straw and stover are not qualified as crops, and therefore are not tabulated in the NASS database. Thus, quantities of straw and stover are estimated from the grain yield of the specific crop. Wheat straw was estimated using a correlation by Nelson et al [141]. and was found to match well with methods used by Kerstetter and Lyons [142], and Banowetz et al. [123]. Oat straw, barley straw and corn stover were estimated using a table by Gupta et al. [143]. Soil requirements for erosion control and fertility require a minimum residue of straw and stover be left to decay in the field (Table 2). Orchard and vineyard trimmings are calculated based on 2007 NASS acreage and a correlation from a Western Governors Association report [126].

Logging Slash Piles

Commercial logging operations generate slash (unmerchantable tops, limbs, and damaged wood). The slash is typically piled and either left to decay or burned. We assumed that 1 m^3 of slash was produced for every 1 m^3 of cut wood, assuming a partial cut and the average value for public and private lands [144]. For each ownership group within the study area, except the Yakama Nation, separate logging estimates were used by averaging annual logging estimates reported to the Washington State DNR [145]. The logging on Yakama Nation lands was estimated by choosing a representative annual cut specified in their forest management plan [146]. Totals are summarized in Table 3.

The spatial location of the slash pile supply was estimated by creating a continuous raster surface. Slash pile supply was adjusted by the relative density from aboveground biomass estimates produced by Blackard et al. [147] so that the total slash pile supply equaled the amounts in Table 3 for each ownership group, but was spatially arranged by the patterns produced by the remotely sensed aboveground biomass.

Fuel Reduction Thinning

Thinning of small-diameter wood has been proposed as a source of bioenergy but has not been enacted over large spatial extents. In order to estimate the supply and spatial location of the resource, the Fuel Treatment Evaluator [148] was used to identify the average mass of biomass that could be removed from each ownership group to reduce wildfire risk. To adjust for the distribution of biomass, an aboveground biomass map [147] was used to adjust each pixel while allowing the mean to equal the output from the Fuel Treatment Evaluator. We assumed that no new roads would be created to access thinning resources, and utilized the existing forest roads with a maximum skid distance of 122 m (400 ft), creating a subset of the total available supply. This distance was based on economic viability and local forestry practices.

A.4.4 Base Case Cost Estimates

We quantified the available biomass supply as a function of delivered cost to the biomass conversion facility. This delivered cost was determined by a combination of biomass collection cost, processing cost, loading cost, transportation cost, and unloading cost. Arriving at single, robust cost parameters is a difficult task owing to the many factors that we did not model (eg. fluctuations in fuel prices, capital costs, economies of scale, etc.). Therefore, a range of parameter values was included (Table 4) and modified using the uncertainty adjustment from Table 1. Reducing the uncertainties for these costs will require pilot scale field studies.

Transportation

The transportation cost of the biomass was estimated by developing a model based partly on the methodology described in a Western Governors Association report [126]. The model estimates both time-based and distance-based transportation costs. Model inputs are based on physical features of roads within the study area. Roads were imported into ArcGIS 9.3 (ESRI corp.) and assigned a road class based on the average speed a semi-trailer truck would be able to maintain on each road segment. Road class 1 assumed an average speed of 50 mph and was confined to divided highways. Road class 2 assumed an average speed of 40 mph and was confined to improved paved secondary roads. Road class 3 assumed an average speed of 30 mph and was confined to improved unpaved secondary roads. Road class 4 assumed an average speed of 20 mph and was confined to forest roads. Roads speeds were assigned based on existing speed limits and conversations with an expert forester. Topography, which can influence truck speed, was not modeled. Class 1 and 2 roads were imported from publicly available GIS shapefiles, and Class 3 and 4 were assigned after importing a publicly available GIS shapefile with no road classification information and assigning classification visually by comparing to 2006 NAIP imagery. Road width was the principle visual identifier used to differentiate between class 3 and 4. The final roads layer was analyzed using the Network Analysis extension in ArcGIS 9.3. A service area was calculated around the proposed plant location and distance and time polygons were generated based on road length and traversal time. These polygons were converted to rasters, and doubled to provide roundtrip measures. Raster values of time and distance were multiplied by cost parameters, and summed to produce the final transportation model.

Truck capacity can significantly influence transportation cost. Large chip vans can be utilized on improved roads, but limits in turning restrict forest roads to smaller capacity trucks. Therefore, transportation over class 3 and 4 roads was limited to trucks of a smaller capacity (Table 4). We assumed a single trip utilizing one trip from the forest to the plant, though transfer to larger trucks at the edge of the forest is also an option [134].

Urban Waste

To include the urban waste in our supply curves transportation and acquisition costs were needed. The facility urban waste numbers from 2007 were used [137]. The location of these sites was used to estimate the transportation cost as noted above. Three urban waste sources were outside of the study area, but were very close, a significant source, and received waste originating from within the study area. The distance and number of minutes to the nearest modeled transport raster cell were calculated and used to determine the transportation costs separately for those three sources. The current cost of urban wood in Yakima County is \$11 per wet ton[i] (\$22 per BDT) [149]. This cost is expected to increase, and so it was only used as a starting point for cost estimates.

Agricultural Residue

The typical disposal procedure for tree trimmings in the study area is either mulching in place or piling and burning at the field edge [150]. Farmers already pay for the disposal of fruit tree trimmings so they were assumed to be available at no additional cost. In California where a fruit tree trimmings market is developed, trimmings were available delivered in 1993 for \$37-55 BDT [150]. It is not clear what price would make trimmings economical for use as an energy source within the study area. Once piled, the woody material is assumed to be chipped, loaded, trucked to the plant, and unloaded using assumptions found in Table 4. Unlike fruit tree and vineyard trimmings, straw and stover biomass is not typically collected by farmers so their collection cost is significant. The cost estimates for collecting and stacking the straw and stover biomass at the edge of the field is a function of the crop yield. The costs were estimated based on the average county yield from USDA crop yields [140] and a price correlation from Gordon et al. [126]. These collection costs ranged from \$32/BDT to \$240/BDT.

---

[i] All mass values used in this study are reported in metric tonnes (T), or bone dry metric tonnes (BDT)

Logging Slash Piles and Fuel Reduction Thinning

Slash piles are typically burned or left in place, and are thus assumed to be available at no cost. There is a large range of reported values for the cost of performing fuel reduction thinning [151], with no logical best number. Therefore, we used a median values as a base case and will show the effects of the range in cost estimates. Like fruit tree trimmings, once piled, the woody material is assumed to be chipped, loaded, trucked to the plant, and unloaded (Table 4).

A.5 Results and Discussion

A.5.1 Transportation Cost Modeling

Figure A.1C shows the distribution of round trip transportation costs for accessible areas within the study area. Conspicuous patterns are produced by high speed highways running to the northwest, east, and south of the proposed plants. High densities of forest roads to the west allow for inexpensive roundtrip transport to resources on the Yakama Nation, but topography and wilderness limit access to the immediate north and far west.

Existing roads on the Yakama Nation provide for ample ability to access a large amount of biomass at low cost, with most areas costing less than $10 dollars per BDT to access for a truck with a 20 MT capacity. Resources outside of the Yakama Nation become more expensive, but because most of the biomass available is tied to existing agriculture and industry, quality road networks are in place and help to increase the efficiency of access.

It is only in areas with little active forest products activity, such as the northwestern part of the study area, where road quality begins to significantly increase the rate at which cost increases with distance from the plant. Contrary to a common assumption, over-the-road transportation costs do not dominate the cost of these biomass resources. Rather, it is the collection, processing, loading, and unloading that are the dominant force in this case study. This is due in part to the wealth of resources in close proximity to the proposed plant, but it also shows how trucks with large capacities can reduce over the road cost of delivered BDT.

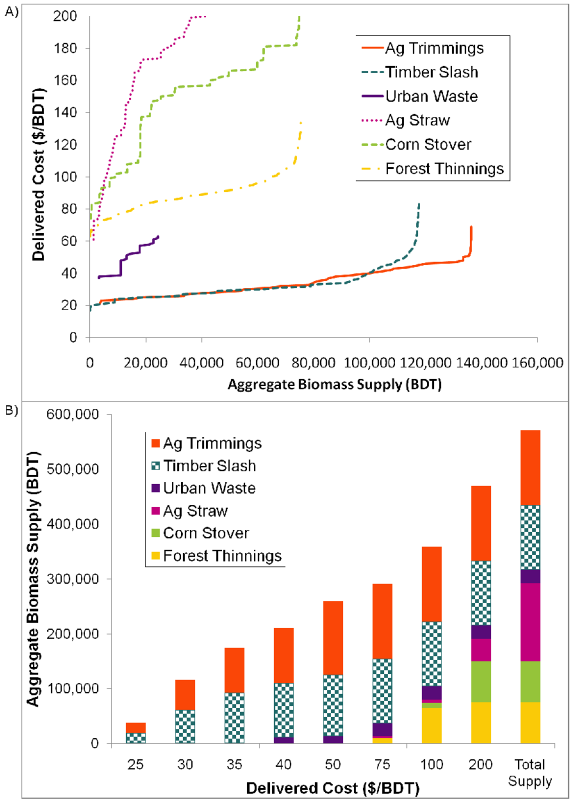

Figure A.2: Base case aggregate supply and cost estimates for six feedstocks within the study region. (A) Shows the projected annual delivered cost and aggregate supply of each feedstock and (B) shows the aggregate supply corresponding to each feedstock at eight delivered costs and the maximum supply of the study region.

A.5.2 Base Case Supply Curves

The results of the supply economics modeling of the biomass for the Yakama cogeneration facility are shown in Figure A.2. Overall the region has an estimated 470,000 BDT of biomass available for bioenergy. The two most inexpensive sources were also the largest: orchard and vineyard trimmings from tribal and private farmers and slash from normal timber operation are available at around $20 per BDT and plateau at around $70 per BDT. These less inexpensive biomass resources benefit from established industries that are producing other high value products. Without an operational timber mill as a destination for sawlogs or an established fruit packing and processing industry, there would be little creation of slash or fruit tree trimmings resulting in significantly increased cost and reduced supply of biomass. Urban waste produces a medium-priced but relatively small supply of biomass. Unlike large regional metropolises such as Seattle, WA and Portland, OR, population density is relatively low in the study area, thus limiting supply.

Fuel reduction thinning provides a large potential supply, but the high costs of removing small diameter trees from the forest causes this resource to be one of the more expensive, and may therefore limit its contribution to bioenergy. This finding is important because bioenergy has often been touted as a method for funding fuel reductions thinning operations [134, 152]. At over $75/ BDT, this resource would likely be too expensive, and would require subsidy to be economically viable as a feedstock. Through programs such as the Healthy Forest Initiative [153], and Forest Service stewardship contracting, the federal government may provide such a subsidy. Subsidies would need to be stable over the course of the life of the plant to maintain supply, otherwise investors will be reluctant to invest the capital needed to build a facility that relies on biomass from fuel reductions.

The most expensive biomass sources are the oat and wheat straw, and corn stover. The agricultural residues have a significant cost of collection on the field, are relatively low bulk density for transportation, and their fertilizer value must be replaced which significantly increases their cost. The available biomass at different costs can be seen in Figure A.2B. As an example of the real world relevance of these findings, for the cogeneration plant considered in this study to be viable, delivered costs needed to be $40 per BDT or less. At that level there is an estimated 214,000 BDT. A 15 MW combustion facility with an estimated efficiency of 20% needs an estimated 120,000 BDT per year. The base-case estimate shows adequate biomass at the $40 level for this type of facility. The majority of that biomass is from waste produced by industry, though, and shows that a bioenergy plant would be reliant on the survival of the timber and fruit tree industries well into the future.

A.5.3 Economic Ramifications of Ownership Boundaries

There are a variety of different land owners in the study area: USDA Forest Service, Washington State Department of Natural Resources, Yakama tribal trust, and private farms (private forest lands were excluded from the study because they represented a small proportion of the landscape). A map of land holdings can be seen in Figure A.1A. Ownership of the biomass resources has implications in setting up a biomass contract. Multiple land owners make negotiations more difficult. The existence of an anchor supply significantly enhances the viability of the bioenergy facility.

A breakdown of the biomass supply and cost can be seen in Figure A.3. At the $40 level the major contributors are tribal and private land owners. While the available biomass on tribal lands benefits the proposed cogeneration plant, if this plant is not built, any future projects should include tribal partnership. Many other tribes have large forested landholdings in the West (eg. Colville Confederated Tribes, the Confederated Salish-Kootenai tribes, Quinault Indian Nation, the Confederated Tribes of Warm Springs Reservation, etc), underscoring the importance of tribal collaboration in bioenergy projects. In many cases, tribal lands may be the logical sites for bioenergy plants because of their proximity to resources and the unique economic environment in which tribes operate; for example, the Yakama Nation retains the last major saw mill operation in all of Washington east of the cascades. For the private land owners which could supply the fruit tree and vineyard trimmings, contracts through food co-ops would be necessary to guarantee that the resources are available. The guarantee is necessary for the bioenergy facility to secure loans and investment. Many distributed land holdings make contracting difficult and expensive.

Forest biomass from state and federal landholdings is too expensive to contribute much

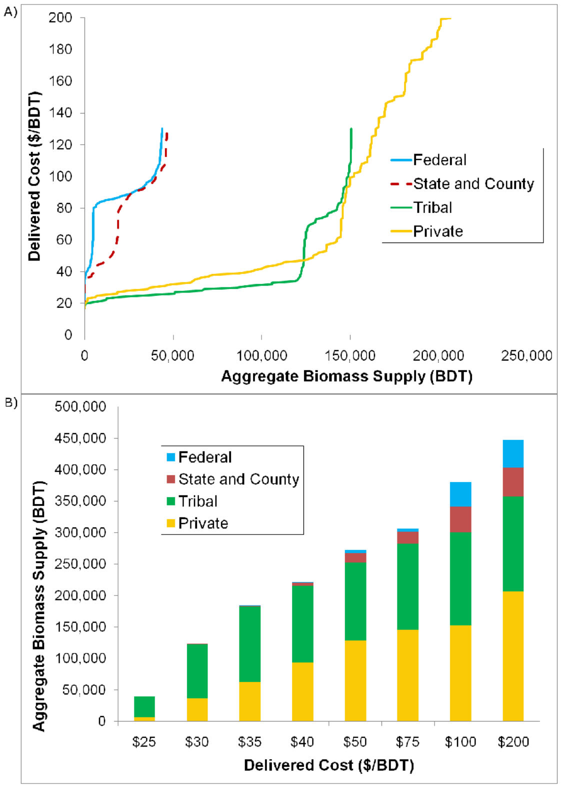

Figure A.3: (A) Base case aggregate supply curves for the four ownership classifications. (B) The aggregate supply at eight different costs for four land ownerships.

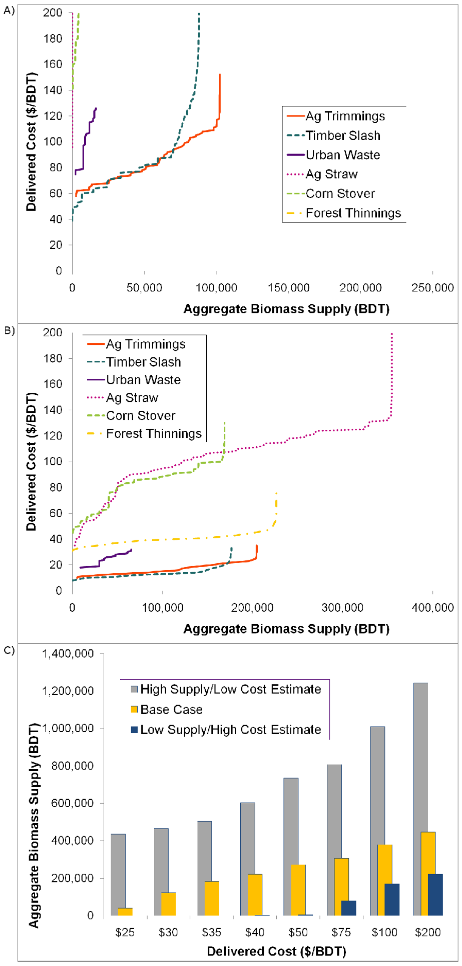

Figure A.4: (A) Aggregate supply curves for six feedstocks under assumptions of lowest supply and highest cost. (B) Aggregate supply curves for six feedstocks under assumptions of highest supply and lowest cost. (C) The aggregate supply of the combined feedstocks at three levels of uncertainty for eight delivered costs.

to the biomass supply. Both owners produce a small fraction of logging slash compared to the Yakama Nation, and most of the supply comes from expensive fuel reduction thinning. Stewardship contracts are likely the only method of reducing the cost of biomass from these ownerships to levels appropriate for a cogeneration plant.

A.5.4 Economic Ramifications of Uncertainty in Cost and Supply Parameters

Since no parameter used in developing the supply curves was known with 100% certainty, the results showing a wide range between conservative and liberal parameters is not unexpected (Fig A.4). For instance, assumptions about truck capacity strongly influence the delivered cost of the slash and thinning supply. Larger trucks lead to net reductions in transportation costs, but there is great uncertainty in the types of trucks that can navigate forest roads. Logging trucks are specially designed to navigate the tight turns of forest roads, but existing chip vans are typically only used on paved roads. Thus, the optimum truck for accessing forest biomass resources may not yet exist. It is likely that better trucks will be developed if a robust bioenergy market develops, but without such markets, it is difficult to predict with certainty the attributes of trucks used in the assessment in the current study. Another example of uncertainty is the range in the cost to produce piles of thinned trees at a forest landing, which, varied from $25 to $250. This variation reflects the uncertainty and variation found in reported values in the literature [134, 151, 154] as well as variation in anecdotal costs estimates from those familiar with forests in the study area [155], and is one of the major drivers of the differences in cost estimates for biomass from forest thinning.

Differences in supply relate to uncertainty in the amount of existing biomass that can realistically be extracted and transported to a plant. For straw and stover, much of this uncertainty centers around concerns of how much residue should be left on the field to maintain soil tilth. Thinning supply drastically changes based on the assumption of the amount of time required to treat the entire forest whilst ensuring sustainable future supply through regeneration and regrowth. This is a very difficult parameter to estimate because of variation in tree density between forest stands within the study area, risk of loss of resource from large wildfires, ecological concerns over whether management is appropriate, and differences in management methods (eg prescribed fire vs. thinning). For all resources, variation in recoverable fraction affects the amount of biomass that is present but unsuitable for bioenergy (eg: needles in slash piles) or may be lost during transport.

The coupled uncertainty in supply and cost can lead to major issues in deciding whether to move forward on a large capital project such as a cogeneration plant. A reliable supply of biomass needs to be available at a reliable price for the life of the plant. Figure A.4 shows the variation in supply available with the different assumptions at different price points. The significant variation in estimated biomass available has significant implications for a bioenergy facility. These uncertainties have created local conditions that expect a supply approximately five times larger than the demand of a proposed plant in order to attract capital investment [156].

A.5.5 Avoided Costs

A significant factor in the economics of the proposed plant not captured in the supply curves are the avoided costs. For instance, the current practice of Yakama National Tribal Forestry is to burn slash piles in place. This incurs a labor cost, as fuel treatment personnel need to monitor the fire, as well as a cost to the regions air quality. Similarly, the costs of not performing fuel treatments are large fires that require extremely expensive fire fighting and significant inputs of smoke that reduce air quality. The uncertainty in how to quantify these avoided costs makes it difficult to compare to actual costs observed in the supply curves, but the existence of these costs is non debatable. Capturing the value of avoided costs is one method of improving the economics of bioenergy.

A.6 Conclusions

We have developed supply curves derived from spatially explicit estimates of cost and supply for six biomass feedstocks currently available in a five county area surrounding a proposed cogeneration plant in White Swan, WA. The results show that waste materials produced from existing industries (logging and fruit production) are the most economically viable feedstocks. The continued availability of these feedstocks is dependent on the continued health of the two industries. More generally, we show that ownership boundaries can restrict the available biomass supply and suggest that careful siting and inclusion of all land owners is necessary for the most efficient use of resources. Bioenergy projects may benefit from the inclusion of a strong anchor supplier, such as exemplified by the Yakama Nation. The uncertainty inherent in the multiple assumptions imbedded in producing the supply curve leads to a large range in cost and supply. This uncertainty drives the need for excess supply in order to secure investment. On the basis of financing safety margins alone, the technically available supply cited in the Perlack et al.s Billion Ton Study would be roughly cut by 20%. Finally, capturing the value of avoided costs may help to improve the economics of bioenergy.

Future research is necessary to refine and reduce the uncertainty in the assumptions. Small, site specific pilot projects may be useful for refining parameters that are not constant at national scales due to differences in local economics, laws, and geography. The effect of feedstock specific subsidies and the effect of subsidies on reducing the price of competing energy resources also warrants further study. Careful consideration of the history and life cycle impacts of subsidization is necessary though, to minimize the chance of creating markets that may compete with food or damage ecosystems. Finally, a carbon economy may create opportunities to offset the cost of certain feedstocks. Research into the economics of the carbon economy in relation to bioenergy, as well as new technologies that may increase efficiencies or produce valuable new product is essential if cost of bioenergy in the United States is to become competitive with other energy sources.

Appendix

Table A.1: Methodology for Producing Uncertainty Ranges in Cost and Supply Parameters

Uncertainty Rank	High Deviation from Base Case	Low Deviation from Base Case
1	0	0
2	0.75	1.5
3	0.5	2
4	0.5	5

Table A.2: Parameters used in determining biomass supply

Supply Parameter	Base Case	Low Estimate	High Estimate	Source	Uncertainty
Agricultural Recovery	60%	30%	90%	[125]	2
Slash Recovery	60%	30%	90%	[125]	2
Thinning Recovery	60%	30%	90%	[125]	2
Urban Waste Recovery	45%	34%	68%	[125]	3
Thinning Rotation	30 years	15 years	150 years	[125]	4
Straw Recovery	40%	30%	60%	[157]	2
Stover Recovery	50%	37.5%	75%	[157]	2
Sustainable Limit	4000 lbs/acre	3000	6000	[124]	2

Table A.3: Annual Logging Estimates (m^3)

Yakama Nation	Yakima FS	Yakima DNR	Kittitas FS	Kittias DNR	Klickitat DNR
35,400	13,211	9,341	22,045	10,533	30,703

Table A.4: Parameters used in Determining Biomass Cost

Supply Parameter	Base Case	Low Estimate	High Estimate	Source	Uncertainty
Small Chip Truck Cap.[ii]	18.1 T	9.0 T	36.2 T	[158]	3
Large Chip Truck Cap.[iii]	30.9 T	23.2 T	46.5 T	[134]	2
Stover and Straw Truck Cap.	17 T	12.8 T	25.5 T	[159]	2
Stover and Straw Moisture	50%	25%	75%	[160,161]	2
Chipped Wood Moisture	50%	25%	75%	[iv]	2
Urban Waste Moisture	20%	10%	40%	[iv]	3
Transport Cost (Time)	$29/hour	$22/hour	$43.5/hour	[132]	2
Transport Cost (Distance)	$0.75/km	$0.56/km	$1.13/km	[132]	2
Thinning Cost	$50/BDT	$25/BDT	$250/BDT	[134,151,154]	4
Loading Cost	$5.50/BDT	$2.80/BDT	$11/BDT	[132]	3
Chipping Cost	$4.40/BDT	$2.20/BDT	$8.80/BDT	[154]	3
Unloading Cost	$5.50/BDT	$2.80/BDT	$11/BDT	[132]	3
Urban Waste Collection Cost	$22/BDT	$10/BDT	$40/BDT	[137]	3
Fruit Tree Farmer Profit	$5/BDT	$2.5/BDT	$25/BDT	[iv]	4
Straw Profit and Nutrients	$10/BDT	$5/BDT	$50/BDT	[125]	3
Edge of Field Collection Cost	Variable	75%	150%	[iv], [126]	2

[ii] Small chip truck was used for slash and thinning calculations

[iii] Large chip truck was used for fruit tree trimming and urban waste routes

[iv] Values chosen based on common sense and input from an expert forester [136]